Supplementary Information to Agreement, opposition, and dataset influence in global evapotranspiration trends

Johanna Ruth Thomson[1], Yannis Markonis[1], Riya Dutta[2], Simone Fatichi[3], Martin Hanel[1], Akash Koppa[4], Petr Maca[1], Vishal Thakur[1], Mijael Rodrigo Vargas Godoy[5], and Athanasios Paschalis[6]

[1]Faculty of Environmental Sciences, Czech University of Life Sciences Prague, Kamýcká 129, Praha – Suchdol, Czech Republic

[2]Department of Environmental Science and Engineering, Indian Institute of Technology Dhanbad, Dhanbad, India

[3]Department of Civil and Environmental Engineering, National University of Singapore, Singapore, Singapore

[4]Department of Environmental Science and Technology, University of Maryland, College Park, MD, USA

[5]Department of Physical Geography and Geoecology, Charles University, Prague, Czechia

[6]Department of Civil and Environmental Engineering, University of Cyprus, Nicosia, Cyprus

Correspondence: Johanna R. Thomson bloecher@fzp.czu.cz

1 Text S1. Data sets

1.1 Reanalysis products

1.1.1 ERA5-Land

- **General information:** ERA5-Land (Muñoz-Sabater et al., 2021) is a reanalysis product providing monthly ET data at $0.1^\circ \times 0.1^\circ$ spatial resolution spanning 1950 to present. The European Centre for Medium-Range Weather Forecasts (ECMWF) provides the ERA5-Land monthly averaged data. ERA5-Land is a land-surface reanalysis produced by running the Carbon Hydrology-Tiled ECMWF Scheme for Surface Exchanges over Land (CHTESSEL; model cycle Cy45r1) land surface model offline. More information on the CHTESSEL model implementation can be found on https://www.ecmwf.int/en/elibrary/80895-ifs-documentation-cy45r1-part-iv-physical-processes, last checked on 06.02.2026.
- **ET scheme:** The land surface in CHTESSEL is represented using a tiled approach analogous to the mosaic method of Koster and Suarez (1992). Each land grid box is divided into up to eight surface tiles: water, ice, low vegetation,

Table S1. Summary of evapotranspiration (ET) approach and resistance formulations. Abbreviations: r_a = aerodynamic resistance; r_v = vegetation resistance; r_s = soil surface resistance; BL = boundary layer; LAI = leaf area index; SW = shortwave radiation; PAR = photosynthetically active radiation; VPD = vapour pressure deficit; RH = relative humidity; SM = soil moisture; RZSM = root-zone soil moisture; VOD = vegetation optical depth; A_n = net CO_2 assimilation; ML = machine learning; int. = interception; n/s = not specified in product paper.

Dataset	Evaporation approach	Resistances
BESS v2	Quadratic Penman–Monteith embedded in a carbon-energy balance linking ET to photosynthesis with instantaneous estimates upscaled to daily totals.	r_a: iterative, Two-leaf (sun/shade): input n/s; r_v: Ball–Berry (A_n, CO_2, RH, VPD); r_s: n/s
ETMonitor	Multisource remote-sensing energy and water balance model using Shuttleworth–Wallace two-source scheme for transpiration and soil evaporation and Penman combination equation for open water and sublimation.	r_a: two-source (canopy + soil), input: wind, roughness(canopy height), LAI ; r_v: Jarvis (SW, VPD, T, RZSM); r_s: SM
GLEAM v4.1a	Potential evaporation from Penman equation combined with neural net trained stress functions to derive actual ET.	r_a: multi-source (soil + low + high veg), Thom's equation, input: roughness (canopy height), LAI; r_v: ML stress (SM, VOD, VPD, T, LAI, CO_2); r_s: n/s
ERA5-Land	Surface energy balance solved in CHTESSEL. Evaporation calculated from vapour gradient between surface and lowest atmospheric level.	r_a: multi-source (soil + low + high veg): wind, roughness (tabled, vegetation type); r_v: Jarvis (LAI, SW, VPD, RZSM); r_s: SM, wilting point, field capacity.
MERRA-2	Surface energy balance with GEOS-5 and CLSM. ET includes bare soil evaporation, transpiration, canopy evaporation and snow evaporation.	r_a: n/s; r_v: n/s; r_s: n/s
JRA-55	Japanese Simple Biosphere (SiB) model where ET is calculated from vapour pressure difference modulated by resistance terms.	r_a: two-source (canopy + soil). Input: wind, canopy height; r_v: Jarvis (LAI, PAR, T, RH); r_s: SM
FLDAS	Surface energy balance solved in Noah model 3.6.1.	r_a: n/s; r_v: Jarvis (SW, VPD, T, SM); r_s: SM
GLDAS-CLSM v2.1	Surface energy balance solved in CLSM 2.5	r_a: n/s; r_v: n/s; r_s: n/s
GLDAS-NOAH v2.1	Surface energy balance solved in NOAH 3.6	r_a: n/s; r_v: Jarvis (SW, VPD, T, SM); r_s: SM
GLDAS-VIC v2.1	Reference ET is calculated with Penman-Monteith, actual ET is scaled and surface fluxes rebalanced in VIC 4.1.2	r_a: n/s; r_v: n/s; r_s: SM
TerraClimate	Modified Thornthwaite–Mather climatic water balance model using FAO Penman–Monteith reference ET constrained by soil water availability	r_a: n/s; r_v: n/s; r_s: n/s
MOD16A3GF	Penman–Monteith algorithm with day/night and wet/dry canopy and soil partitioning.	r_a: single-source (leaf-upscaled), input: LAI, temperature; r_v: stomatal+cuticular: LAI, VPD; r_s: n/s
CAMELE	Composite evapotranspiration product using collocation analysis merging ERA5-Land, FLUXCOm, PMV2, GLDAS-Noah v2 and v 2.1, GLDAS-CLSM v2 and v 2.1, GLDAS-VIC v2 and v 2.1 and GLEAM 3.7a.	
SynthesizedET	Composite ET dataset merging PML, SSEBop, MOD16A2105 and NTSG using temporal averaging and spatial resampling.	

Table S2. Main evapotranspiration input variables grouped by forcing/input, prognostic-diagnostic and not included. Abbreviations: LAI = leaf area index; P = precipitation; Rad = radiation; SM = soil moisture; U = wind speed; T_a = air temperature; VPD = vapor pressure deficit; T_s = soil temperature; RH = Relative humidity; NSW = net short-wave radiation; NLW = Net long wave radiation; DSW = Downward short wave radiation.

Dataset	**Forcing/Input data**	**Prognostic/Diagnostic**	**Not included**
BESS v2	LAI: MODIS, GLOBMAP Rad: ERA5 U: WorldClim T_a: ERA5 VPD/RH: MODIS		P, T_s, SM: –
ETMonitor	LAI: GLASS P: GPM Rad, U, T_a: ERA5 VPD/RH: MODIS SM (surface): ESA CCI	SM	T_s: –
GLEAM v4.1a	LAI: MODIS (MOD15A3H) P: MSWEP v2.8 Rad: MSWX U: ERA5 T_a, VPD/RH: MSWX SM (surface): ESA CCI	SM	T_s: –
ERA5-Land	LAI: MODIS P, Rad, U, T_a, VPD/RH: ERA5	T_s, SM	
MERRA-2	LAI: AVHRR P: prog, CMAP/GPCP	Rad, U, T_a, VPD/RH, T_s, SM	
JRA-55	P, Rad: GSM	U, T_a, VPD/RH, T_s, SM	LAI: not specified
FLDAS	LAI: AVHRR, MODIS P: CHIRPS Rad, U, T_a, VPD/RH: GDAS, MERRA-2	T_s, SM	
GLDAS v2.1	LAI: AVHRR, MODIS P: GPCP Rad: AFWA AGRMET U, T_a, VPD/RH: GDAS	T_s, SM, NSW, NLW, T_a, U, P, DSW	
TerraClimate	P, T_a, VPD/RH: WorldClim v2, CRU-TS4, JRA-55 Rad, U: WorldClim v2, JRA-55	SM	LAI, T_s: –
MOD16A3GF	LAI: MODIS Rad, U, T_a, VPD/RH: GMAO reanalysis	P, T_s, SM: –	

high vegetation, bare soil, exposed snow, snow under high vegetation, and intercepted water. All tiles share a single atmospheric column above and a single soil column below, but each has its own surface energy balance solved for the tile skin temperature, as well as tile-specific properties including emissivity, albedo, and skin-layer conductivity. Total evaporation is the area-weighted sum of evaporative fluxes from all tiles and comprises transpiration from vegetation, bare soil evaporation, evaporation from the interception reservoir, open water evaporation, and sublimation from snow. Here we use the total evaporation field. For each tile, evaporation is computed as the turbulent moisture flux between the surface and the lowest atmospheric model level ($\sim$10 m above the surface), depending on air density, wind speed, and the difference in specific humidity between the saturated surface (evaluated at the tile skin temperature) and the overlying atmosphere, modulated by tile-dependent resistances.

– **Resistances:** The evaporation flux is regulated by a series of resistances whose formulation varies by tile type. The aerodynamic resistance, common to all tiles, is derived from the turbulent transfer coefficient following Monin–Obukhov similarity theory and depends on wind speed, atmospheric stability, and the roughness lengths for momentum and heat. For vegetated tiles, an additional canopy resistance follows the Jarvis-type formulation (Jarvis, 1976), defined as the minimum stomatal resistance scaled by the leaf area index (LAI) and modulated by stress functions for incoming shortwave radiation, root-zone soil moisture availability (scaled between the permanent wilting point and field capacity, weighted by the root distribution across the soil layers), and atmospheric vapour pressure deficit. Bare soil evaporation is governed by a soil surface resistance with a minimum value of 50 s m^{-1}, depending on the moisture content of the uppermost soil layer; the associated stress function is scaled between the field capacity and a vegetation-weighted minimum moisture content that accounts for the texture-dependent residual moisture in unvegetated fractions and the permanent wilting point in vegetated fractions. The roughness lengths for the bare soil tile correspond to the "desert" vegetation type. For the tile representing high vegetation with snow underneath, an additional sub-canopy aerodynamic resistance (67 s m^{-1} under unstable conditions, 220 s m^{-1} under stable conditions) governs snow sublimation. Finally, an interception resistance acts as a flux limiter when the water stored in the interception reservoir is insufficient to sustain potential evaporation over the model time step, based on the potential evaporation from the previous time step.

– **Soil scheme:** The subsurface is discretised into four soil layers with fixed depths of 0.07, 0.21, 0.72, and 1.89 m, shared by both the thermal and hydrological budgets. Six soil texture classes ranging from coarse to very fine, plus an organic class, are defined, with the dominant texture assigned per grid cell. Soil hydraulic properties are parameterised using the van Genuchten formulation, with the permanent wilting point and field capacity corresponding to matric potentials of -15 bar and -0.1 bar, respectively. Soil water movement follows Richards' equation with Darcy's law; the upper boundary condition is defined by infiltration (throughfall minus surface runoff) and surface evaporation, and the lower boundary assumes free drainage with no bedrock representation. Surface runoff is generated via a variable infiltration scheme sensitive to sub-grid orographic variability and soil texture. The soil heat budget obeys Fourier's diffusion law, driven at the top by the net ground heat flux from the tiled surface energy balance and bounded at the bottom by a zero-flux (insulating) condition. Soil water phase changes and their associated latent heat effects are accounted for,

including the suppression of water transport in frozen soils, although the effect of ice on soil thermal conductivity is not represented. When snow is present, an additional prognostic snow layer overlies the soil with its own temperature and mass balance, contributing to surface runoff via melt, soil infiltration, and sublimation.

- **Interception:** The interception reservoir is represented as a single-layer store with a grid-box maximum capacity of 1 mm, computed from a base value of 0.2 mm per unit leaf area (or bare ground) scaled by the LAI-weighted contributions from high vegetation, low vegetation, and bare soil fractions. It collects liquid water from rainfall interception and dewfall, and loses water through evaporation at the potential rate when sufficient water is available. Its water content is a prognostic variable. The formulation is water-conserving and based on Rutter.

- **Data and important information:** CHTESSEL in ERA5-Land is forced by near-surface atmospheric fields from the ERA5 reanalysis, including 2-m air temperature, 2-m specific humidity, 10-m wind speed, surface pressure, downward shortwave and longwave radiation, and liquid and solid precipitation. These fields are interpolated from the $\sim$31 km resolution of ERA5 to the $\sim$9 km native resolution of ERA5-Land using linear interpolation on a triangular mesh; the atmospheric forcing provides an indirect observational constraint on the land surface model estimates. Static ancillary fields include orography (SRTM30), land cover (GLCCv1.2), LAI and albedo (MODIS-derived, prescribed as monthly climatologies), soil type (FAO Digital Soil Map of the World), and lake depth (GLDB). Vegetation is classified using the Biosphere-Atmosphere Transfer Scheme (BATS) with 20 vegetation types, each designated as low or high vegetation and characterised by fixed parameters including minimum stomatal resistance, vegetation fractional cover, root distribution coefficients, skin-layer conductivity (with separate values for stable and unstable conditions), the fraction of shortwave radiation transmitted to the soil, and separate roughness lengths for momentum and heat. In summary, ET in ERA5-Land is governed by the meteorological forcing from ERA5 (air temperature, wind speed, radiation, humidity, and precipitation), prognostic land surface state variables (skin temperature, soil moisture, interception water content, and snow mass), and prescribed surface properties (roughness lengths, soil hydraulic parameters, root-zone characteristics, and vegetation parameters such as LAI and stomatal resistance).

- **Unspecified or undocumented model components:** Some processes relevant to evapotranspiration are not represented in CHTESSEL as implemented in ERA5-Land. The model does not include lateral subsurface water flow, groundwater dynamics, or any representation of the water table. Irrigation and anthropogenic water management are absent. No atmospheric CO_2 concentration is used in the ET calculation: although a photosynthesis scheme (A-gs) is included in CHTESSEL for land-atmosphere carbon dioxide exchange, the Jarvis-type canopy resistance remains the operational parameterisation for transpiration, with no coupling between stomatal conductance and CO_2 levels.

1.1.2 JRA-55

- **General information:** The Japanese 55-year Reanalysis (JRA-55) (Kobayashi et al., 2015) is a global atmospheric reanalysis product provided by the Japan Meteorological Agency (JMA), offering monthly ET data at approximately 0.57° ($\sim$55 km, TL319 spectral resolution on a reduced Gaussian grid) from 1958 to the present. The product used

here is the JRA-55 Monthly Mean Model Resolution Two-Dimensional Average Diagnostic Fields, specifically the evapotranspiration field. Land surface analysis fields in JRA-55 are generated by driving an offline version of the JMA Simple Biosphere (SiB) model (Sellers et al., 1986) with 3-hourly atmospheric forcing fields from the JMA Global Spectral Model (GSM), based on JMA's operational data assimilation system as of December 2009 (Kobayashi et al., 2015). Further product specifications are available in the JRA-55 product users' handbook (JMA, 2014).

- **ET scheme:** In SiB, the vegetation is represented by two distinct layers: an upper canopy layer (trees or shrubs) and a lower ground cover layer (grasses and herbaceous species), either or both of which may be present at a given location. The model solves energy balance equations for two prognostic temperatures: a canopy temperature and a ground surface temperature, the latter predicted using the force-restore method (Deardorff, 1978). Evaporation is calculated from the vapour pressure difference between the evaporating surface (assumed saturated) and the atmosphere, modulated by a series of resistances. Total evaporation comprises transpiration from both canopy and ground cover vegetation (controlled by stomatal resistances), direct evaporation from wet canopy and ground cover surfaces (interception stores), and bare soil evaporation. Here we use the total evaporation field. Canopy and ground surface evaporative fluxes depend explicitly on the near-surface atmospheric state. Relevant atmospheric variables include air temperature, humidity, wind speed, precipitation, and radiation. The fluxes also depend on prognostic land surface variables. These include canopy and ground temperatures, canopy and ground water storage, and aerodynamic and surface resistances.

- **Resistances:** The evaporative fluxes are regulated by a network of aerodynamic and surface resistances. Three aerodynamic resistances are defined: between the ground and the canopy air space, between the canopy air space and the atmospheric reference height, and a bulk boundary layer resistance at the leaf surface. These resistances depend on roughness lengths, wind speed, and reference height; within the canopy, a leaf drag coefficient and leaf shelter factor are included. The bulk boundary layer resistance additionally depends on a transfer coefficient and leaf area. Two vegetation (stomatal) resistances are defined, one for the upper canopy and one for the ground cover, both following a Jarvis-type formulation. They depend on leaf area index, leaf water potential, photosynthetically active radiation (derived from downward shortwave radiation), temperature, and atmospheric humidity. One soil surface resistance is defined for bare soil evaporation, dependent on the moisture content of the surface soil layer.

- **Soil scheme:** Soil moisture is predicted in three layers, with layer thicknesses and porosity defined per vegetation type (JMA, 2014): tree types (codes 1–5) use layers of 0.02, 1.48, and 2.0 m depth (total $\sim$3.5 m) with a porosity of 0.42 m^3 m^{-3}, while shrub and grassland types use shallower configurations (e.g., 0.02, 0.47, and 1.0 m for groundcover types; 0.02, 0.17, and 0.3 m for broadleaf shrubs with bare soil). Vegetation draws water from the soil via root extraction distributed across the layers, with separate contributions from canopy and ground cover transpiration. In the original SiB formulation (Sellers et al., 1986), infiltration is limited by the hydraulic conductivity of saturated soil, excess water is removed as surface overflow, and gravitational drainage occurs from the bottom layer; the thermal budget uses the force-restore method (Deardorff, 1978), with the deep soil temperature serving as an additional prognostic variable. However, it is not confirmed whether these specific formulations are retained in the JMA implementation used for JRA-55. The

method used for soil moisture initialisation in JRA-55 is not documented in Kobayashi et al. (2015); the original SiB employed climatological values from Willmott et al. (1985). No further detail on soil hydraulic parameterisation (e.g., water retention curves or unsaturated conductivity functions) could be identified in the available JRA-55 documentation.

- **Interception:** Two prognostic interception stores are represented: one on the canopy and one on the ground cover. Each collects liquid water from precipitation, with interception modelled using an exponential attenuation approach analogous to radiative transfer, assuming vertical flux and non-transmitting leaves. Water is lost from the interception stores through evaporation at the potential rate and drainage. When surface temperatures fall below freezing, the canopy store represents ice and the ground store represents snow water equivalent. However, (Kobayashi et al., 2015) do not provide detail on the specific mathematical formulation of interception within SiB, including storage capacities, throughfall parameterisation, or the equations governing evaporation from wet canopy surfaces.

- **Data and important information:** The offline SiB land surface model in JRA-55 is forced by 3-hourly atmospheric fields from the GSM forecast model, including pressure, temperature, humidity, and wind at the lowest model level, surface pressure, precipitation, downward solar and longwave radiation fluxes, and total cloud cover (Kobayashi et al., 2015, Section 3.2b). The atmospheric analysis uses four-dimensional variational data assimilation (4D-Var) with variational bias correction (VarBC) for satellite radiances (Kobayashi et al., 2015, Section 3.1); first-guess fields are produced at TL319 horizontal resolution ($\sim$55 km) with 60 vertical levels extending to 0.1 hPa, while analysis increments are computed at T106 resolution. Vegetation types are classified into 14 categories (JMA code table 252, codes 0–13) based on the SiB vegetation classification (Sellers et al., 1986); prescribed parameter values for each type (albedo, roughness length, stomatal resistance, and root distribution) follow Dorman and Sellers (1989). The source land cover dataset used for the vegetation map and the source and temporal treatment of leaf area index (LAI) in JRA-55 are not documented in Kobayashi et al. (2015). The vegetation map is static (constant field); no dynamic vegetation or time-varying land use is represented. Static ancillary fields include orography and sea surface temperature from COBE-SST (Ishii et al., 2005). Soil moisture has no direct observational constraint; it is corrected only indirectly through the snow depth analysis (Kobayashi et al., 2015, Section 7.2). In summary, ET in JRA-55 is governed by the 3-hourly meteorological forcing from the GSM (temperature, wind, radiation, humidity, precipitation, and cloud cover), prognostic land surface state variables (canopy and ground temperatures, soil moisture, interception water on canopy and ground cover, and snow water equivalent), and prescribed vegetation and soil properties.

- **Unspecified or undocumented model components:** JRA-55 employs a modified version of the Simple Biosphere model (SiB) originally introduced by Sellers et al. (1986). Although JMA substantially revised the SiB soil water, soil heat, and snow schemes (Hirai et al., 2007), these developments are not explicitly referenced in the main JRA-55 description of Kobayashi et al. (2015). As a result, it remains unclear which specific model developments were incorporated into the December 2009 version of the JMA Global Spectral Model used for JRA-55. Consequently, several aspects of the land-surface formulation, including the exact SiB physics and the full set of surface properties controlling resistance parameterisations, are only minimally documented in the standard JRA-55 references.

1.1.3 MERRA-2

- **General information:** MERRA-2 (Gelaro et al., 2017) is NASA's Modern-Era Retrospective Analysis for Research and Applications, version 2, produced by the Global Modeling and Assimilation Office (GMAO) using the GEOS-5.12.4 atmospheric data assimilation system. It provides global, sub-daily estimates of atmospheric and land surface conditions from 1980 to present at ∼50 km horizontal resolution on a $0.5^\circ \times 0.625^\circ$ output grid with 72 hybrid-eta vertical levels. MERRA-2 supersedes the original MERRA reanalysis and was designed to provide a viable near-real-time climate analysis while serving as a stepping stone toward a future integrated Earth system analysis. Key advances over MERRA include aerosol data assimilation, improved representations of the stratosphere and cryosphere, a global dry-mass conservation constraint, and the use of observation-corrected precipitation to force the land surface.

- **ET scheme:** Evapotranspiration in MERRA-2 is computed using the GEOS-5 Catchment land surface model (Koster et al., 2000), which explicitly resolves sub-grid-scale soil moisture variability and its effects on runoff and evaporation. The model distinguishes between transpiration, bare-soil evaporation, and canopy interception loss. ET is governed by the available soil water and the atmospheric demand, mediated through the surface turbulence scheme of Helfand and Schubert (1995) in MERRA-2 (replacing the Louis (1979) scheme used in the original MERRA).

- **Resistances:** Surface turbulent fluxes in MERRA-2 are computed using the Monin–Obukhov similarity framework of Helfand and Schubert (1995), which replaced the bulk aerodynamic scheme of Louis (1979) used in MERRA and MERRA-Land. This change affects the partitioning of the surface energy balance and contributes to differences in evapotranspiration and soil drying rates between MERRA-2 and its predecessors. No stomatal resistance or CO_2-dependent conductance scheme is implemented.

- **Soil scheme:** The land surface model is the GEOS-5 Catchment model (Koster et al., 2000), which uses hydrological catchments as its basic computational unit. Soil moisture is tracked in two layers: a thin surface layer of 0.05 m and a root zone layer of 1.0 m. Soil texture is taken from Reynolds et al. (2000), with hydraulic properties derived from pedotransfer functions adapted from Cosby et al. (1984) and depth-to-bedrock from GSWP-2. The saturated hydraulic conductivity decays vertically with a factor of 1.0 m^{-1}. Snow is represented in three layers tracking snow water equivalent, depth, and heat content, using the scheme of Stieglitz et al. (2001), with a minimum snow water equivalent parameter of 26 kg m^{-2}. A shallow unconfined groundwater table depth can additionally be diagnosed from the model prognostic variables.

- **Interception:** Rainfall interception is parameterised through a canopy interception reservoir in the Catchment model, with capacity set to LAI × 0.2 kg m^{-2}. The areal fraction of canopy leaves onto which large-scale and convective precipitation falls is set to 0.02 in both cases, a major revision from MERRA (values of 1.0 and 0.2 respectively) that substantially reduces the fraction of rainfall directly reevaporated from the canopy. The global average interception loss fraction in MERRA-2 is approximately 0.12, which is more realistic than MERRA's value of 0.33, and consistent with estimates from the Community Land Model (Reichle et al., 2017). Remaining overestimation relative to GLEAM-based

estimates is attributed partly to insufficient subdaily rainfall intensity in the corrected precipitation forcing, which inflates interception relative to what higher-intensity convective events would produce.

- **Data and important information:** MERRA-2 assimilates a comprehensive suite of conventional and satellite observations within a 3DVAR framework with a 6-hourly update cycle. Land surface precipitation is corrected with observational data products at low-to-mid latitudes, while model-generated precipitation is retained at high latitudes. Monthly LAI, greenness fraction, and land cover are prescribed climatologies; LAI is derived from AVHRR NDVI (1982–1998) and does not vary interannually. Land surface albedo is from an 8-day MODIS climatology. ET is modulated by temperature, humidity, wind, radiation, and soil moisture, but carries no signal from dynamic vegetation, CO_2 fertilisation, or LAI.

1.2 Remote Sensing based models

1.2.1 BESS v2

- **General information:** The Breathing Earth System Simulator version 2.0 (BESSv2.0) (Li et al., 2023) is a remote-sensing-based product providing daily ET data at 0.05° (∼5.5 km) resolution spanning 1982 to 2019. BESSv2.0 is developed and maintained by Seoul National University. BESS is a process-based, satellite-driven model that couples atmosphere and canopy radiative transfer, photosynthesis, stomatal conductance, and evapotranspiration through an iterative carbon–water–energy balance. Unlike reanalysis or offline land surface model products, BESS does not solve a soil water or energy balance; instead, it computes instantaneous land-atmosphere fluxes at the time of satellite overpass using satellite-derived surface properties and reanalysis meteorology, and temporally upscales these to daily sums. BESSv2.0 extends the temporal coverage of the earlier BESSv1.0 product (2000–2015, 1 km, 8-day) (Jiang and Ryu, 2016) back to 1982 through calibration of AVHRR datasets against MODIS, and includes new modules for ecosystem respiration and an optimality-based maximum carboxylation rate (V_{cmax}).

- **ET scheme:** BESS computes ET using the quadratic form of the Penman–Monteith equation embedded within a coupled carbon–water–energy balance module. The canopy is represented using a two-leaf (sunlit/shaded) scheme (De Pury and FARQUHAR, 1997; Ryu et al., 2011). Total evapotranspiration comprises transpiration from sunlit canopy, transpiration from shaded canopy, and soil evaporation (Jiang and Ryu, 2016). For each component, evaporation is driven by the available energy (net radiation minus ground heat storage), the vapour pressure deficit between the surface and the atmosphere, and resistance terms. The carbon–water–energy module integrates Farquhar–von Caemmerer–Berry (FvCB) photosynthesis for C3 plants (Farquhar et al., 1980) and the Collatz formulation for C4 plants (Collatz et al., 1992), the Ball–Berry stomatal conductance equation (Ball et al., 1987), and a two-leaf longwave radiative transfer model (Kowalczyk et al., 2006). Five intermediate variables-sunlit leaf temperature, shaded leaf temperature, soil temperature, intercellular CO_2 concentration, and aerodynamic resistance-are solved iteratively (three iterations per time step). The derived instantaneous estimates of ET at satellite overpass time are temporally upscaled to daily sums using a cosine function. In each land grid cell, fluxes are computed separately for C3 and C4 species and combined according to their fractional cover.

– **Resistances:** Transpiration is regulated by stomatal conductance (g_s), parameterised using the Ball–Berry formulation. In BESSv2.0, the slope m and initial intercept b_0 are parameterised using a look-up table (LUT) dependent on plant functional type (PFT) and climate zone (Li et al., 2023, Table S3). A water stress factor (f_w) downregulates the minimum stomatal conductance under dry conditions. The aerodynamic resistance (r_a) is computed from canopy height and wind speed and is updated iteratively within the energy balance module. No explicit soil surface resistance is documented for the soil evaporation component in BESS; soil evaporation is computed via the Penman–Monteith equation using the soil energy balance, with soil temperature as a prognostic variable in the iteration.

– **Soil scheme:** BESS does not include a soil hydrological model. There is no prognostic soil moisture, no Richards' equation or bucket-type water balance, and no representation of infiltration, drainage, runoff, or groundwater. Water availability effects on ET are represented solely through the atmospheric water stress factor (f_w) applied to stomatal conductance, which depends on relative humidity and vapour pressure deficit rather than on soil water content. Soil temperature is solved iteratively as part of the energy balance for the soil evaporation component, using an empirical ground heat storage function, but no multi-layer soil thermal scheme is included. The Harmonized World Soil Database (HWSD) and SoilGrids topsoil organic carbon stock (0–15 cm) are used only as inputs to the ecosystem respiration (TER) module, not for the ET calculation.

– **Interception:** Interception is not represented in BESS. There is no interception reservoir, no throughfall partitioning, and no evaporation from wet canopy surfaces. All precipitation-related processes are absent from the ET calculation.

– **Data and important information:** BESSv2.0 uses an extensive set of satellite and reanalysis datasets as input (Li et al., 2023, Table 1). Hourly ERA5 data provide air temperature, dewpoint temperature, and solar radiation (the latter used for the pre-MODIS period before 2001 and for gap-filling; for the MODIS period, BESS computes its own radiation products (BESS-Rad) from MODIS atmosphere products). Daily MODIS products provide aerosol optical depth (MOD04/MYD04_L2 C6), cloud properties (MOD06/MYD06_L2 C6), and atmospheric profiles including temperature and humidity (MOD07/MYD07_L2 C6). Visible, NIR, and shortwave albedo are from daily MODIS MCD43D59–61 (after 2001) and 8-day GLASS products (before 2000). Leaf area index, the most sensitive input variable for BESS flux estimates (Ryu et al., 2011), is derived from MODIS MCD15A2H (8-day) and MCD15A3H (4-day) after 2001, and from GLOBMAP LAI (half-monthly) before 2001, with pixel-wise inter-calibration against MODIS and cloud-contamination filtering. Monthly ambient CO_2 concentration maps are generated by harmonising OCO-2 XCO_2, GHG-CCI, and NOAA measurements. NCEP/NCAR Reanalysis wind speed data are used in the aerodynamic module. Land cover is from MCD12Q1 (IGBP, after 2001) and ESA-CCI (before 2001). The C3/C4 plant distribution uses the MsTMIP maize fraction map (Monfreda et al., 2008) and the global C4 grass fraction map (Still et al., 2003), both static (ca. 2000). Canopy height is from ICESat/GLAS (Simard et al., 2011), also static (2005). A global clumping index is from MODIS BRDF (Wei et al., 2019). Elevation is from SRTM. The maximum carboxylation rate ($V_{\mathrm{cmax}}^{25\mathrm{C}}$) for C3 plants is derived from an optimality-based model combining coordination theory and least-cost hypothesis (Jiang et al., 2020; Li et al., 2017), using 40-day running averages of environmental conditions; for C4 plants, a PFT-dependent LUT is retained (Jiang and

Ryu, 2016). In summary, ET in BESSv2.0 is governed by satellite-derived surface properties (LAI, albedo, clumping index, land cover, canopy height, and CO_2 concentration), reanalysis meteorology (air temperature, dewpoint temperature, wind speed, and solar radiation), and process-based coupling of photosynthesis, stomatal conductance, and energy balance. Importantly, neither precipitation, soil moisture, nor root-zone water availability enter the ET calculation directly; water stress is represented only through the atmospheric humidity-based f_w factor applied to stomatal conductance.

1.2.2 ETMonitor

- **General information:** ETMonitor (Zheng et al., 2022; Hu and Jia, 2015) is a global remote-sensing-based evapotranspiration product released by the Aerospace Information Research Institute, Chinese Academy of Sciences. The dataset provides daily ET at 1 km spatial resolution for 2000–2019. In the 2022 global implementation, ETMonitor was improved for global application by incorporating dynamic water and snow or ice cover, downscaled high-resolution soil moisture, improved soil heat flux estimation, and parameter calibration using global flux tower observations.

- **ET scheme:** ETMonitor estimates ET using a combined model driven by multi-source satellite observations and meteorological forcing, considering energy budget, water balance, and plant physiological controls on land–atmosphere exchange. Total ET is calculated as the sum of plant transpiration, soil evaporation, canopy rainfall interception loss, open-water evaporation, and snow or ice sublimation. For the soil–vegetation canopy system, transpiration and soil evaporation are estimated using the Shuttleworth–Wallace two-source scheme (Shuttleworth and Wallace, 1985) combined with a Jarvis-type canopy resistance formulation. Open-water evaporation and snow or ice sublimation are estimated using the Penman combination equation. Available energy is calculated as net radiation minus ground heat flux, and for vegetated surfaces the net radiation is partitioned among transpiration, soil evaporation, and canopy interception loss.

- **Resistances:** ETMonitor explicitly represents aerodynamic, canopy, and soil surface resistances. Aerodynamic resistances for canopy, soil, and air are calculated from wind speed, roughness length, and atmospheric stability corrections, with momentum partitioning additionally influenced by LAI (Hu and Jia, 2015). Canopy resistance is estimated with a Jarvis-type formulation in which minimum stomatal resistance is regulated by shortwave radiation, vapour pressure deficit, air temperature, and root-zone soil moisture. The key sensitivity parameters calibrated in the global implementation are the minimum stomatal resistance $r_{s,\min}$ and the vapour pressure deficit stress parameter K_D. Soil surface resistance is parameterized as a function of surface soil moisture saturation, minimum soil resistance, and a soil-dependent exponent b, with θ_{sat} and θ_{res} derived from soil-property maps.

- **Soil scheme:** In the global ETMonitor implementation, soil moisture is represented using a simplified two-layer soil scheme. The upper layer corresponds to the shallow surface depth sensed by microwave remote sensing, while the lower layer represents subsoil moisture reaching the root zone. Surface soil moisture is taken from ESA CCI and downscaled from 0.25° to 1 km using a Random Forest model. Root-zone soil moisture is then estimated from the relationship between surface and subsoil moisture following the simplified approach adopted for global-scale application. Thus,

ETMonitor includes soil moisture controls on transpiration and soil evaporation, but it does not use a fully prognostic multilayer soil-water balance model in the global 1 km product.

- **Interception:** Canopy rainfall interception loss is explicitly represented in ETMonitor and estimated using a revised Gash analytical model. The model treats interception loss as the portion of rainfall temporarily retained on the canopy and subsequently evaporated to the atmosphere, while the remaining rainfall reaches the ground as throughfall, dripping, or stemflow. In the global daily application, the revised Gash model is applied on a daily basis under the assumption of one storm per rainy day. The canopy and trunk are treated together in the revised formulation used here.

- **Data and important information:** ETMonitor is driven by multi-source remote sensing and meteorological forcing datasets. GLASS products provide LAI, albedo, and fractional vegetation cover. MODIS products provide annual land cover and seasonal snow cover, while dynamic water cover is taken from DGWCD and later global surface water extent products. Surface soil moisture is taken from ESA CCI, with ERA5 top-layer soil moisture used to fill missing values before downscaling to 1 km. Precipitation is taken from GPM. Canopy height is taken from GLAS. Meteorological forcing is derived from ERA5, including air temperature, dewpoint temperature, air pressure, wind speed, and downward shortwave and longwave radiation. Ground heat flux is estimated with a Random Forest model trained using FLUXNET2015 observations and driven by net radiation, LAI, air temperature, albedo, and saturated soil water content. The global implementation was calibrated and validated using flux tower observations from 251 sites across a wide range of climate regimes and plant functional types.

- **Unspecified or undocumented model components:** Although ETMonitor represents the main ET components explicitly, several processes remain simplified or only partly documented for the global product. Root-zone soil moisture is not directly observed but inferred from a simplified two-layer relationship with surface soil moisture. The global product does not use a full prognostic multilayer soil hydrology scheme, and groundwater dynamics, lateral subsurface flow, and detailed runoff routing are not represented as part of the ET estimation framework. Snow or ice sublimation is included, but evaporation from melting snow surfaces is neglected in the current study. Interception is represented through the revised Gash model, but the daily implementation assumes one storm per rainy day, which is a simplification.

1.2.3 GLEAM v4.1a

- **General information:** The Global Land Evaporation Amsterdam Model (GLEAM) (Miralles et al., 2025) is a global remote-sensing-based evaporation product that provides daily estimates at 0.1° spatial resolution from 1980 to 2023. The product provides not only total evaporation, but also several component fluxes and related variables such as soil moisture, potential evaporation, evaporative stress, and sensible heat flux.

- **ET scheme:** GLEAM4 estimates total land evaporation through four sequential modules that compute interception loss, potential evaporation, soil water content, and evaporative stress. Potential evaporation is calculated with the Penman equation. Actual evaporation is then obtained by applying a multiplicative evaporative stress factor to potential evaporation for bare soil and for the tall and short vegetation fractions within each grid cell. Total evaporation is partitioned

into transpiration, bare-soil evaporation, interception loss, open-water evaporation, evaporation over snow and ice, and condensation. Understorey bare-soil evaporation is represented through canopy radiation transmission based on the Beer Lambert law and leaf area index.

– **Resistances:** GLEAM4 does not formulate evapotranspiration through an explicit stomatal or canopy resistance model in the standard land-surface-model sense. Instead, atmospheric demand is represented through Penman potential evaporation and water limitation is imposed through the evaporative stress factor. The aerodynamic term enters through the bulk aerodynamic conductance in Penman's equation, approximated with Thom's equation under neutral atmospheric conditions. The conductance depends on wind speed, zero-plane displacement height, and roughness lengths for momentum and vapour. Displacement height and momentum roughness are derived from vegetation height, with an additional LAI dependence for vegetated fractions. The roughness length for vapour and heat is computed from the momentum roughness using a vegetation-specific kB^{-1} approach, with values of 5 and 8 for short and tall vegetation, respectively. The evaporative stress factor for tall and short vegetation is learned from eddy-covariance and sapflow observations using a deep neural network driven by root-zone soil moisture, vegetation optical depth, vapour pressure deficit, incoming solar radiation, air temperature, CO_2 concentration, wind speed, and LAI (Koppa et al., 2021).

item **Interception:** Rainfall interception loss is explicitly represented in GLEAM4 and is computed on rainy days. In GLEAM4, the previous interception approach based on Gash's analytical model is replaced by a globally constrained van Dijk–Bruijnzeel model. This formulation is constrained using satellite-observed vegetation dynamics through fPAR and LAI, together with potential evaporation and precipitation. A key update in GLEAM4 is that interception is computed separately for tall and short vegetation fractions, thereby accounting for sub-grid heterogeneity.

– **Data and important information:** GLEAM4 uses a multi-source forcing framework resampled to 0.1°. The main inputs listed in the paper are net radiation and shortwave incoming radiation from MSWX or CERES, air temperature from MSWX or AIRS, precipitation from MSWEP or IMERG, wind speed from ERA5, vapour pressure deficit from MSWX or AIRS, CO_2 concentration from CAMS, snow water equivalent from GlobSnow or NSIDC, surface soil moisture from ESA CCI, vegetation optical depth from VODCA v2, fPAR and LAI from MOD15A3H, vegetation height from GEDI/Landsat, land-cover fractions from MEaSURES and MOD44B, and soil properties from HiHydroSoil. The dataset includes 12 output variables: actual evaporation, transpiration, bare-soil evaporation, interception loss, open-water evaporation, condensation, evaporation over snow and ice, potential evaporation, evaporative stress, surface soil moisture, root-zone soil moisture, and sensible heat flux.

1.2.4 MODIS 16A2

– **General information:** The ET product is a remote-sensing-based terrestrial evapotranspiration dataset that provides annual ET estimates at 500 m spatial resolution from 2000 onward over global vegetated land surfaces. It is derived from MODIS observations and distributed by NASA through the LP DAAC. The year-end gap-filled version uses quality-screened and temporally gap-filled vegetation inputs to reduce missing-data effects in the standard product.

- **ET scheme:** The MOD16 algorithm estimates ET on a daily basis using the Penman–Monteith approach. Daily ET is calculated as the sum of daytime and nighttime fluxes, and vertically as the sum of soil evaporation, wet canopy evaporation, and plant transpiration from the dry canopy surface. Net radiation is partitioned between canopy and soil using vegetation cover fraction, represented by FPAR, and the algorithm separately accounts for evaporation from wet surfaces and transpiration from dry vegetation.

- **Resistances:** MOD16 explicitly represents aerodynamic and surface resistances within the Penman–Monteith framework. Aerodynamic resistance over the canopy is calculated following the Biome-BGC formulation, as a parallel combination of convective and radiative heat-transfer resistances, while the improved algorithm also includes a biome-dependent boundary layer resistance term. Surface conductance to transpiration is parameterized using biome-specific values from a Biome-Property-Lookup-Table (BPLUT), with stomatal constraints based mainly on minimum temperature and vapour pressure deficit. Wet canopy evaporation and soil evaporation are treated separately from dry-canopy transpiration, and the wet surface fraction is estimated from relative humidity, constrained to zero when relative humidity is below 70%.

- **Soil scheme:** MOD16 is not a soil hydrology model and does not simulate a prognostic soil water balance. Instead, soil enters the ET calculation mainly through soil heat flux, the wet surface fraction, and empirical constraints on soil evaporation. In the improved MOD16 algorithm, soil heat flux is estimated as a function of available energy, temperature, and vegetation cover fraction rather than through an explicit subsurface heat and water transport scheme.

- **Interception:** Interception is represented through evaporation from the wet canopy surface. In the improved MOD16 formulation, ET includes evaporation of precipitation intercepted by the canopy before it reaches the ground, and this wet canopy evaporation is treated separately from transpiration through the dry canopy surface. The wet fraction of the canopy is derived from relative humidity, with no wet surface assumed when relative humidity is below 70%. Evaporation from the wet canopy is calculated as a potential evaporation process regulated by aerodynamic and wet canopy resistances. Interception loss in MOD16 is represented through wet-canopy evaporation and depends primarily on relative humidity through the wet surface fraction, as well as on leaf area index, vegetation cover fraction, available energy, vapour pressure deficit, and biome-dependent aerodynamic and wet-canopy conductance parameters.

- **Data and important information:** MOD16A3GF uses daily meteorological reanalysis data together with MODIS vegetation and surface-property inputs. The key remote-sensing inputs are FPAR, LAI, albedo, and land-cover classification, while the main meteorological forcings are downward shortwave radiation, air temperature, vapour pressure deficit, relative humidity, and wind speed. These variables regulate the partitioning of ET into wet canopy evaporation, plant transpiration, and soil evaporation through their effects on available energy, wet surface fraction, aerodynamic resistance, and biome-specific conductance parameters defined in the BPLUT. Land cover determines biome type and therefore the parameter values used in the ET calculation. The standard MOD16 algorithm does not explicitly account for atmospheric CO_2 concentration as a direct control on ET.

1.3 Hydrological and Land Surface Model based products

1.3.1 FLDAS

- **General information:** FLDAS Noah Land Surface Model L4 Global Monthly $0.1^\circ \times 0.1^\circ$ (MERRA-2 and CHIRPS) (FLDAS_NOAH01_C_GL_M) is a land-surface-model-based product that provides monthly land-surface variables, including evapotranspiration, at 0.1° spatial resolution from January 1982 onward. The dataset is produced within the Famine Early Warning Systems Network (FEWS NET) Land Data Assimilation System (FLDAS) (McNally et al., 2017) and is based on simulations from the Noah version 3.6.1 land surface model (Niu et al., 2011).

- **ET scheme:** In FLDAS, evapotranspiration is simulated by the Noah v3.6.1 land surface model within the NASA Land Information System rather than by a separate FLDAS-specific ET algorithm. Noah represents land–atmosphere exchange through coupled energy and water balances and simulates ET from multiple surface sources, including vegetation transpiration, bare-soil evaporation, canopy water evaporation, and snow-related fluxes. In the Noah framework, transpiration is linked to vegetation condition through green vegetation fraction and canopy conductance, whereas bare-soil evaporation is strongly constrained by moisture availability in the upper soil layer. Nevertheless, the standard FLDAS documentation does not provide the exact governing equations or a detailed ET-component partitioning for the global Noah product.

- **Resistances:** The FLDAS README does not explicitly document the resistance formulation, but the Noah model documentation indicates that transpiration is controlled using a Jarvis-type big-leaf canopy conductance approach. In this formulation, canopy conductance depends on soil moisture availability and atmospheric conditions, including solar radiation, temperature, and humidity. Noah also includes surface exchange parameterizations affected by roughness and thermal roughness length, and these influence the turbulent transfer of heat and moisture between land and atmosphere. Thus, in FLDAS the resistance framework should be attributed to Noah rather than described as a separate FLDAS-specific scheme.

- **Resistances:** In FLDAS, evapotranspiration is controlled by aerodynamic exchange and canopy conductance parameterizations inherited from the Noah land surface model. Plant transpiration is represented through a Jarvis-type big-leaf canopy conductance scheme, in which canopy conductance responds to soil moisture stress and atmospheric conditions, particularly solar radiation, air temperature, and humidity. Vegetation effects are represented through green vegetation fraction and leaf area index, which modify canopy conductance and thereby transpiration. Surface exchange of heat and moisture is further influenced by roughness-dependent transfer parameterizations, including thermal roughness length. For bare soil, evaporation is limited by moisture availability in the upper soil layer and decreases nonlinearly as the soil surface dries, reflecting the increasing resistance imposed by a dry surface layer.

- **Soil scheme:** In FLDAS, soil water and heat are represented with an explicit four-layer soil scheme at 0–10, 10–40, 40–100, and 100–200 cm depth. Soil moisture and soil temperature are represented as prognostic variables in each layer, and the scheme is coupled to infiltration, surface runoff, subsurface runoff, and soil heat transfer. It also includes frozen-

soil and snow-related physics, allowing soil-water and snow storage to influence land–atmosphere exchange. Root-zone water availability is therefore represented through the multilayer soil profile rather than through a single bulk soil store.

- **Interception:** Interception is represented through Noah's single-layer prognostic canopy water store. Precipitation is first intercepted by the vegetation canopy up to a maximum capacity that scales linearly with leaf area index (0.5 mm per unit LAI), with excess water dripping instantaneously to the ground as throughfall. Evaporation from the wet canopy proceeds at the potential rate and takes priority over transpiration; as the canopy wets, transpiration is progressively suppressed through a power-law wet-fraction factor (exponent 0.5), ceasing when the canopy store is full. The scheme does not distinguish between liquid and frozen interception, does not represent stemflow, and does not account for rainfall intensity or canopy architecture in determining storage capacity. Because Noah employs a combined soil–vegetation surface layer without a separate canopy energy balance, intercepted water evaporates at the bulk skin temperature rather than at a distinct canopy temperature.

- **Data and important information:** The global FLDAS Noah product is forced by MERRA-2 reanalysis meteorology (near-surface air temperature, specific humidity, surface pressure, wind speed, downward shortwave and longwave radiation) with precipitation replaced by CHIRPS daily rainfall, temporally disaggregated to 6-hourly time steps via the NASA Land Data Toolkit (McNally et al., 2017). Land cover parameters are derived from the IGBP and UMD vegetation classifications (MODIS and AVHRR, respectively). Soil properties are prescribed per soil type following standard Noah STATSGO-FAO texture classifications, though the specific soil dataset for the global FLDAS configuration is not documented. The simulation was initialised on 1 January 1982 from a FLDAS/Noah model climatology. ET is modulated by the atmospheric forcing and by internally simulated land states (soil moisture, vegetation fraction, snow cover). Atmospheric CO2 concentration is not used in the ET calculation.

- **Unspecified or undocumented model components:** The FLDAS product-level documentation (McNally et al., 2017) identifies Noah v3.6.1 as the underlying LSM and lists forcing and output variables, but does not reproduce the governing equations or parameterisation details for ET. Specific formulations for aerodynamic exchange, stomatal conductance, root water uptake, soil hydraulic functions, and snow-surface sublimation must therefore be inferred from the general Noah literature. The vegetation parameters used in the FLDAS global run — including the land cover classification, LAI source and temporal treatment, and roughness lengths — are likewise not specified in the product description. The vegetation parameters used in the FLDAS global run (land cover classification, LAI source, roughness lengths) are also not specified in the product description.

- **Note:** GLDAS-Noah v 2.1 and FLDAS both rely on the Noah model and use NASA LIS 7 as the underlying software framework, FAO-based soil parameters, and provide similar input and output variables. Differences are the meteorological forcing (MERRA-2 + CHIRPS in FLDAS versus GDAS + GPCP + AGRMET in GLDAS), the spatial resolution (0.1° versus 0.25° or 1.0°), the temporal coverage (1982–present versus 2000–present), and the Noah model version (3.6.1 in FLDAS versus 3.6 in GLDAS-2.1).

1.3.2 GLDAS-CLSM v2.1

- **General information:** GLDAS Catchment Land Surface Model L4 monthly 1.0° × 1.0° V2.1 (GLDAS_CLSM10_M) (Li et al., 2020) is a land-surface-model-based product that provides monthly land-surface variables at 1° spatial resolution from January 2000 to present. It is a component of the NASA Global Land Data Assimilation System (GLDAS-2.1) and is generated by temporal averaging of 3-hourly simulations from the Catchment-F2.5 land surface model run offline within the Land Information System (LIS) Version 7. The global domain extends from 60°S to 90°N.

- **ET scheme:** In GLDAS-CLSM v2.1, evapotranspiration is simulated by the Catchment-F2.5 land surface model through coupled surface water and energy balances. The model operates on hydrological catchments, within which the land surface is dynamically partitioned into saturated, transitional, and wilting fractions according to sub-grid hydrological conditions (Koster et al., 2000). Different evaporation and runoff formulations are applied across these fractions, allowing ET to respond to both atmospheric forcing and spatial variations in soil moisture. The model also includes a three-layer snow scheme that affects snow storage, melt, refreezing, surface energy. Total ET is partitioned into canopy water evaporation, vegetation transpiration, and direct bare-soil evaporation.

- **Resistances:** In GLDAS-CLSM v2.1, evapotranspiration is controlled by aerodynamic exchange and canopy conductance within the Catchment-F2.5 model. Canopy conductance is calculated separately for the different hydrological regimes from meteorological forcing, vegetation phenology, and regime-specific temperature and moisture conditions, and these conductances are used in the corresponding energy-balance calculations. Aerodynamic conductance is also represented explicitly. However, the standard product references do not fully specify the exact resistance equations for this GLDAS configuration, and neither a separate soil surface resistance formulation nor an explicit CO_2 dependence of canopy conductance is clearly documented.

- **Soil scheme:** The Catchment LSM uses a unique hydrological framework in which the vertical soil moisture profile is determined by an equilibrium profile from the surface to the water table, plus two deviation variables describing departures from equilibrium in a 2-cm surface layer and a 1-m root-zone layer (Koster et al., 2000). The water table depth is a prognostic variable. The subgrid spatial variability of soil moisture is related to topographic index statistics, allowing the dynamic partitioning into saturated, transitional, and wilting subareas. Runoff is generated through both saturation-excess (Dunne) and infiltration-excess (Horton) mechanisms. Soil temperature is simulated in six layers from the surface to 13 m depth (Tao et al., 2017). The soils database is from Reynolds et al. (2000).

- **Interception:** The Catchment LSM includes a canopy interception reservoir. Precipitation is first intercepted by the canopy up to a storage capacity related to leaf area index. The intercepted water may subsequently evaporate back to the atmosphere, while the remaining water reaches the ground surface as throughfall or canopy drainage. Canopy water storage is represented as a prognostic variable in the model output.

– **Data and important information:** The GLDAS-2.1 simulation is forced by NOAA/GDAS atmospheric analysis fields (Derber et al., 1991) providing near-surface air temperature, humidity, pressure, and wind speed; disaggregated GPCP V1.3 Daily Analysis precipitation (Adler et al., 2003; Huffman et al., 2001); and AGRMET radiation fields (shortwave and longwave) from March 2001 onward. From January 2000 to February 2001, only GDAS and GPCP forcing were used. The simulation was initialised on 1 January 2000 using conditions from the GLDAS-2.0 simulation. The soils database is from Reynolds et al. (2000), and the elevation database is GTOPO30. Land surface parameters use MODIS-based datasets, and the data were post-processed with the MOD44W MODIS land mask. Atmospheric CO_2 concentration is not used in the ET calculation.

– **Unspecified or undocumented model components:** The GLDAS product-level documentation (Rodell et al., 2004) and README identify the Catchment-F2.5 LSM and list forcing and output variables, but do not reproduce the governing equations for ET. The specific formulations for aerodynamic resistance, canopy conductance (stomatal resistance function and its environmental stress factors), and bare soil evaporation must be inferred from the original Catchment LSM literature (Koster et al., 2000). The vegetation parameters used in the GLDAS-CLSM global run (land cover classification, LAI source and temporal treatment, greenness fraction) are noted as MODIS-based but are not fully specified in the product documentation. The detailed snow interception parameterisation (whether canopy snow loading, unloading, and sublimation are represented) is not documented. The CO_2 dependence of stomatal conductance is absent, consistent with the SiB-based (not SiB2) formulation. Irrigation and anthropogenic water management are not represented. In the standard product-level documentation for GLDAS-CLSM v2.1, the exact resistance formulations and soil-scheme parameterizations are not described in detail. In particular, the equations for aerodynamic resistance, canopy conductance, and bare-soil evaporation are not documented clearly.

1.3.3 GLDAS-NOAH v2.1

– **General information:** GLDAS Noah Land Surface Model L4 monthly $0.25° \times 0.25°$ V2.1 (GLDAS_NOAH025_M) (Rodell et al., 2004; Beaudoing and Rodell, 2020) is a land-surface-model-based product providing monthly ET data at $1°$ spatial resolution from January 2000 to present. It is a component of the NASA Global Land Data Assimilation System Version 2. The monthly product was generated through temporal averaging of 3-hourly data simulated with Noah 3.6 in the Land Information System (LIS) Version 7 (Kumar et al., 2006). GLDAS-2.1 is an open-loop simulation (no data assimilation) forced by a combination of model and observation-based data. Noah is run offline, without coupling to the atmosphere.

– **ET scheme:** The Noah LSM computes total evapotranspiration as the sum of three components: direct evaporation from bare soil, transpiration from the vegetation canopy, and evaporation of canopy-intercepted water (Chen et al., 1996; Ek et al., 2003). These are weighted by the green vegetation fraction and bare soil fraction. Potential evaporation is computed using the Penman-based energy balance approach. Transpiration is derived from the potential evaporation modified by a canopy resistance factor that accounts for environmental stress. Canopy evaporation from intercepted water proceeds

at the potential rate and takes priority over transpiration. Direct soil evaporation depends on top-layer soil moisture availability. Noah uses a single combined soil–vegetation surface ("big-leaf") without a separate canopy energy balance; a single skin temperature governs the surface energy budget.

– **Resistances:** Aerodynamic resistance is computed using Monin–Obukhov similarity theory, with roughness lengths for momentum and heat prescribed per vegetation type. Canopy (stomatal) resistance follows a Jarvis-type formulation (Jarvis, 1976; Chen et al., 1996) in which the minimum stomatal resistance is modified by multiplicative stress functions for solar radiation, vapour pressure deficit, air temperature, and soil moisture availability. The soil moisture stress function depends on root-zone soil water content relative to the wilting point and reference (field capacity) values. No explicit soil surface resistance is defined; bare soil evaporation is parameterised through a moisture-dependent exponent that reduces evaporation linearly or nonlinearly between saturated and dry soil conditions (Ek et al., 2003). The stomatal resistance formulation does not include CO_2 dependence.

– **Soil scheme:** Noah uses four soil layers with thicknesses of 0.10, 0.30, 0.60, and 1.00 m (total depth 2.0 m). Soil moisture is predicted using the diffusivity form of Richards' equation, with hydraulic properties (porosity, saturated hydraulic conductivity, wilting point, field capacity) prescribed per soil texture type. Root water uptake for transpiration is distributed across the root-zone layers. Surface runoff is generated using a simple water balance approach (Schaake et al., 1996); subsurface drainage from the bottom layer follows a free-drainage formulation. Noah simulates frozen soil processes, tracking both liquid water and ice content in each layer; frozen ground reduces infiltration capacity. Soil temperature is predicted in the same four layers using the thermal diffusion equation.

– **Interception:** Interception is represented through a single-layer prognostic canopy water store (Chen et al., 1996). Precipitation is first intercepted by the canopy up to a maximum capacity that scales linearly with LAI. Excess water drips instantaneously to the ground as throughfall. Evaporation from the wet canopy proceeds at the potential rate and takes priority over transpiration; as the canopy wets, transpiration is progressively suppressed through a power-law wet-fraction factor. The scheme does not distinguish between liquid and frozen interception and does not represent stemflow or snow interception on the canopy. The snow scheme simulates accumulation, compaction, sublimation, and melt. Snowmelt contributes to infiltration and runoff. Patchy snow cover is represented through a snow cover fraction that affects the surface energy balance and the partitioning between snow sublimation and soil/vegetation evaporation from non-snow-covered areas (Ek et al., 2003). The snow scheme does not include canopy snow interception.

– **Data and important information:** The atmospheric forcing, ancillary datasets, initialisation and post-processing are identical to those used for GLDAS-CLSM v2.1. ET is modulated by the atmospheric forcing and by internally simulated land states, including soil moisture and temperature across four layers, soil ice content, canopy water content, snow water equivalent, snow cover fraction, and skin temperature, as well as prescribed surface properties including vegetation type, green vegetation fraction, LAI, roughness length, minimum stomatal resistance, and root depth. The green vegetation fraction partitions the grid cell between vegetated and bare soil contributions, directly controlling the relative weight of

transpiration versus bare soil evaporation. Canopy wetness shifts latent heat flux from the stomata-controlled transpiration pathway to the resistance-free interception evaporation pathway. Frozen soil reduces liquid water availability for root uptake, suppressing transpiration in cold seasons. Patchy snow cover partitions the surface between sublimation and soil/vegetation evaporation. Atmospheric CO_2 concentration is not used in the ET calculation.

- **Unspecified or undocumented model components:** The GLDAS product-level documentation (Rodell et al., 2004) and the GLDAS-2 README identify Noah 3.6 as the underlying LSM and list forcing and output variables, but do not reproduce the governing equations for ET. The specific formulations for stomatal resistance stress functions, bare soil evaporation parameters (FXEXP), and the canopy interception capacity must be inferred from the Noah LSM literature (Chen et al., 1996; Ek et al., 2003; Mahrt and Ek, 1984). The LAI source and its temporal treatment (monthly climatology vs. satellite-derived) are not fully specified in the product description. No CO_2 physiological effect on stomatal conductance is included. Irrigation and anthropogenic water management are not represented. The Noah model in GLDAS does not include groundwater or lateral subsurface flow.

- **Note:** GLDAS-Noah v 2.1 and FLDAS both rely on the Noah model and use NASA LIS 7 as the underlying software framework, FAO-based soil parameters, and provide similar input and output variables. Differences are the meteorological forcing (MERRA-2 + CHIRPS in FLDAS versus GDAS + GPCP + AGRMET in GLDAS), the spatial resolution (0.1° versus 0.25° or 1.0°), the temporal coverage (1982–present versus 2000–present), and the Noah model version (3.6.1 in FLDAS versus 3.6 in GLDAS-2.1).

1.3.4 GLDAS-VIC v2.1

- **General information:** GLDAS Variable Infiltration Capacity (VIC) Land Surface Model L4 monthly $1.0° \times 1.0°$ V2.1 (GLDAS_VIC10_M) (Rodell et al., 2004) is a land-surface-model-based product providing monthly ET data at 1° spatial resolution from January 2000 to present. The monthly product was generated through temporal averaging of 3-hourly data simulated with VIC 4.1.2 in the Land Information System (LIS) Version 7 (Kumar et al., 2006). GLDAS-2.1 is an open-loop simulation (no data assimilation) forced by a combination of model and observation-based data. VIC is run offline, without coupling to the atmosphere.

- **ET scheme:** VIC computes evapotranspiration using the Penman–Monteith equation (Liang et al., 1994). Sub-grid heterogeneity in land cover is represented by multiple vegetation tiles within each grid cell, each with its own energy and water balance. Total ET comprises three components: evaporation of canopy-intercepted water, transpiration from vegetation, and evaporation from bare soil. Transpiration is computed separately for each vegetation tile using the Penman–Monteith equation with a canopy resistance that depends on environmental stress factors. Bare soil evaporation from the top soil layer follows the ARNO formulation (Franchini and Pacciani, 1991). Each component is weighted by the respective land surface coverage fraction. VIC computes potential evapotranspiration as the area-weighted sum of potential

transpiration and potential soil evaporation; potential transpiration uses the current vegetation's architectural resistance and LAI to compute canopy resistance in the absence of moisture limitation.

– **Resistances:** Aerodynamic resistance is computed from wind speed, roughness length, and displacement height following standard Monin–Obukhov similarity theory. Canopy (stomatal) resistance follows a Jarvis-type multiplicative formulation (Liang et al., 1994), in which a minimum stomatal resistance is scaled by LAI and modified by dimensionless stress functions for photosynthetically active radiation, air temperature, vapour pressure deficit, and soil moisture. The soil moisture stress function reduces transpiration linearly between a critical soil moisture content (above which transpiration is unstressed) and the permanent wilting point (below which stomata close). The architectural resistance accounts for the within-canopy transfer of water vapour from the leaf interior to the canopy air space. No explicit soil surface resistance is formulated; bare soil evaporation is controlled implicitly through the ARNO moisture-dependent formulation applied to the top soil layer. The standard VIC formulation does not include CO_2 dependence of stomatal conductance.

– **Soil scheme:** Soil is represented by a three-layer scheme (Liang et al., 1996). The surface is 0-0.3 m, and the second and third layers are spatially variable. Infiltration into the top layers is governed by the variable infiltration capacity (VIC) curve, a power-law relationship between sub-grid soil moisture storage capacity and the fraction of a grid cell that is saturated (Liang et al., 1994). Gravity-driven drainage between layers follows the Brooks–Corey relationship. Baseflow from the bottom layer is parameterised using the ARNO formulation (Franchini and Pacciani, 1991). Root water uptake for transpiration is distributed across layers within the root zone according to prescribed root fraction profiles. Soil hydraulic properties (porosity, saturated hydraulic conductivity, Brooks–Corey exponents, field capacity, wilting point) are prescribed per soil type. VIC can simulate frozen soil processes including the effects of soil ice on infiltration and drainage (Cherkauer et al., 2003).

– **Interception:** VIC includes a single-layer canopy interception store for each vegetation tile. Precipitation is first intercepted by the canopy up to a maximum capacity determined by LAI; excess precipitation falls through as throughfall. Intercepted water evaporates at the potential rate (Penman–Monteith with zero canopy resistance). The canopy water balance is updated at each model time step. VIC also represents snow interception on the canopy; the snow model accounts for accumulation and melt of snow on the canopy and on the ground separately. Snow can accumulate on both the canopy (canopy snow interception) and the ground surface. Sub-grid variability in snow cover due to elevation is represented through snow/elevation bands, which allow different precipitation and temperature lapse rates across elevation zones within a grid cell.

– **Data and important information:** The atmospheric forcing, ancillary datasets, initialization and post-processing steps are identical to those used for GLDAS-CLSM v2.1. The GLDAS-2.1 VIC simulation is forced by NOAA/GDAS atmospheric analysis fields (Derber et al., 1991) (near-surface air temperature, humidity, pressure, wind speed), disaggregated GPCP V1.3 precipitation (Adler et al., 2003; Huffman et al., 2001), and AGRMET radiation fields from March 2001

onward; only GDAS and GPCP were used from January 2000 to February 2001. ET is modulated by the atmospheric forcing, internally simulated land states (soil moisture across three layers, soil temperature, soil ice content, canopy water storage, snow water equivalent and snow cover fraction), and prescribed surface properties (vegetation type, LAI, greenness fraction, root depth and fraction, roughness length, minimum stomatal resistance, architectural resistance). The dynamic partitioning of each grid cell into multiple vegetation tiles and a bare soil fraction further modulates the relative contributions of transpiration, canopy evaporation, and bare soil evaporation. Snow cover fraction affects the partitioning between sublimation and soil/vegetation evaporation. Atmospheric CO_2 concentration is not used in the ET calculation.

- **Unspecified or undocumented model components:** The GLDAS product-level documentation (Rodell et al., 2004) and the GLDAS-2 README identify VIC 4.1.2 as the underlying LSM and list forcing and output variables, but do not reproduce the governing equations for ET. The specific formulations for canopy resistance stress functions, bare soil evaporation, and snow interception/sublimation must be inferred from the VIC model literature (Liang et al., 1994, 1996; Cherkauer et al., 2003). The vegetation parameters used in the GLDAS-VIC global run (land cover classification, LAI source and temporal treatment, root depths and fractions) are noted as MODIS-based but not fully specified. Whether the frozen soil module is active in the GLDAS-2.1 VIC configuration is not documented. Irrigation and anthropogenic water management are not represented. No CO_2 physiological effect on stomatal conductance is included.

1.3.5 TerraClimate

- **General information:** TerraClimate (Abatzoglou et al., 2018) is a global terrestrial dataset providing monthly ET_0 and ET at $\sim$4 km ($1/24^\circ$) spatial resolution spanning 1958 to present. TerraClimate combines high-spatial-resolution climatological normals from WorldClim (Hijmans et al., 2005) with time-varying monthly anomalies from ERA5 (v1.1) or CRU Ts4.0/JRA-55 (v1.0) through climatically aided interpolation. ET_0 computed using the ASCE Penman–Monteith equation for a short reference crop. ET is derived from a modified Thornthwaite–Mather climatic water balance model using ET_0, precipitation, temperature, and plant-extractable soil water capacity.

- **ET scheme:** Reference evapotranspiration (ET_0) is calculated using the Penman–Monteith approach, which is energy-balance based and considered more appropriate than purely temperature-based metrics for estimating potential water loss. ET_0 assumes a reference grass surface uniformly across space. To account for reduced surface water flux under snow cover or prior to the growing season, ET_0 is modified using an empirical temperature-based relationship that accounts for precipitation phase changes.

- **Resistances:** Not specified. The Penman–Monteith formulation is applied assuming a standard reference grass surface; no explicit documentation of canopy or aerodynamic resistance parameterisations is provided beyond what is implied by the reference surface assumption.

- **Soil scheme:** A one-dimensional modified Thornthwaite–Mather climatic water balance model (WBM) is used. It operates as a single-bucket model on a monthly timestep, tracking the interplay of precipitation, ET_0, soil moisture storage,

and snowpack. Soil water is extracted in months where ET_0 exceeds liquid water supply, with extraction efficiency declining exponentially as the ratio of soil water to extractable soil water capacity decreases. Plant extractable soil water storage capacity is sourced from Wang-Erlandsson et al. (2016) at 0.5° resolution, bilinearly interpolated to the TerraClimate grid, with a lower bound of 10 mm and a default of 50 mm where data are absent.

- **Interception:** Not specified. The WBM does not explicitly document an interception scheme. Precipitation is partitioned into liquid and solid phases using an empirical temperature-based transformation, and 5% of cumulative rainfall and snowmelt each month is assigned as direct runoff regardless of soil conditions, but no canopy interception component is described.

- **Data and important information:** TerraClimate draws on three primary source datasets: WorldClim v2 (1/24° monthly normals, 1970–2000), CRU Ts4.0 (0.5° monthly time series, 1958–2015), and JRA-55 reanalysis (1.25°, 1958–2015). CRU Ts4.0 is prioritised for temperature, precipitation, and vapour pressure anomalies over land; JRA-55 fills gaps where CRU has no contributing stations, and supplies wind speed and solar radiation anomalies exclusively. Ancillary data on the number of CRU stations contributing to anomaly fields are provided as a measure of uncertainty. ET_0 is driven by temperature, solar radiation, and vapour pressure, but no dynamic LAI, CO_2 effects, or vegetation structural responses are represented.

1.4 Composite and Machine learning based models

1.4.1 CAMELE

Collocation-Analyzed Multi-source Ensembled Land Evapotranspiration Data (CAMELE) is a combinational product providing monthly ET data at a 0.25° x 0.25° scale spanning 2000-2020 (Li et al., 2024). CAMELE uses ERA5-Land (used in this study as well), FLUXCOM, PMLV2, GLDAS-NOAH, GLDAS-CLSM, GLDAS-VIC version 2.0 and 2.1 (used in this study as well) and GLEAM 3.7 a . The optimal weight for each product was calculated using collocation.

1.4.2 SynthesizedET

SynthesizedET is a combinational product providing monthly ET data at a kilometre spatial resolution spanning 1982 to 2019 (Elnashar et al., 2021). SynthesizedET combined four ET products, namely Penman–Monteith–Leuning (PML), the operational Simplified Surface Energy Balance (SSEBop), the Moderate Resolution Imaging Spectroradiometer (MODIS, MOD16A2105), and the Numerical Terradynamic Simulation Group (NTSG). Since SSEBop and MOD16A2105 have a 1000 m × 1000 m spatial resolution, PML was upscaled and NTSG was downscaled by pixel average and nearest neighbour resampling techniques in Google Earth Engine (GEE), respectively. For the years 1982 to 2000 SynthesizedET was fully contributed by NTSG. For the years 2001 and 2002 SynthesizedET was contributed by the simple means of MOD16A2105 and NTSG. For the years 2003-2017 SynthesizedET is the simple mean of PML and SSEBop. For the years 2018 and 2019 SynthesizedET was fully contributed by SSEBop.

2 Supplementary Method Figures and Tables

Trend analyses were stratified across multiple environmental domains to capture spatial heterogeneity in evapotranspiration dynamics. We used (i) updated Intergovernmental Panel on Climate Change (IPCC) reference regions v4 (Iturbide et al., 2020); (ii) Köppen–Geiger climate classes (Beck et al., 2018); (iii) elevation classes adapted from (Hersbach et al., 2020) and used as in (Markonis et al., 2024); and (iv) evaporation quantiles based on the ET deciles of the ensemble mean. All classifications were harmonized to the 0.25° grid used for the ET datasets and uploaded to Zenodo.

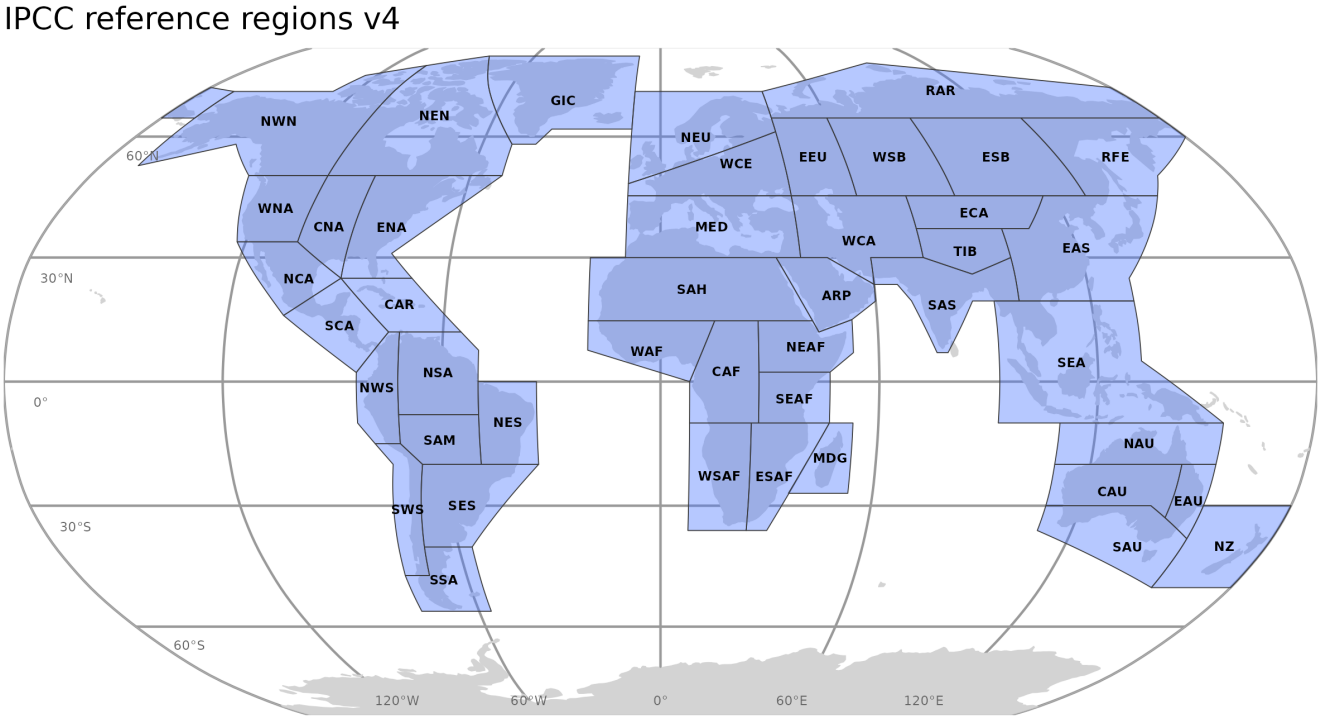

Figure S1. Maps of reference regions defined by the Intergovernmental Panel on Climate Change (IPCC) (Iturbide et al., 2020).

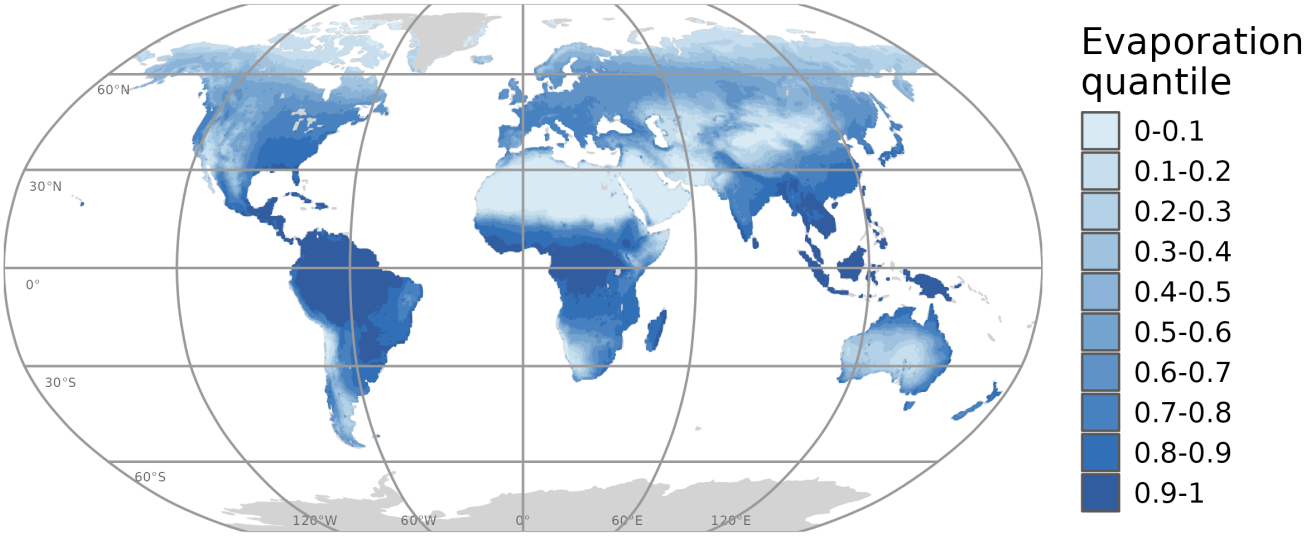

Figure S2. Maps of evaporation quantiles.

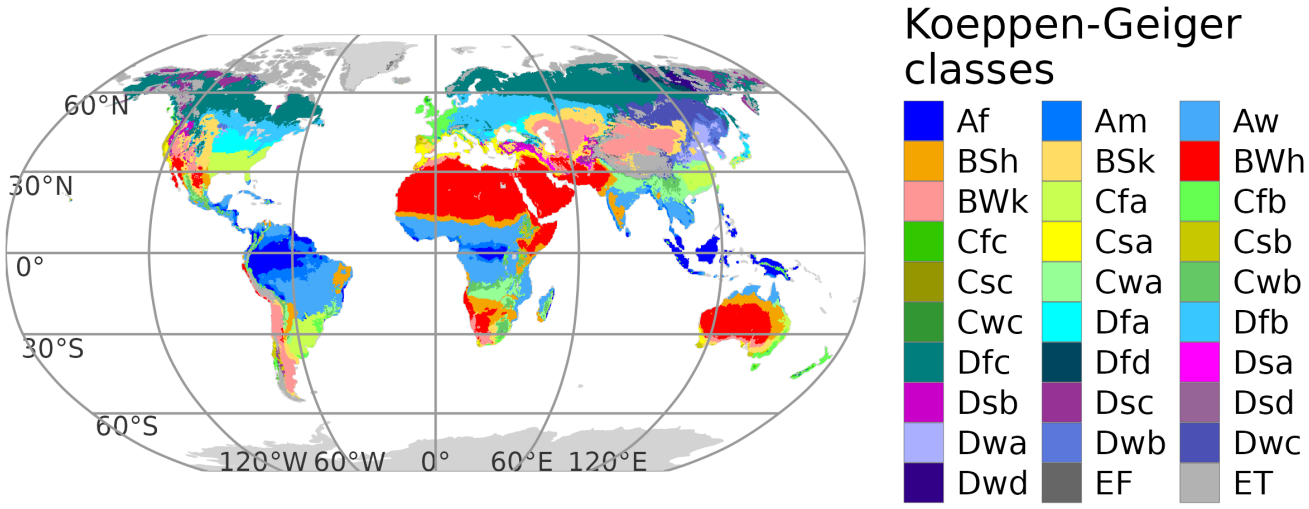

Figure S3. Maps of Köppen–Geiger classes as defined by (Beck et al., 2018).

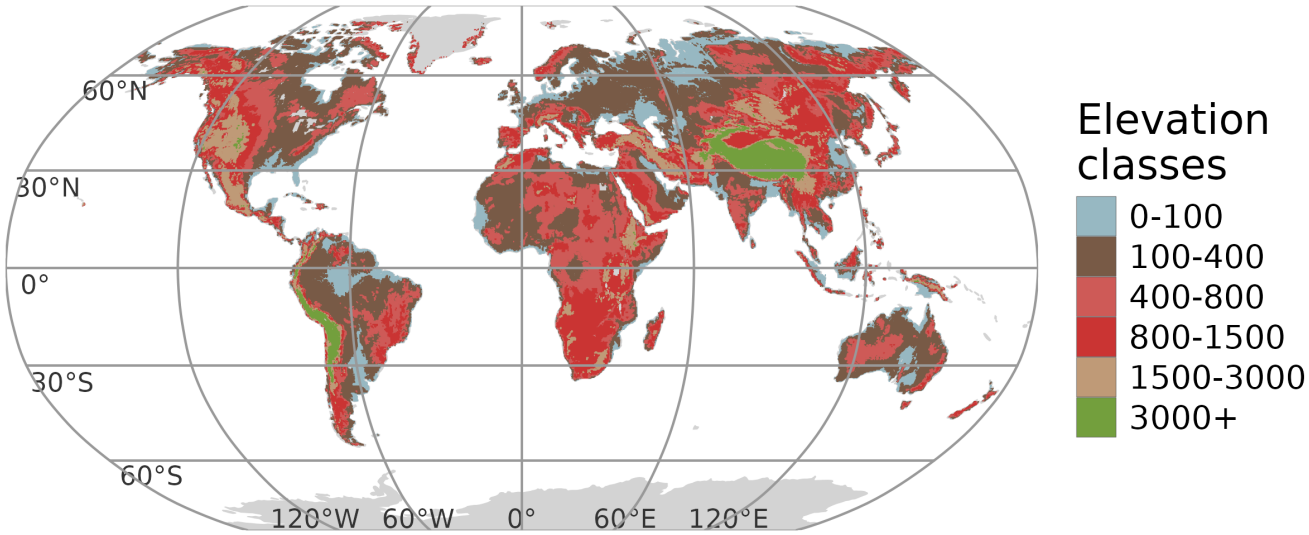

Figure S4. Maps of elevation classes.

3 Supplementary Result Figures and Tables

3.1 Ensemble trend estimates

Table S3. Area fractions of the symmetric quartile ratio $\max(|Q75|, |Q25|) / \min(|Q75|, |Q25|)$.

Ratio of symmetric inner quartiles	Area fraction (%)
(1,3.3]	43.8
(3.3,5]	17.4
(5,10]	18.9
(10,20]	9.8
(20,Inf]	10.1

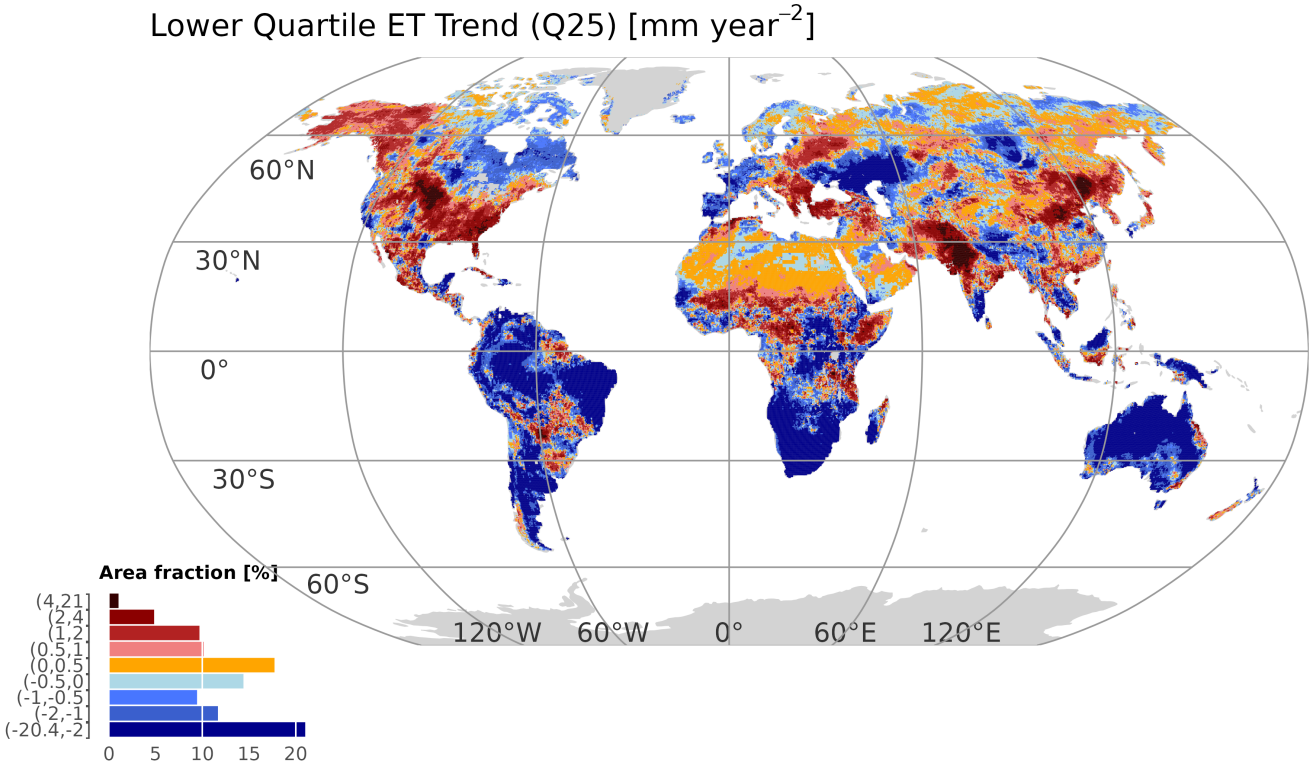

Figure S5. Maps of lower quartile $Q25$ annual evapotranspiration trend estimate of ensemble members.

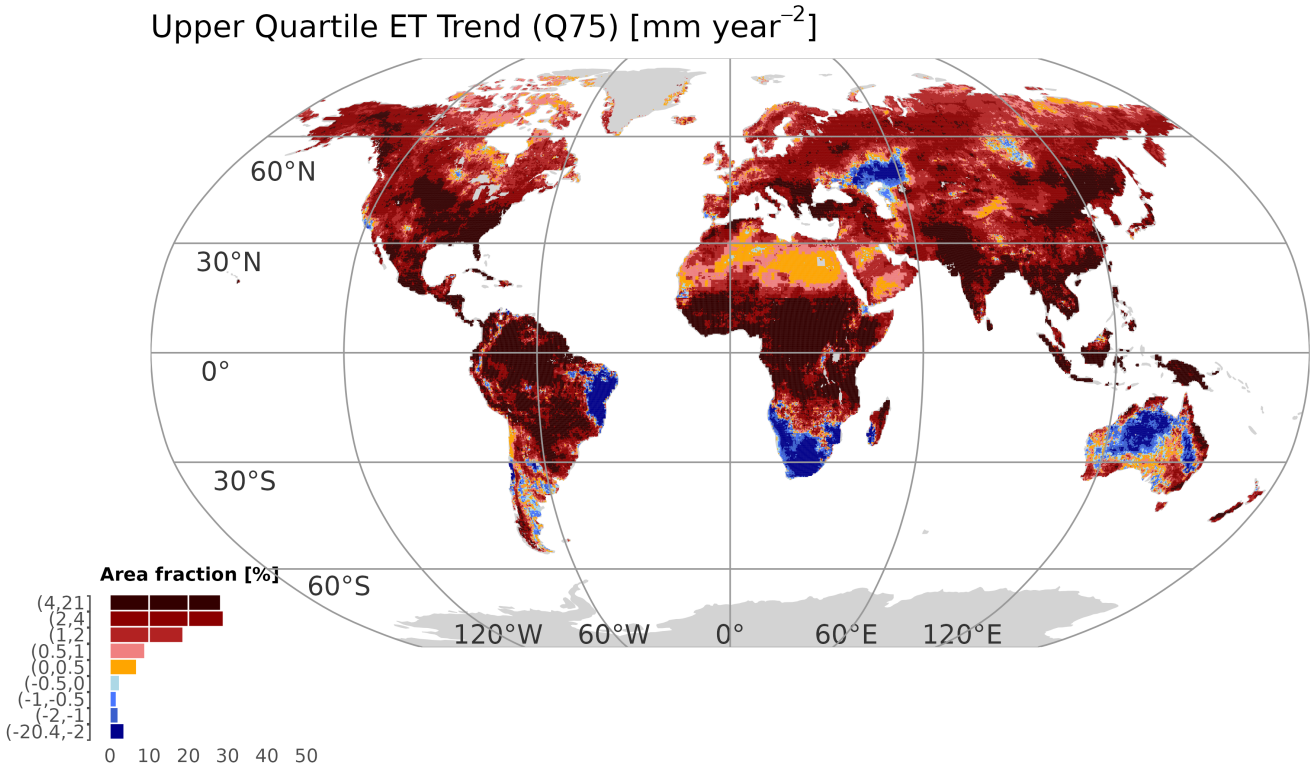

Figure S6. Maps of upper quartile $Q75$ annual evapotranspiration trend estimate of ensemble members.

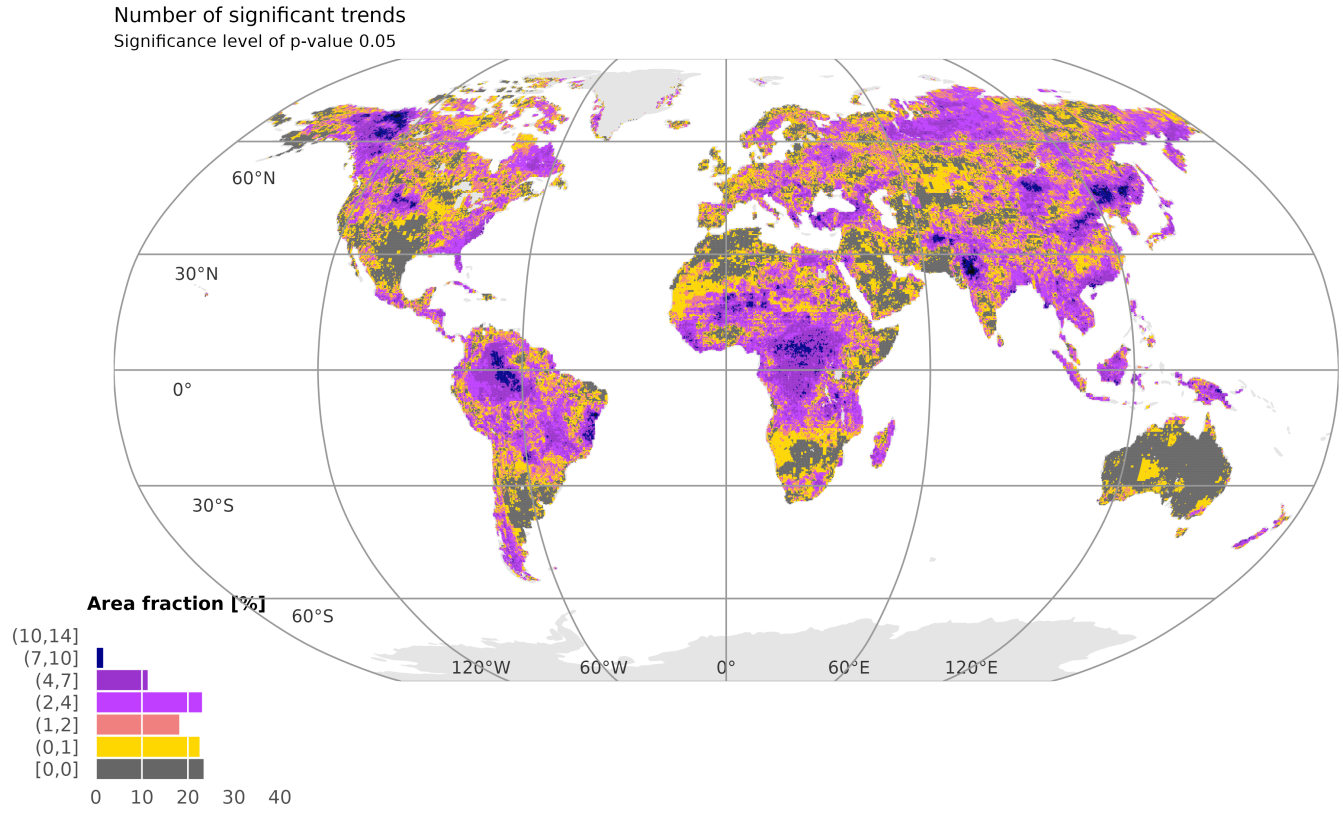

Figure S7. Maps of number of significant trends at p-value 0.05.

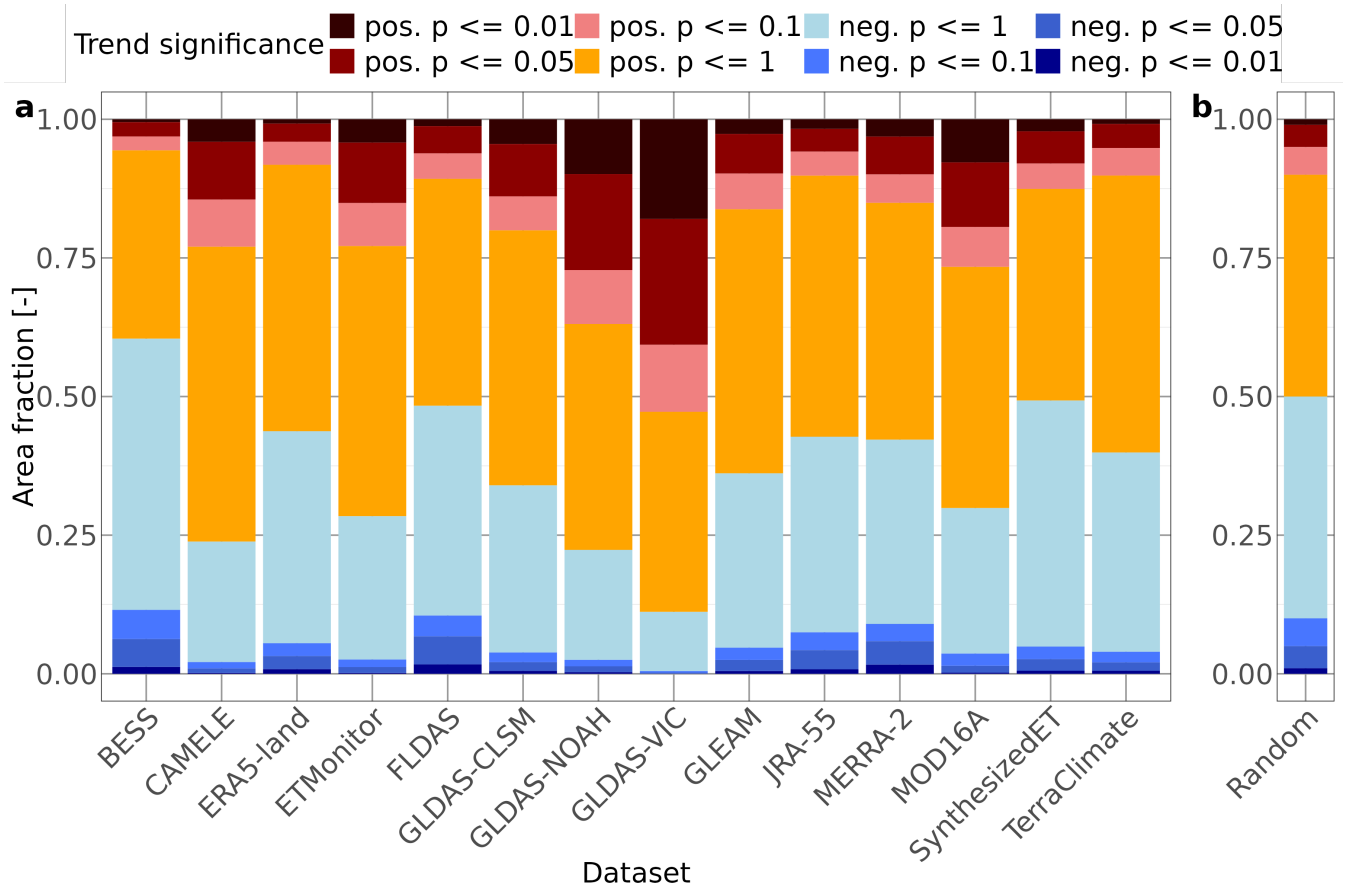

Figure S8. Area fraction of trend direction and trend significance for BESS v2 (Li et al., 2023), CAMELE (Li et al., 2024), ERA5-Land (Muñoz-Sabater et al., 2021), ETMonitor (Zheng et al., 2022), FLDAS (McNally et al., 2017), GLDAS-CLSM v2.1 (Li et al., 2020), GLDAS-NOAH v2.1 (Beaudoing and Rodell, 2020), GLDAS-VIC v2.1 (Beaudoing et al., 2020), GLEAM v4.1a (Miralles et al., 2025), JRA-55 (Kobayashi et al., 2015), MERRA-2 (Gelaro et al., 2017), MOD16A2 (Mu et al., 2011), SynthesizedET (Elnashar et al., 2021), TerraClimate (Abatzoglou et al., 2018) and, for comparison, our theoretical expectation if all trends were random.

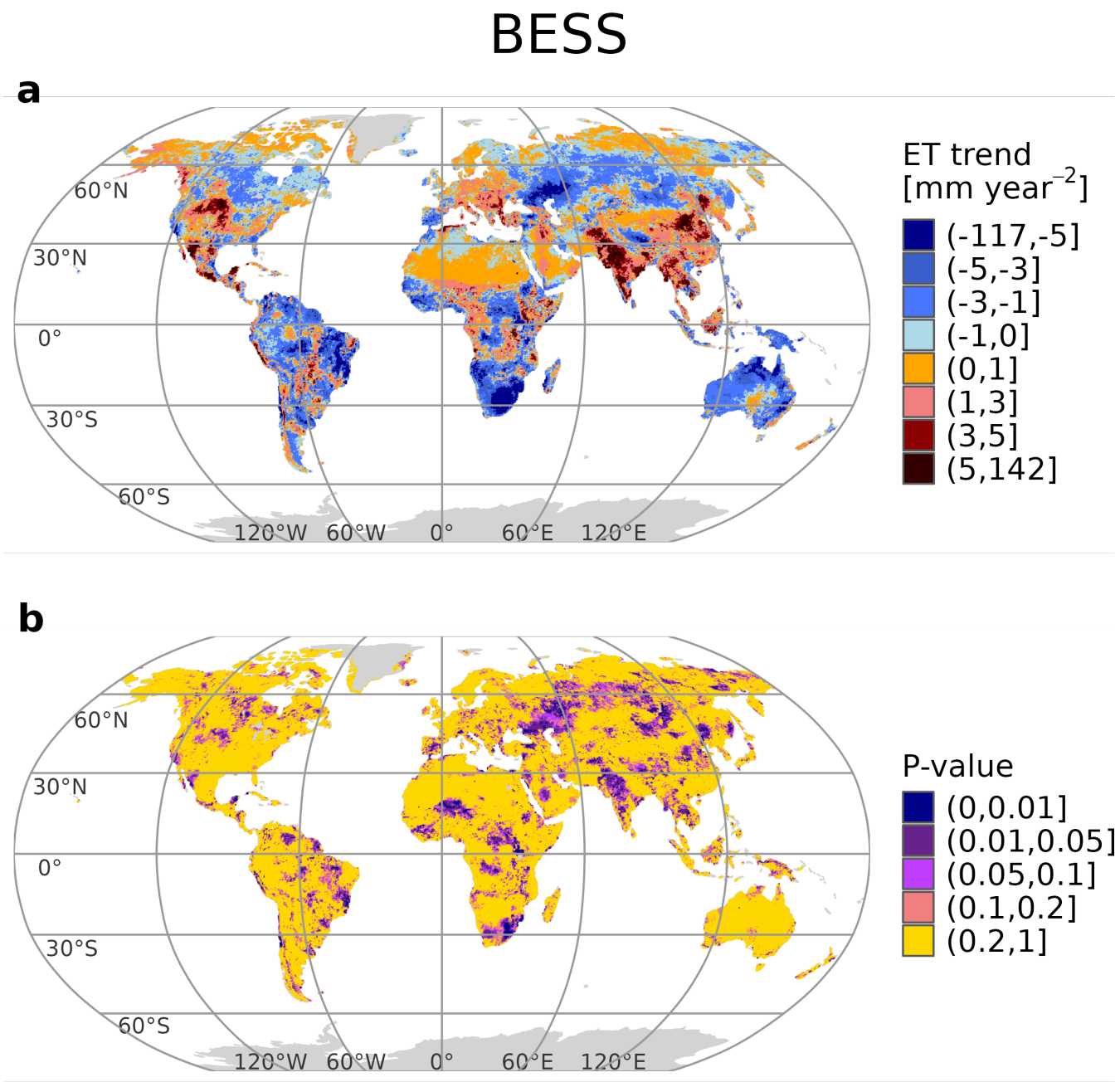

Figure S9. Maps of (a) trend estimates and (b) p-value for ET product BESS v2 (Li et al., 2023).

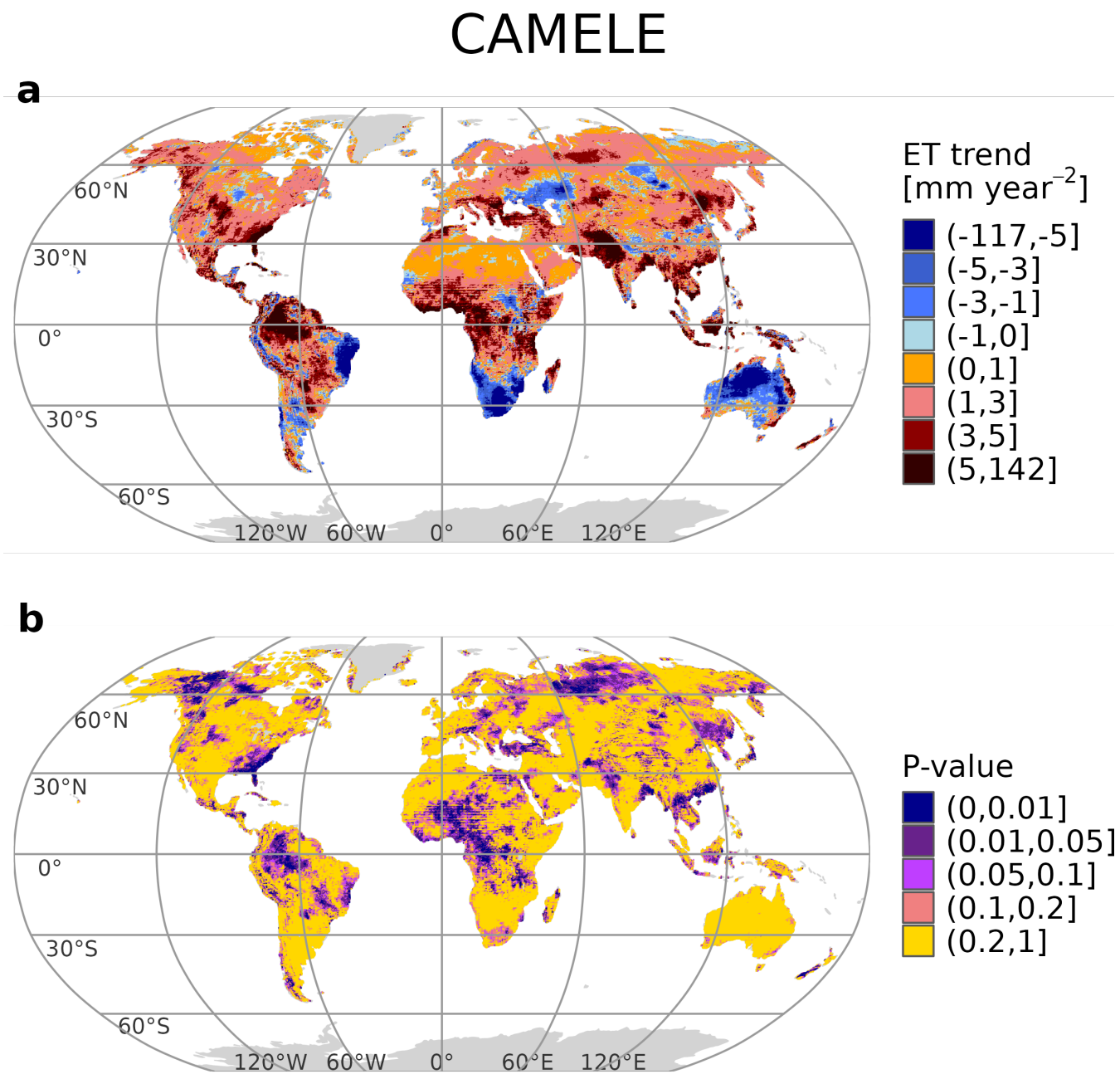

Figure S10. Maps of (a) trend estimates and (b) p-value for ET product CAMELE (Li et al., 2024).

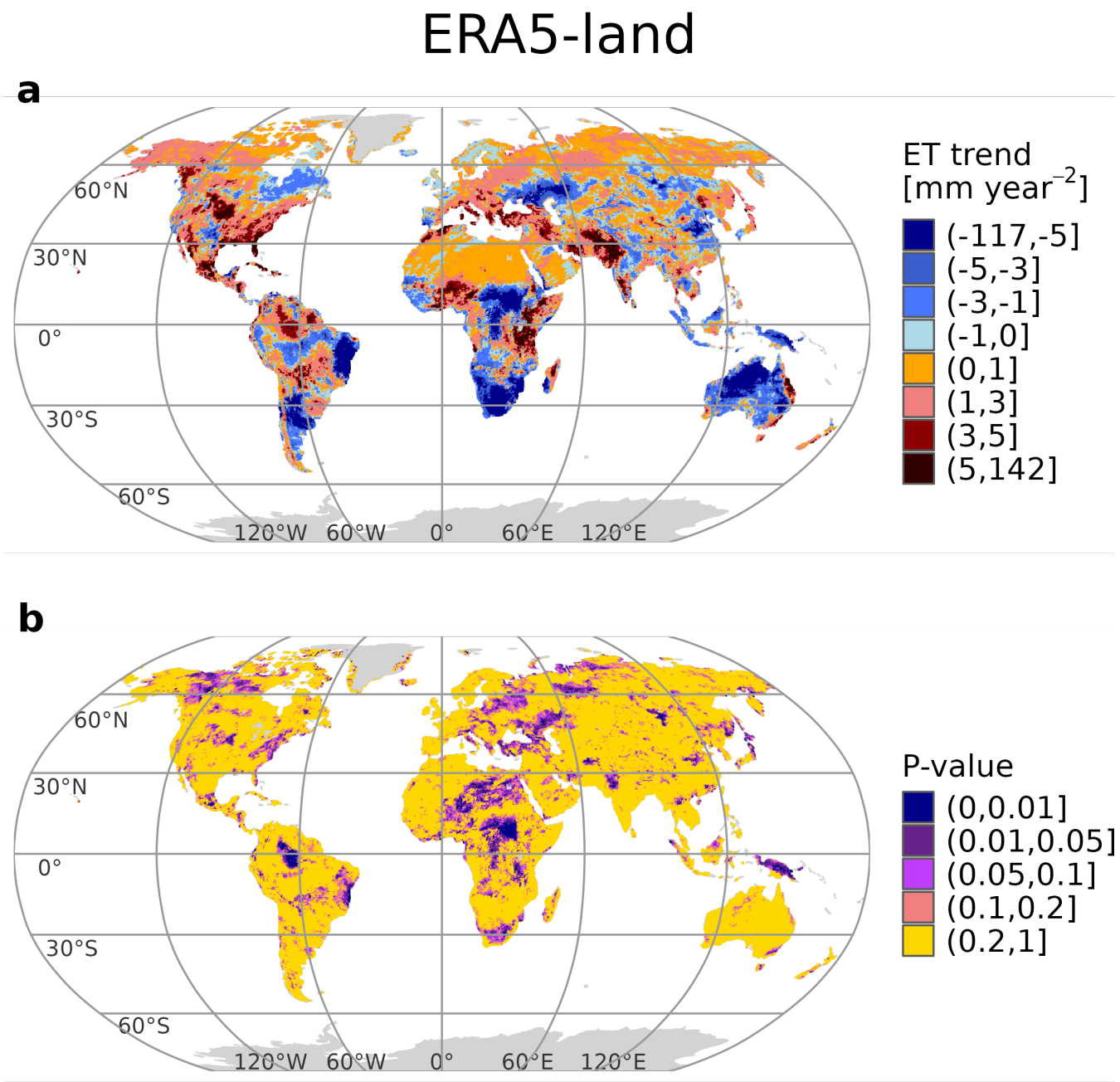

Figure S11. Maps of (a) trend estimates and (b) p-value for ET product ERA5-Land (Muñoz-Sabater et al., 2021).

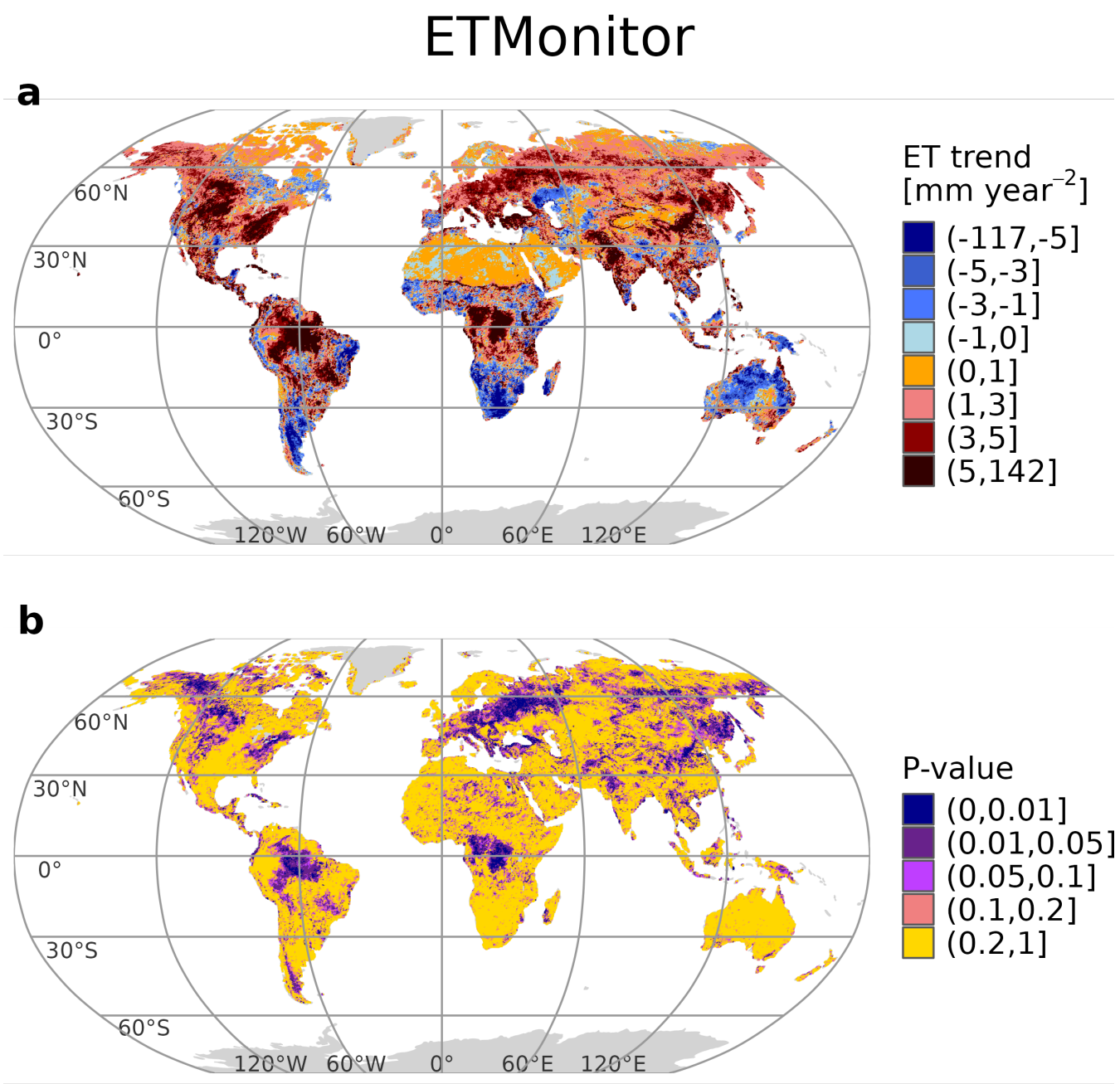

Figure S12. Maps of (a) trend estimates and (b) p-value for ET product ETMonitor (Zheng et al., 2022).

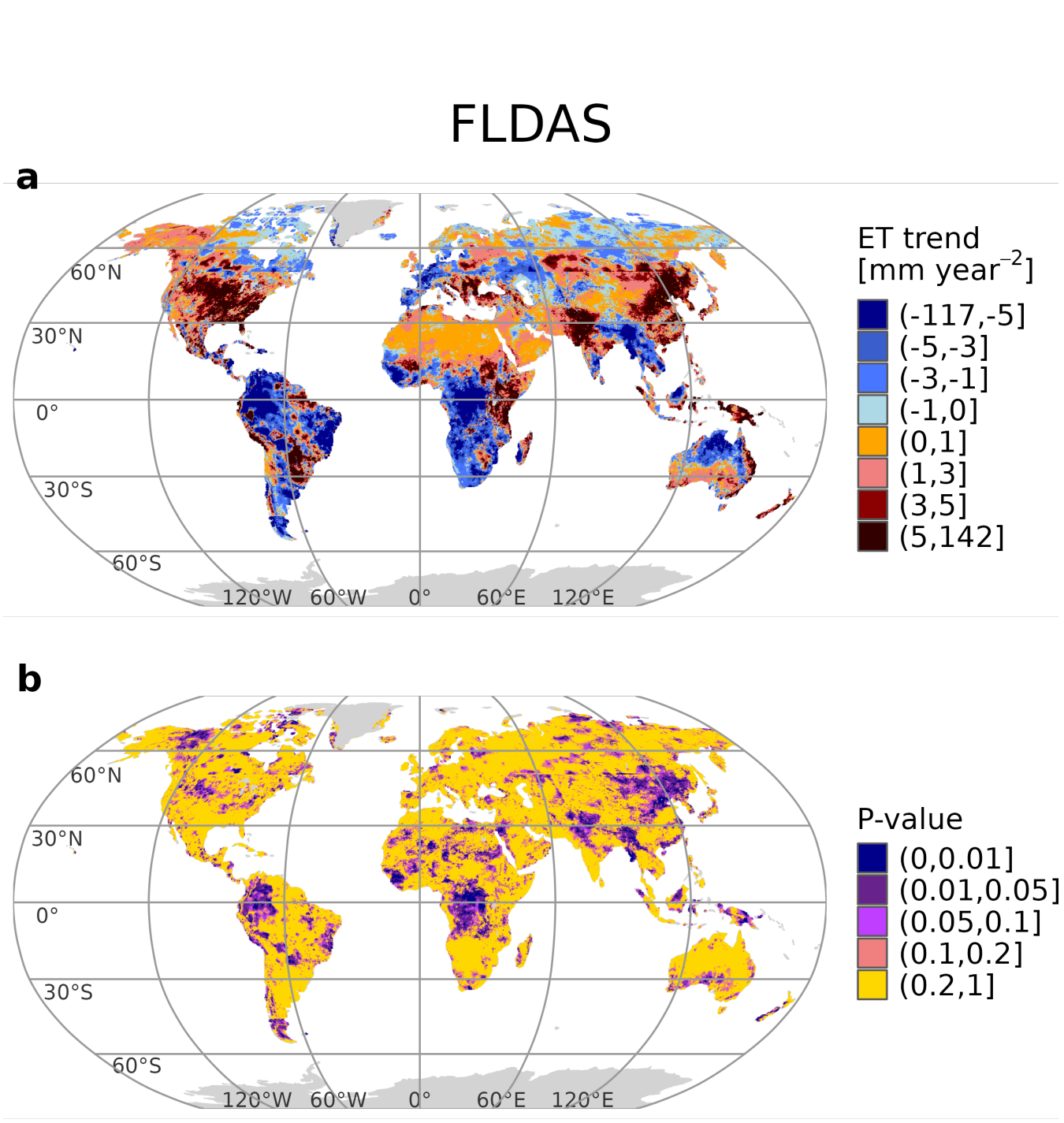

Figure S13. Maps of (a) trend estimates and (b) p-value for ET product FLDAS (McNally et al., 2017).

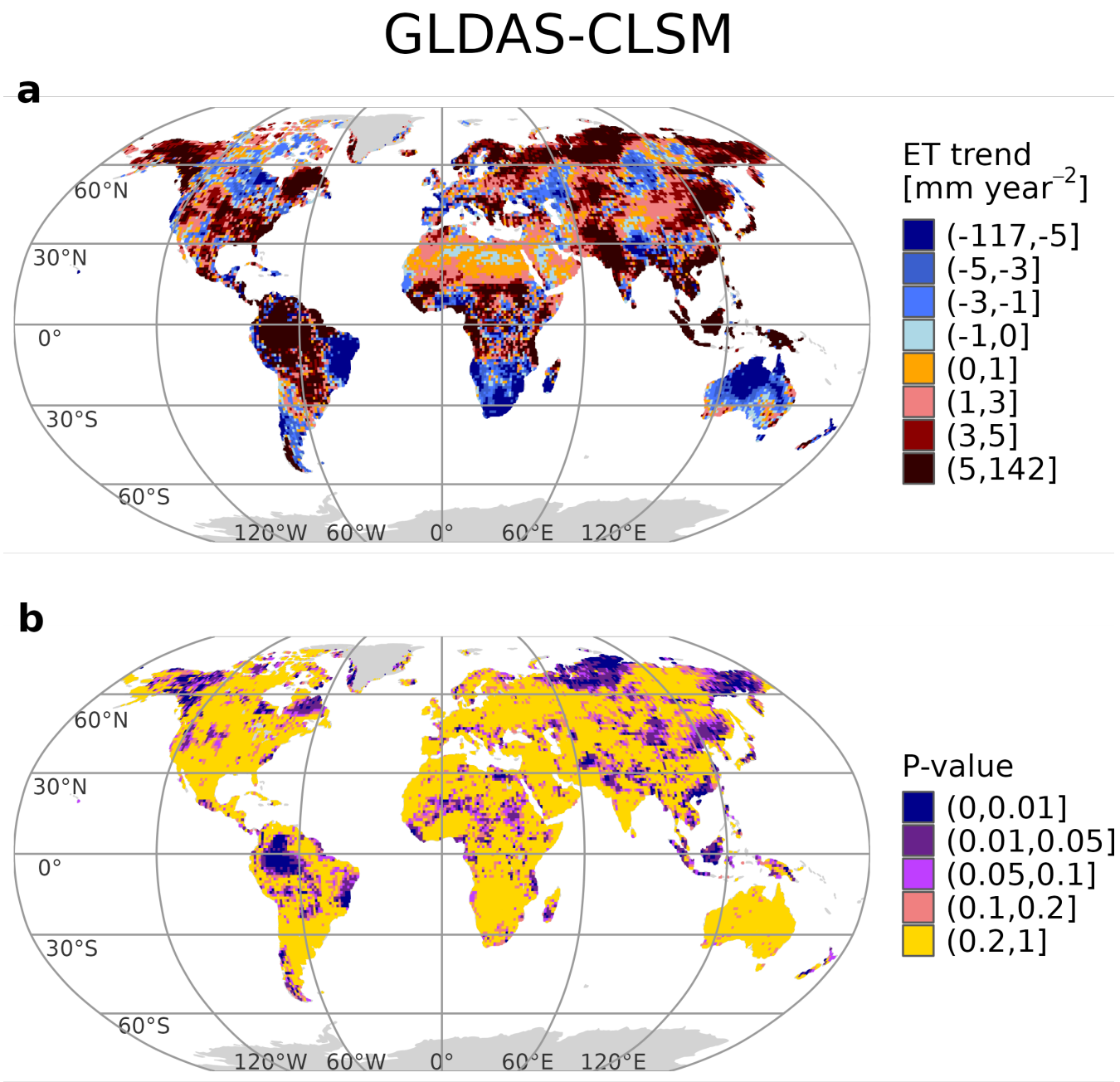

Figure S14. Maps of (a) trend estimates and (b) p-value for ET product GLDAS-CLSM v2.1 (Li et al., 2020).

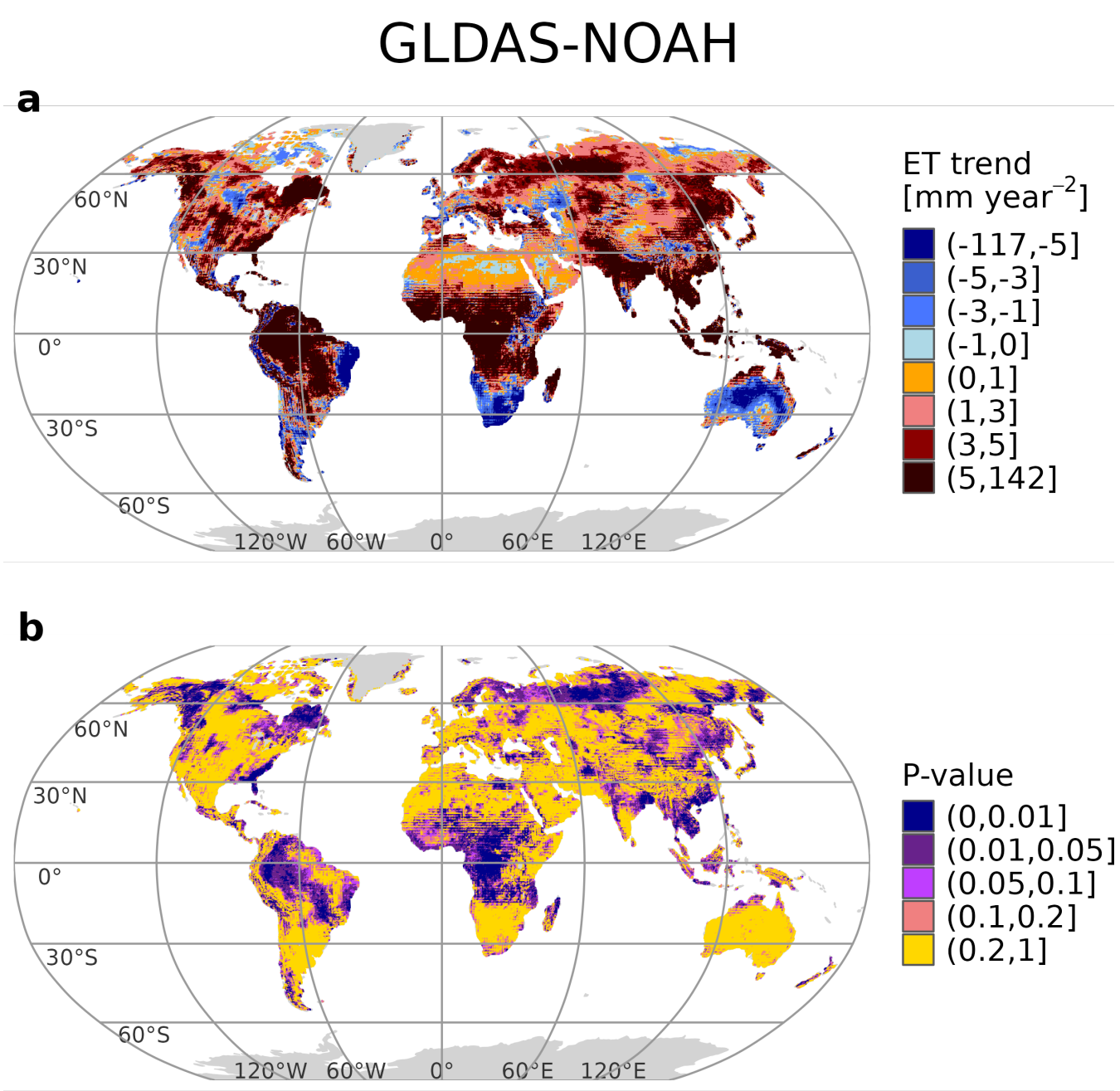

Figure S15. Maps of (a) trend estimates and (b) p-value for ET product GLDAS-NOAH v2.1 (Beaudoing and Rodell, 2020).

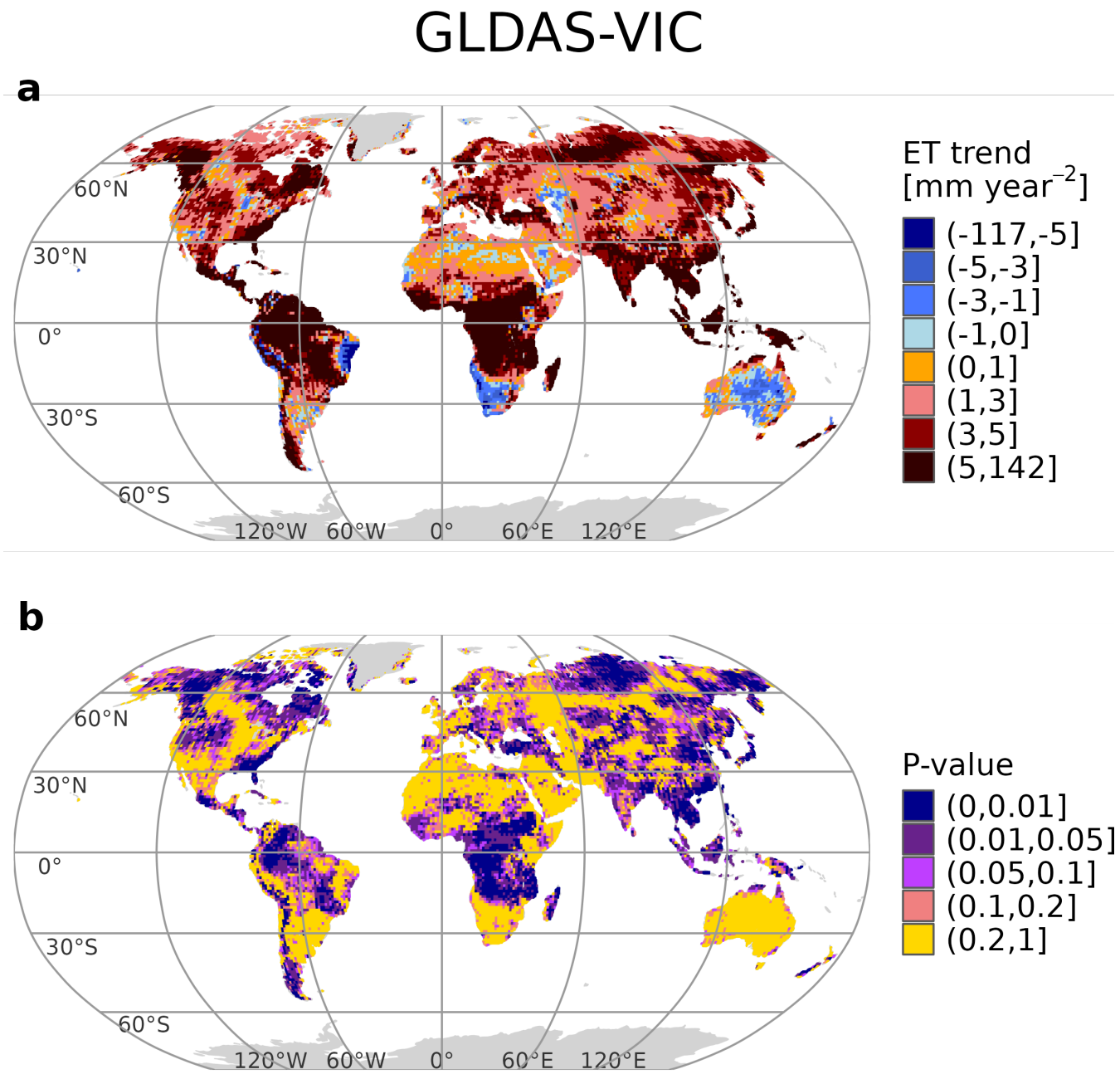

Figure S16. Maps of (a) trend estimates and (b) p-value for ET product GLDAS-VIC v2.1 (Beaudoing et al., 2020).

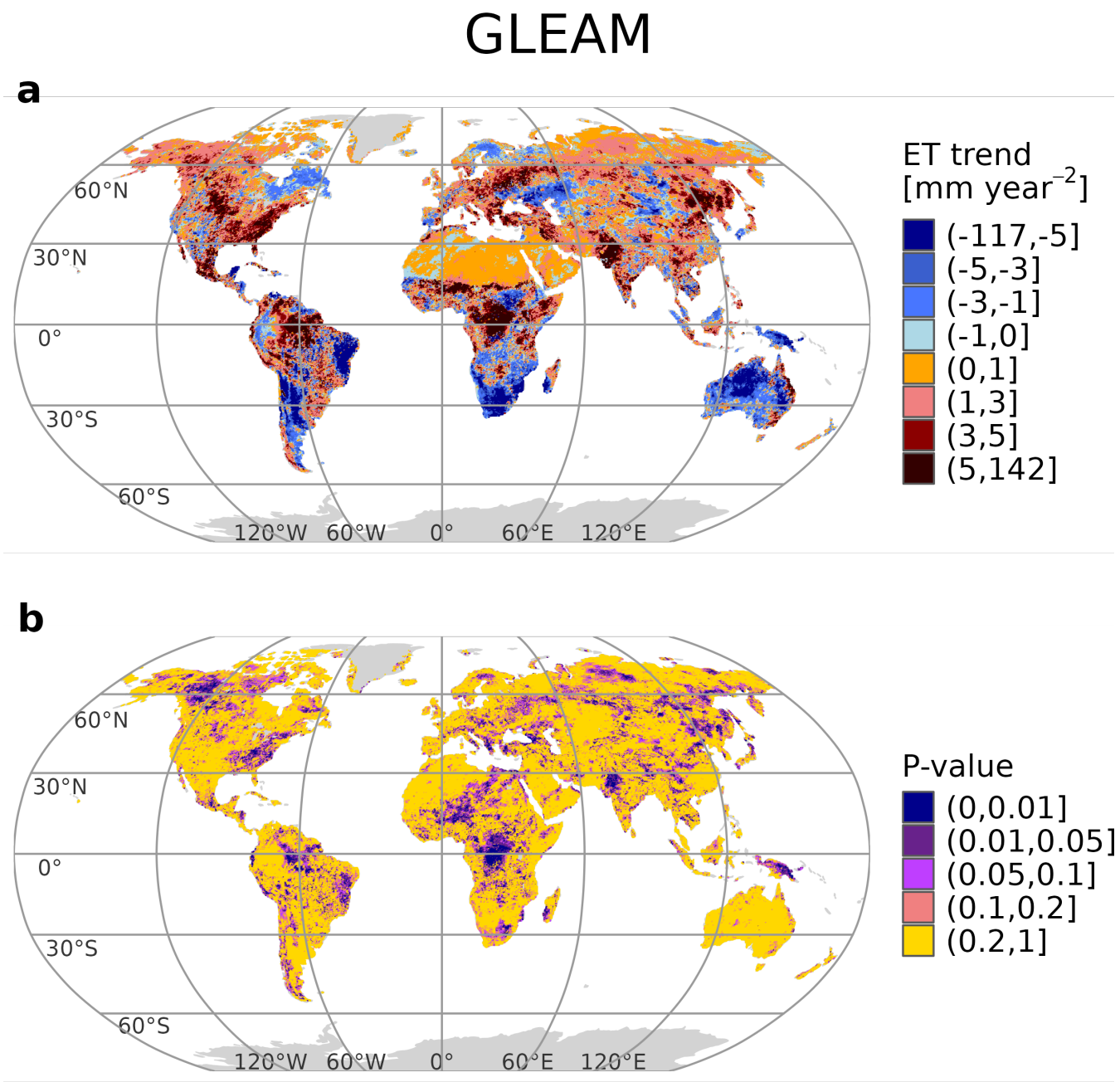

Figure S17. Maps of (a) trend estimates and (b) p-value for ET product GLEAM v4.1a (Miralles et al., 2025).

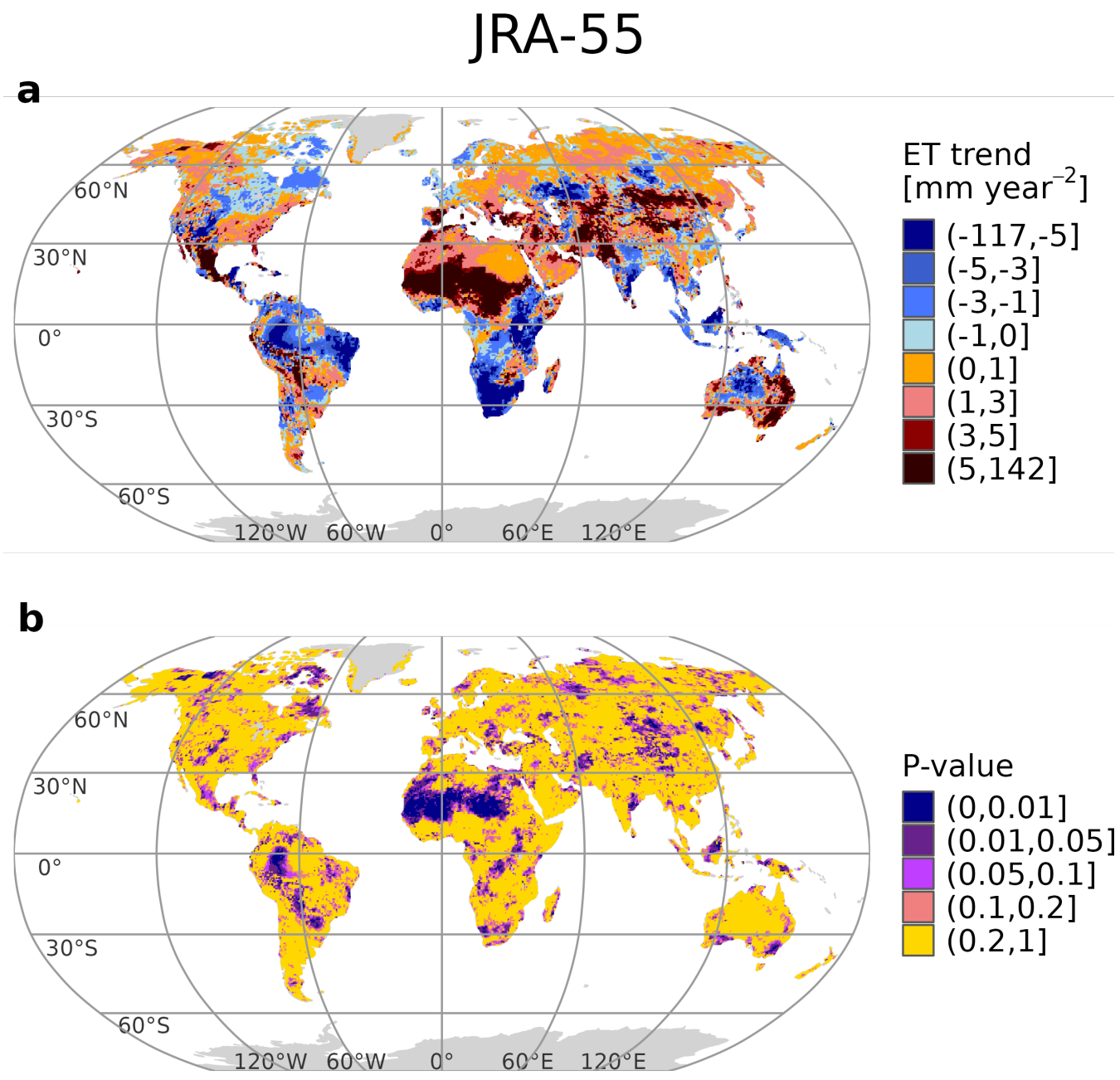

Figure S18. Maps of (a) trend estimates and (b) p-value for ET product JRA-55 (Kobayashi et al., 2015).

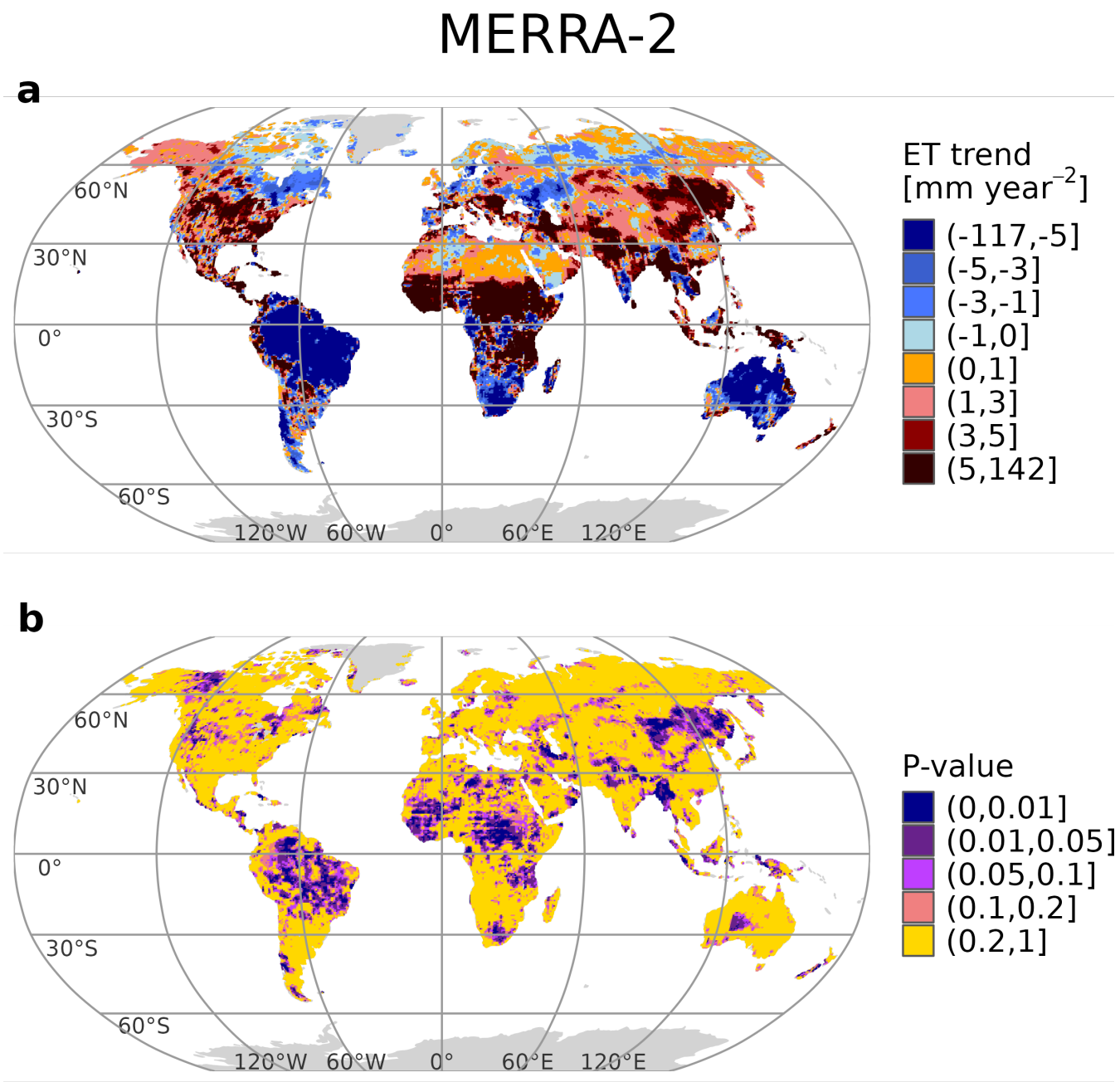

Figure S19. Maps of (a) trend estimates and (b) p-value for ET product MERRA-2 (Gelaro et al., 2017).

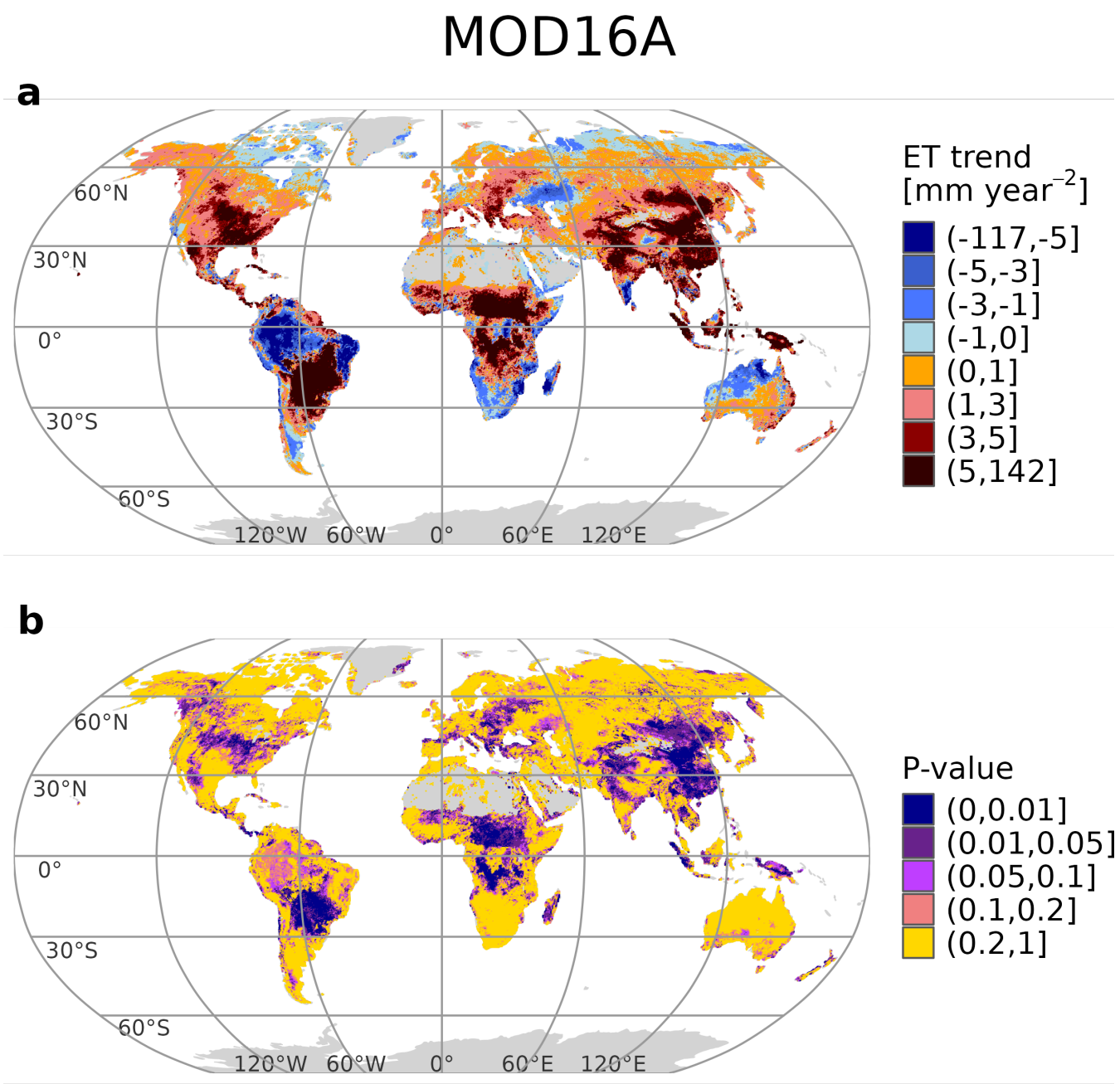

Figure S20. Maps of (a) trend estimates and (b) p-value for ET product MOD16A2 (Mu et al., 2011).

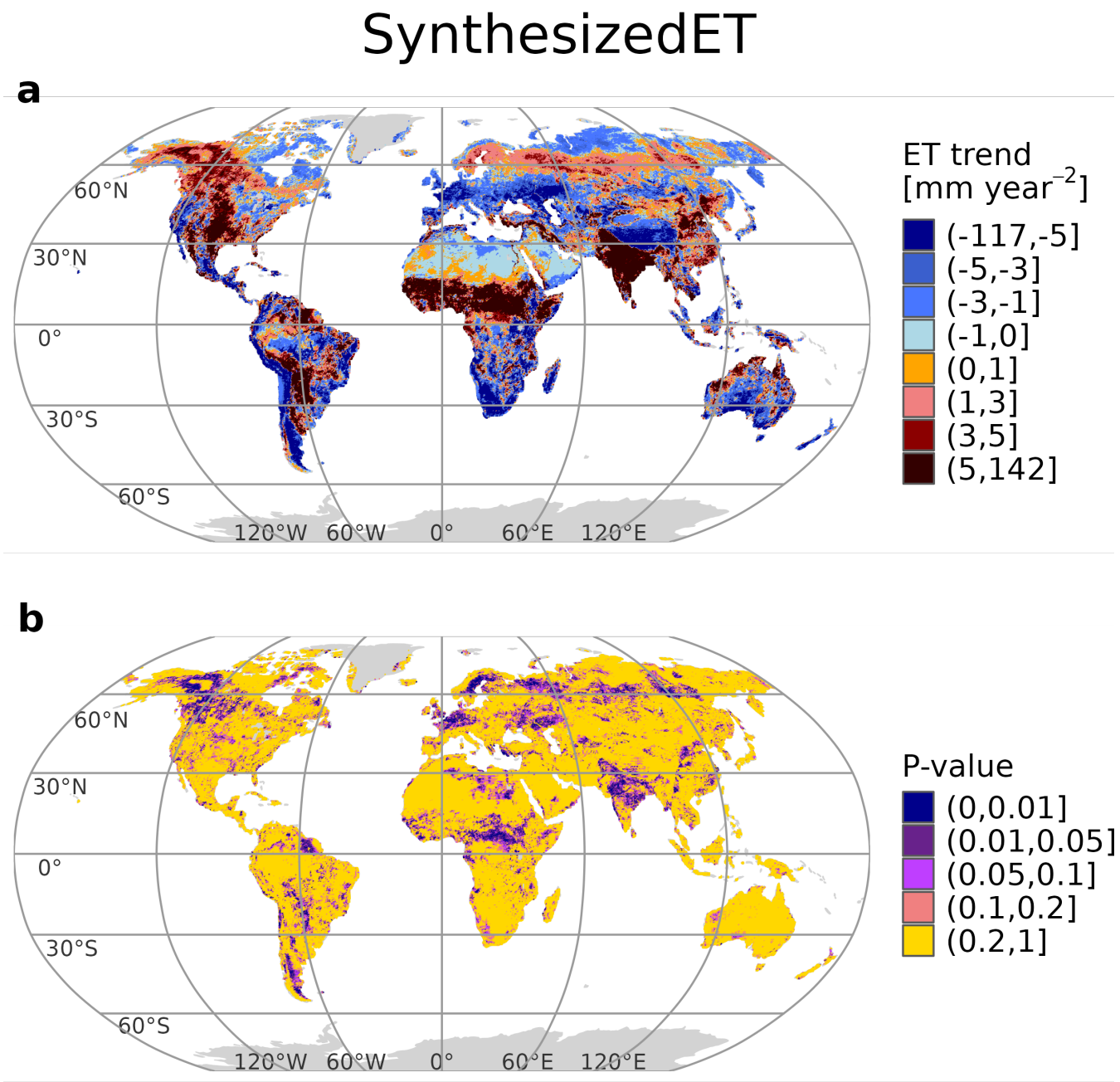

Figure S21. Maps of (a) trend estimates and (b) p-value for ET product SynthesizedET (Elnashar et al., 2021).

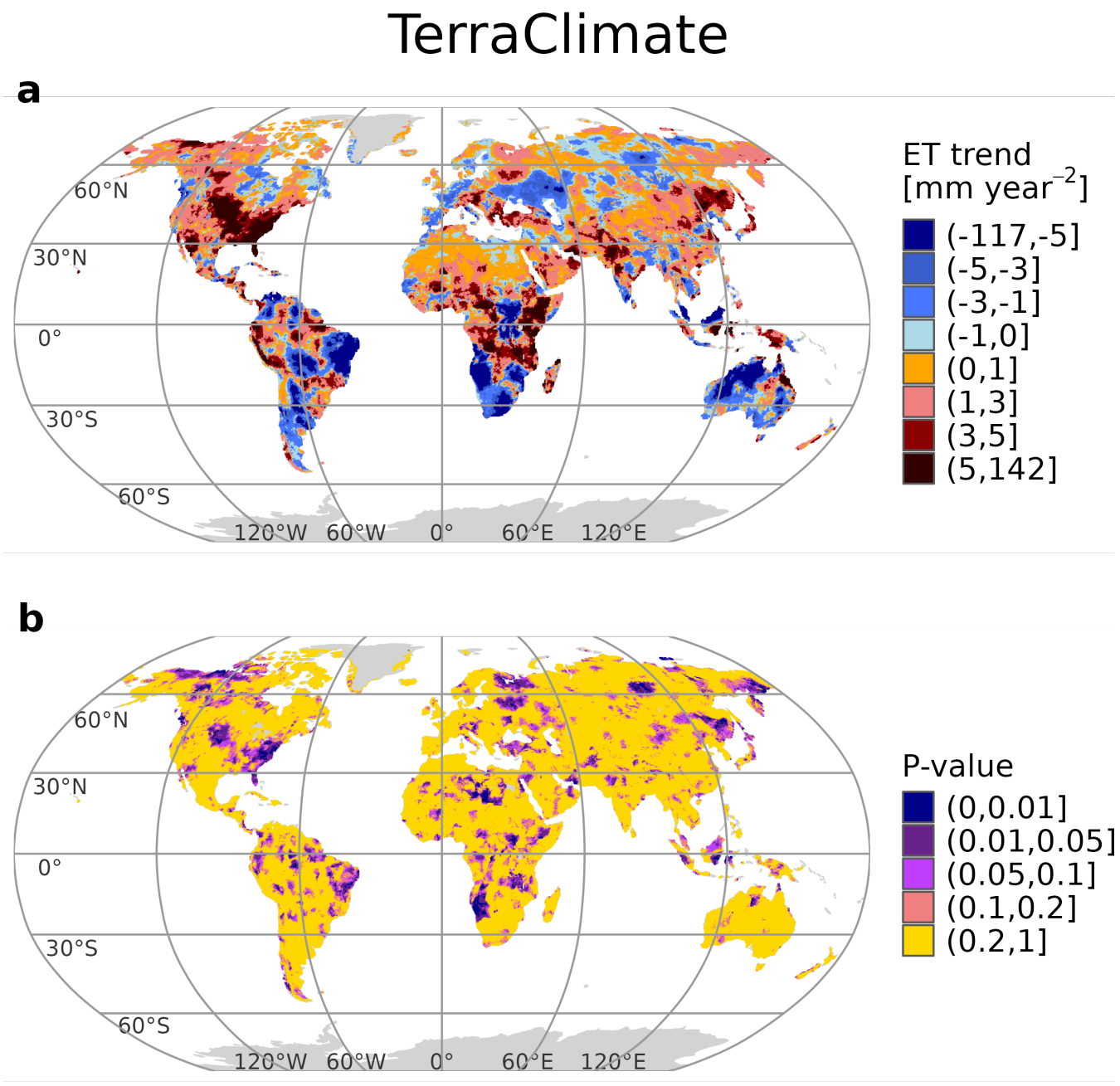

Figure S22. Maps of (a) trend estimates and (b) p-value for ET product TerraClimate (Abatzoglou et al., 2018).

3.2 Pair-wise dataset comparison

For each pair of data products (dataset A and dataset B), we calculated:

- a: number of grid cells where only dataset A produced significant trends in a given direction,
- b: number of grid cells where only dataset B produced significant trends in a given direction,
- c: number of grid cells where both datasets produced significant trends with the same direction.

If dataset A produced a positive significant trend and dataset B a negative significant trend, this was not counted as c but contributed to a and b. Consequently, the sum of a, b, and c can exceed the number of grid cells with significant trends.

The critical success index (CSI), adapted from Kim et al. (2021), was calculated as:

$$CSI = \frac{c}{a+b+c} \times 100. \tag{S1}$$

where CSI represents the percentage of significant trends occurring in common. CSI equals 100 % when all significant trends occur jointly and 0 % when none do. CSI can be low because of lack of overlap of significant trends, different trend direction or because of an imbalance or bias in the number of significant trends between ET products.

We calculate the bias adapted from Kim et al. (2021) as

$$bias = \frac{a+c}{b+c}, \tag{S2}$$

where bias is 1 (no bias) if dataset A and dataset B produce the same number of significant trends. If dataset B produces no significant trends, the index is undefined due to division by zero.

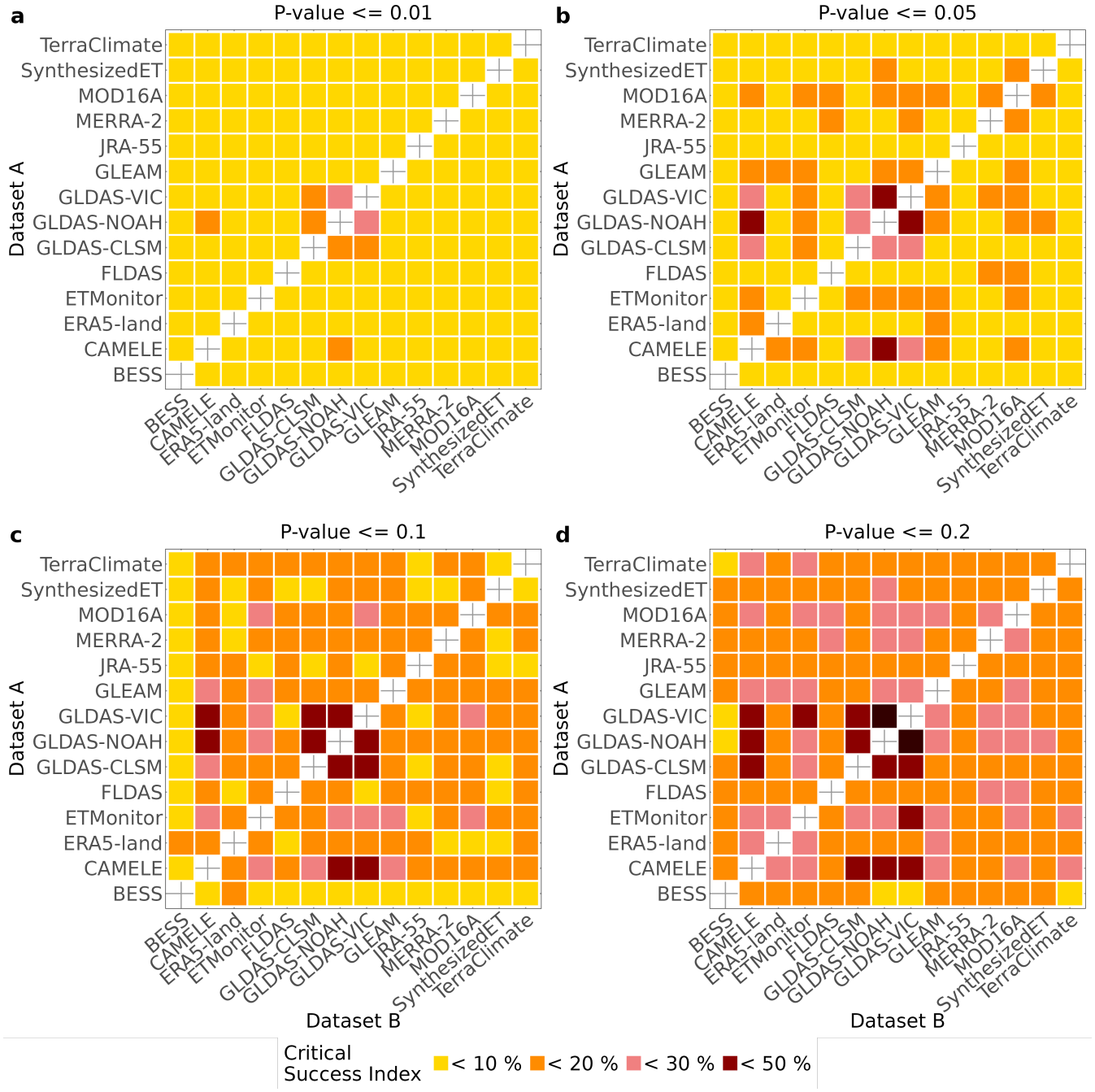

Figure S23. Pair-wise comparison of ET data products using the critical success index (Kim et al., 2021) for p-value thresholds 0.01, 0.05, 0.1, and 0.2.

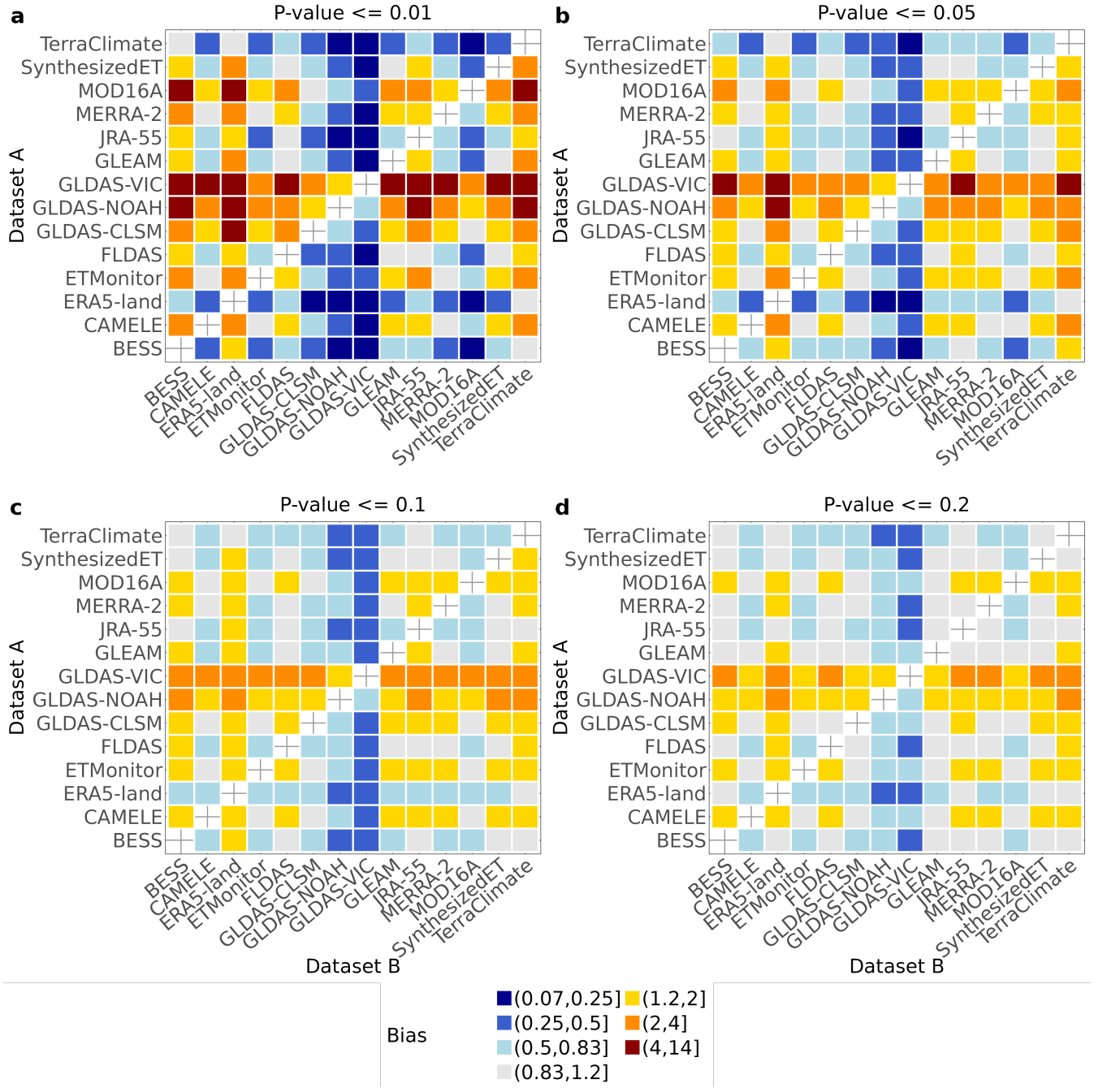

Figure S24. Pair-wise comparison of ET data products using the BIAS index (ratio of significant trends) (Kim et al., 2021) for p-value thresholds 0.01, 0.05, 0.1, and 0.2.

3.3 Quartile uncertainty

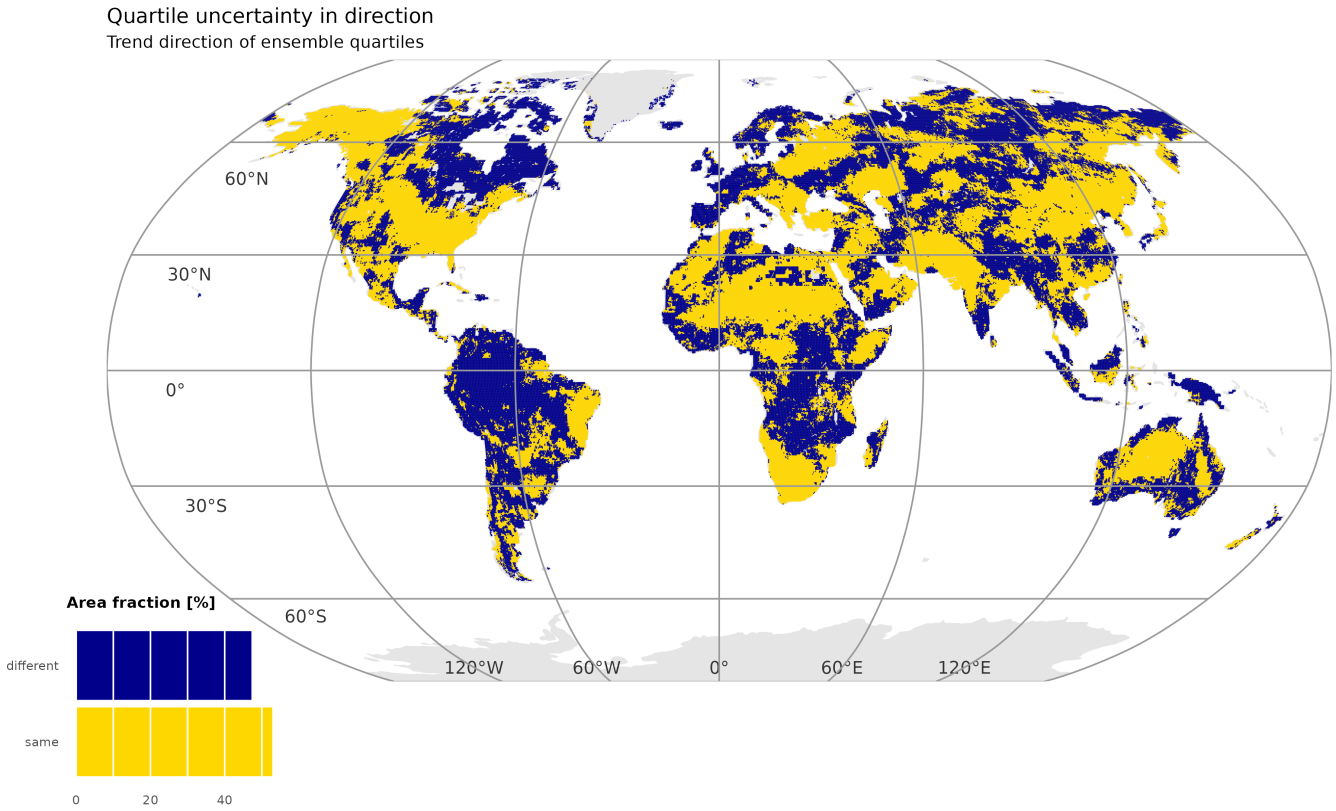

Figure S25. Map of quartile uncertainty in direction.

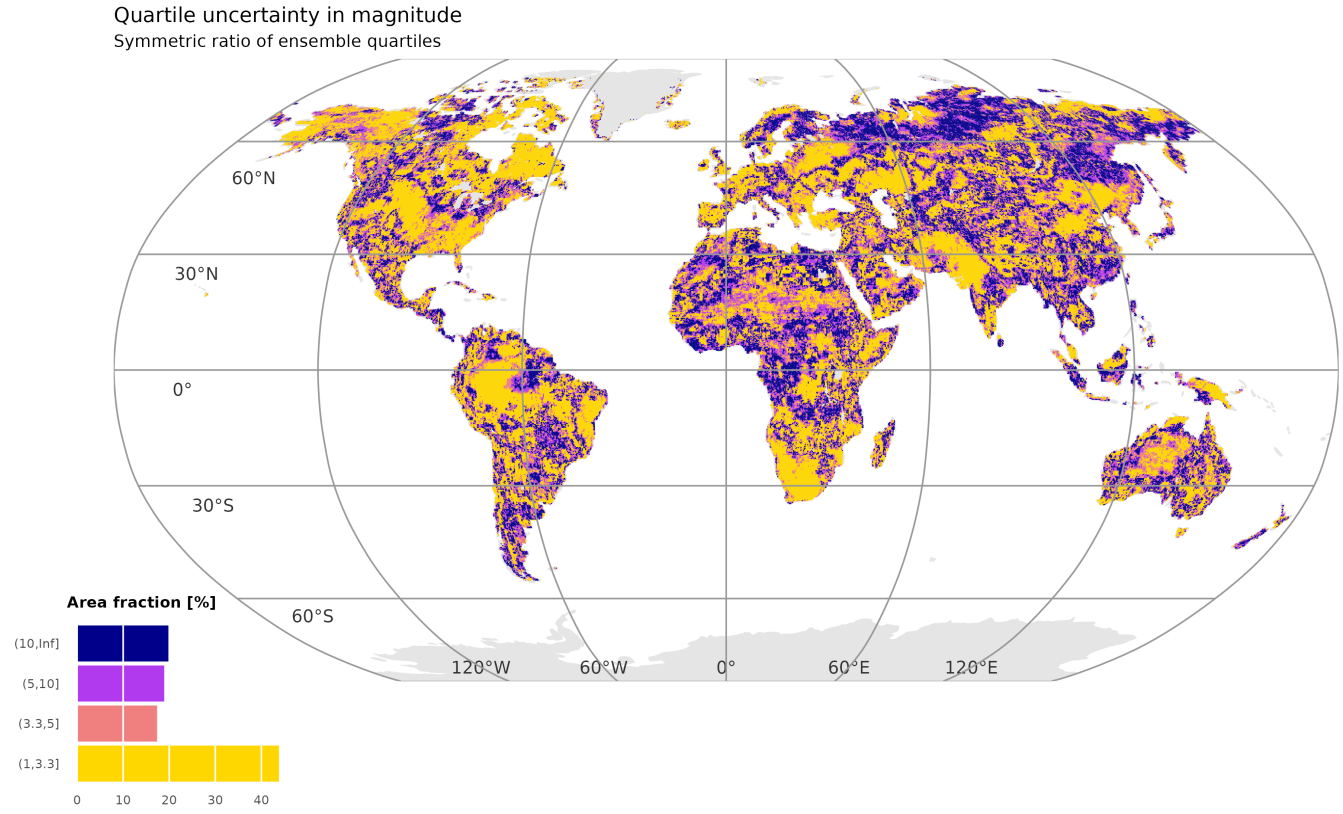

Figure S26. Map of quartile uncertainty in magnitude.

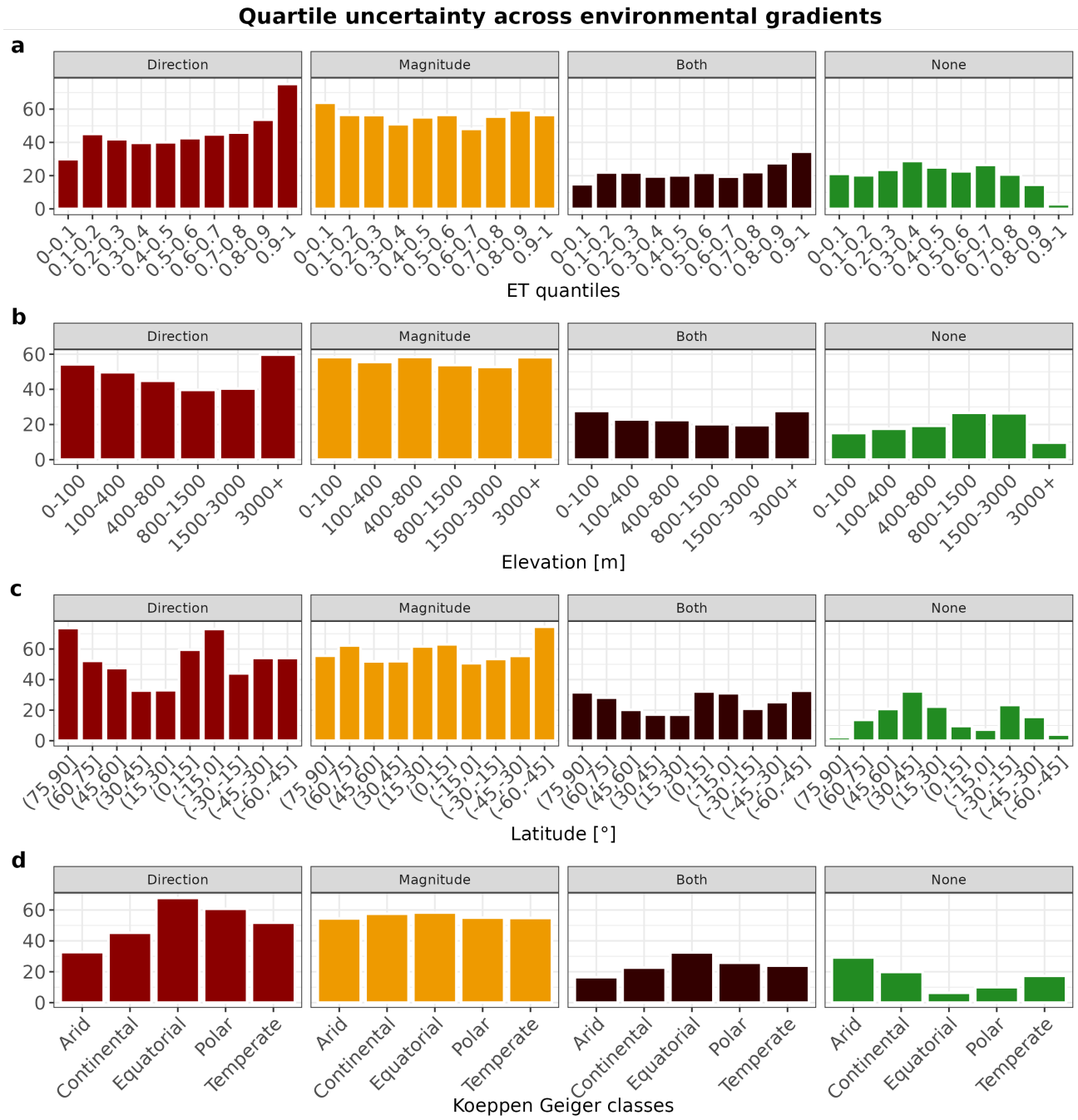

Figure S27. Evapotranspiration trend estimates and area fraction of quartile uncertainty for elevation classes, evaporation quantiles, latitude, and main Köppen–Geiger climate classes.

3.4 Topology

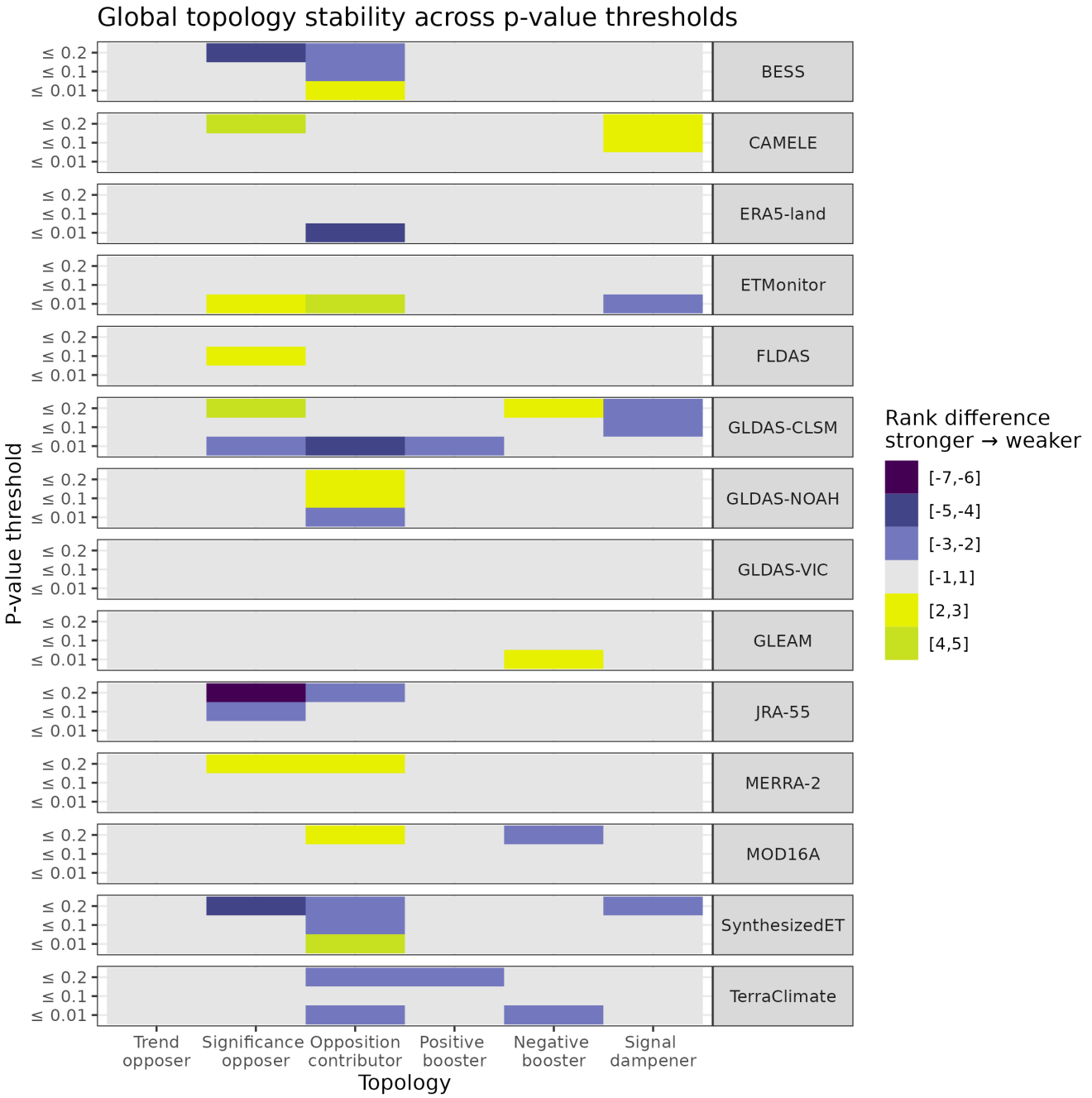

Figure S28. Stability of global topology rank across p-value thresholds for trend signatures. Shown are rank differences relative to the topology estimate at p-value 0.05.

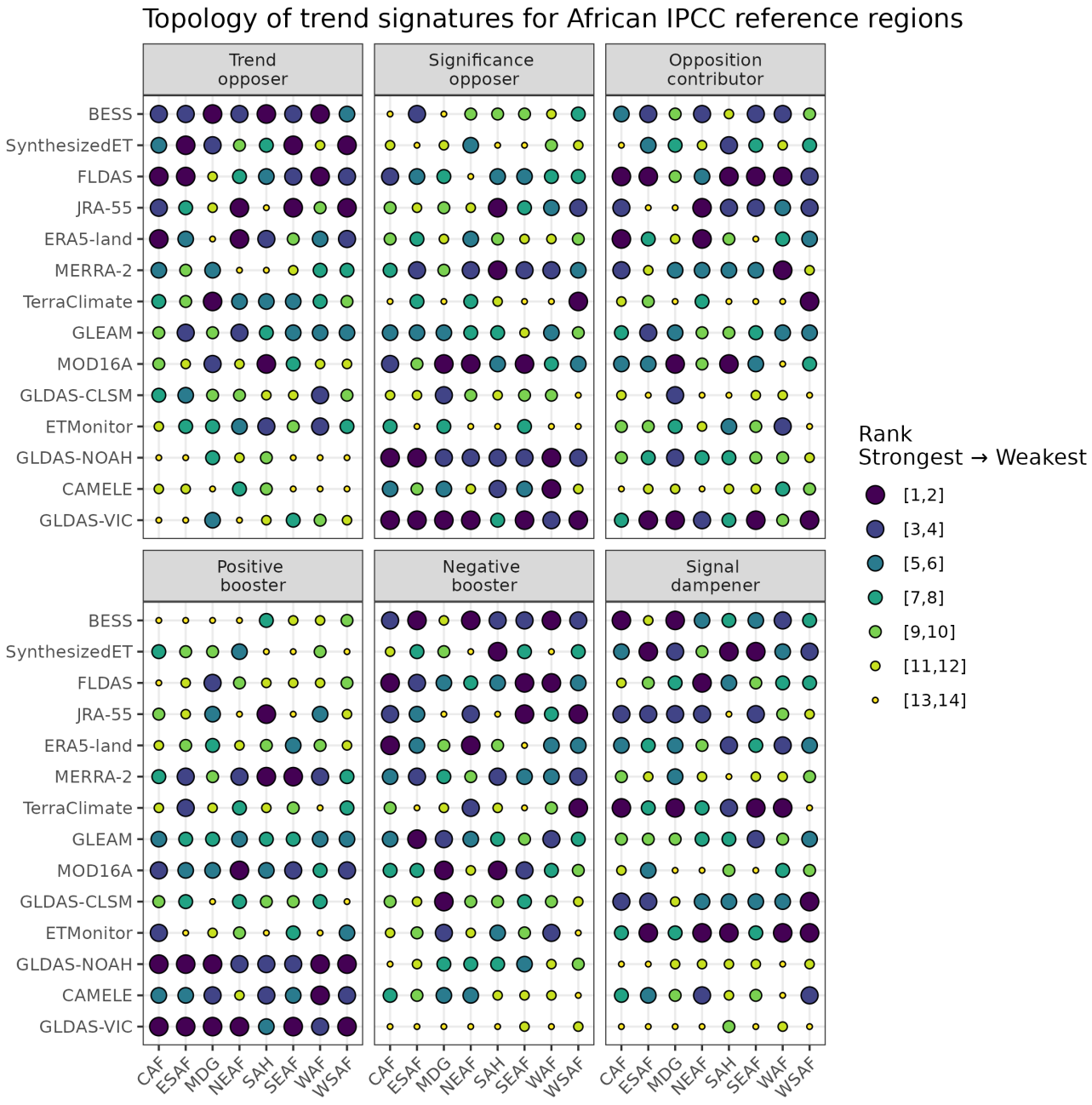

Figure S29. Topology across African IPCC reference regions. Darker and larger circles indicate stronger dataset roles.

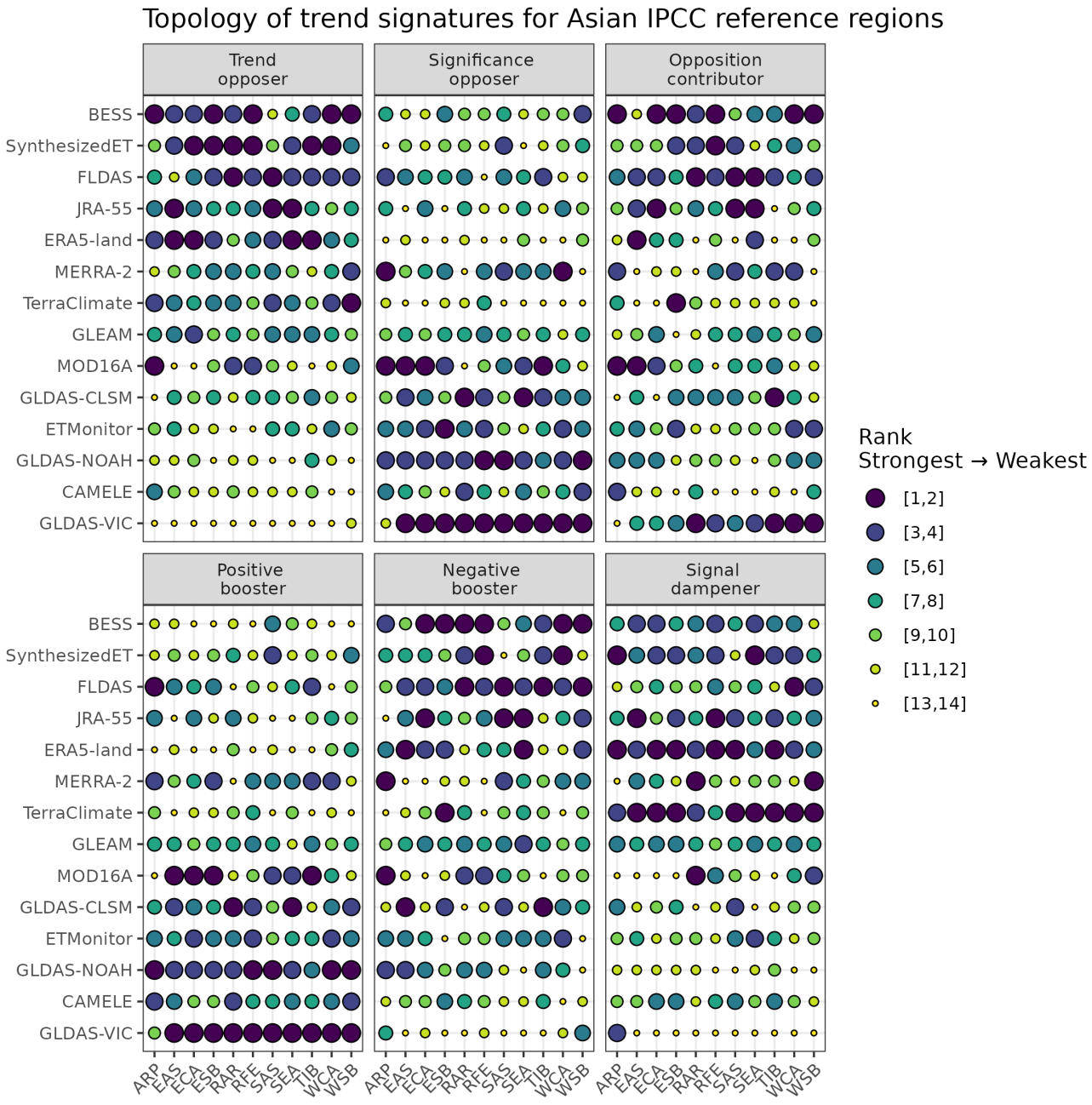

Figure S30. Topology across Asian IPCC reference regions. Darker and larger circles indicate stronger dataset roles.

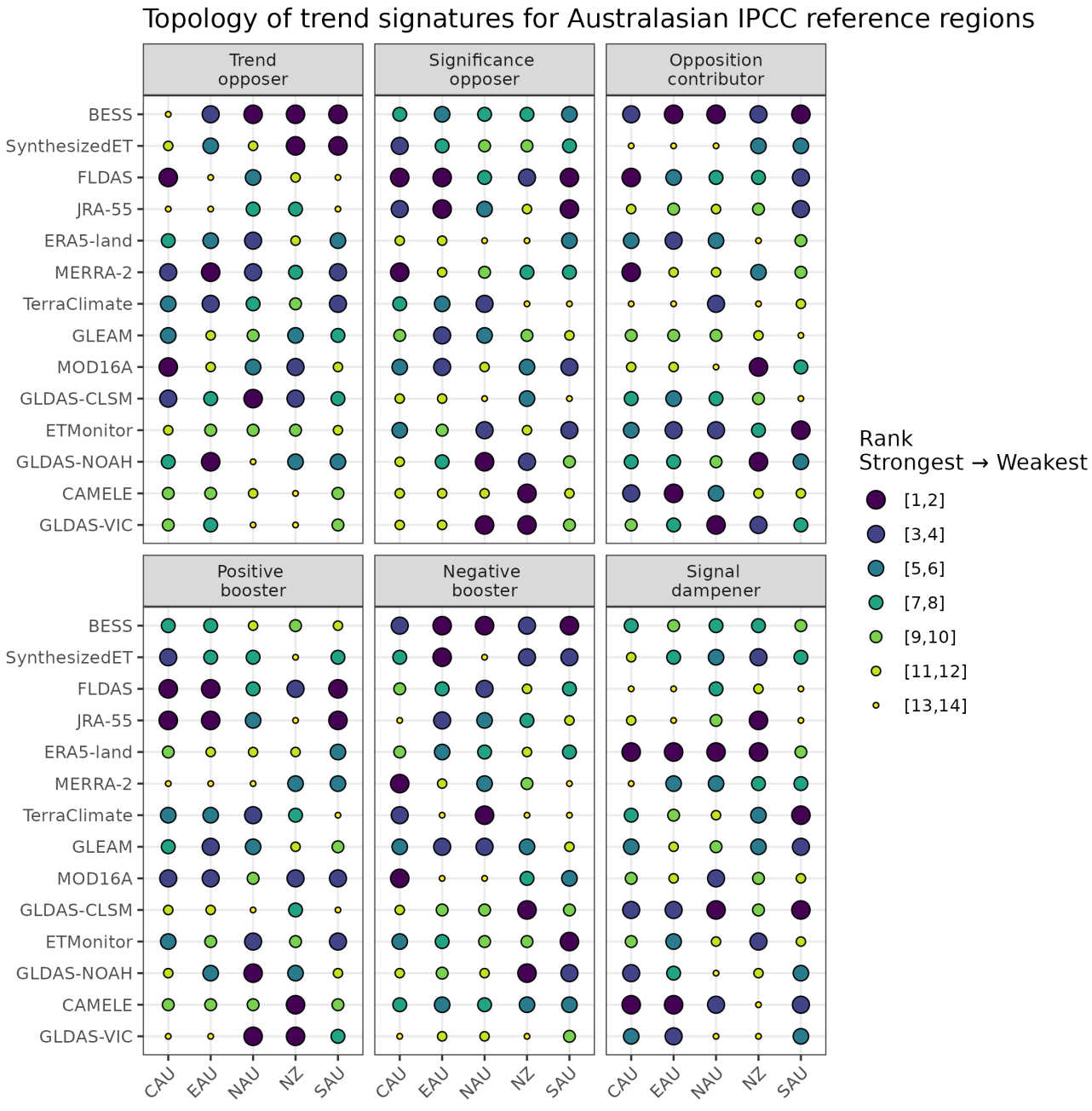

Figure S31. Topology across Australasian IPCC reference regions. Darker and larger circles indicate stronger dataset roles.

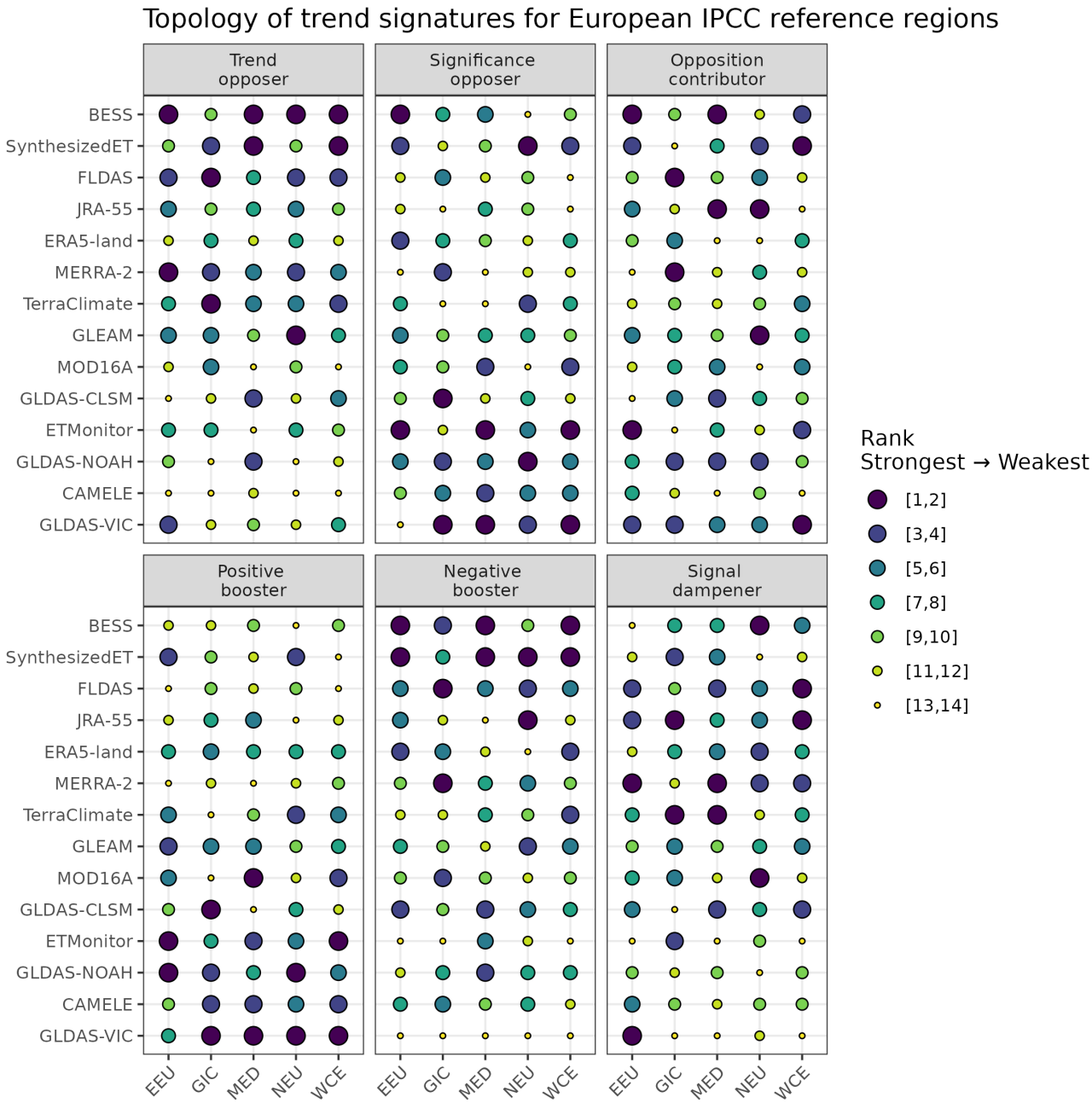

Figure S32. Topology across European IPCC reference regions. Darker and larger circles indicate stronger dataset roles.

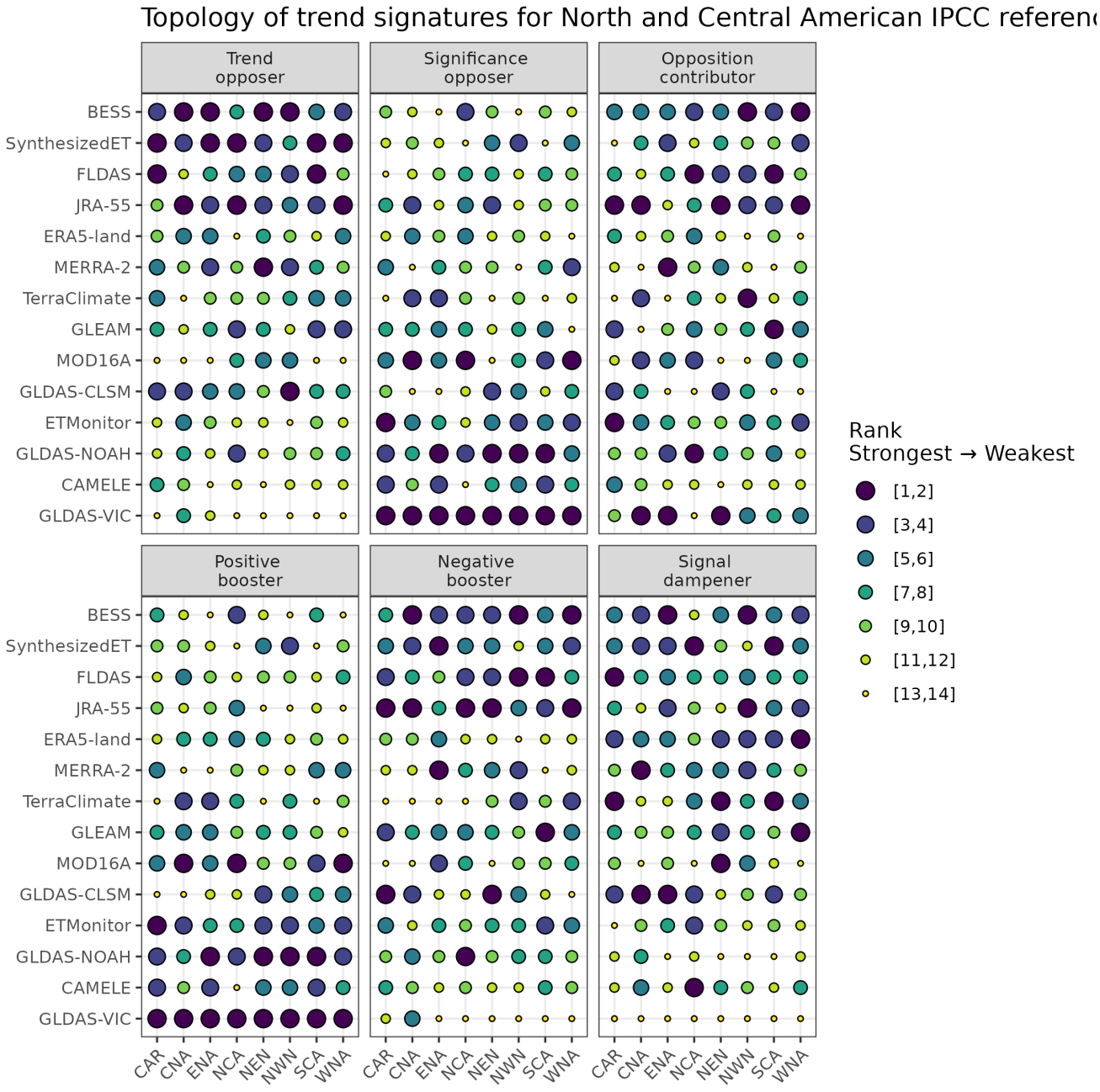

Figure S33. Topology across Northern and Central American IPCC reference regions. Darker and larger circles indicate stronger dataset roles.

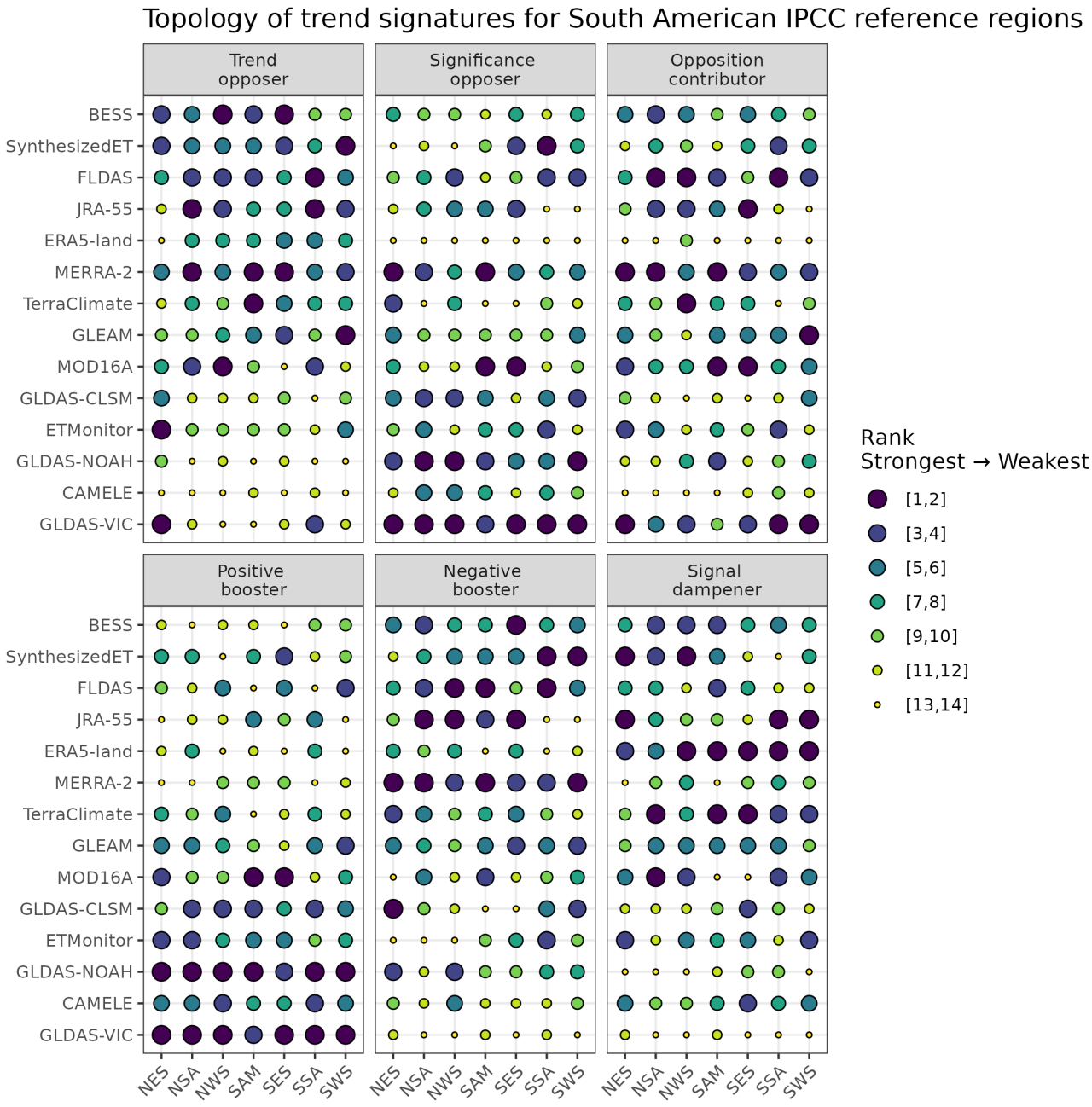

Figure S34. Topology across South American IPCC reference regions. Darker and larger circles indicate stronger dataset roles.

References

Abatzoglou, J. T., Dobrowski, S. Z., Parks, S. A., and Hegewisch, K. C.: TerraClimate, a high-resolution global dataset of monthly climate and climatic water balance from 1958–2015, Scientific Data, 5, 170 191, https://doi.org/10.1038/sdata.2017.191, number: 1 Publisher: Nature Publishing Group, 2018.

Adler, R. F., Huffman, G. J., Chang, A., Ferraro, R., Xie, P.-P., Janowiak, J., Rudolf, B., Schneider, U., Curtis, S., Bolvin, D., et al.: The version-2 global precipitation climatology project (GPCP) monthly precipitation analysis (1979–present), Journal of hydrometeorology, 4, 1147–1167, 2003.

Ball, J. T., Woodrow, I. E., and Berry, J. A.: A model predicting stomatal conductance and its contribution to the control of photosynthesis under different environmental conditions, in: Progress in photosynthesis research: volume 4 proceedings of the VIIth international congress on photosynthesis providence, Rhode Island, USA, august 10–15, 1986, pp. 221–224, Springer, 1987.

Beaudoing, H. and Rodell, M.: GLDAS Noah Land Surface Model L4 monthly 0.25 x 0.25 degree Early Product V2.1 (GLDAS_NOAH025_M_EP) at GES DISC, https://doi.org/https://doi.org/10.1175/BAMS-85-3-381, 2020.

Beaudoing, H., Rodell, M., and NASA/GSFC/HSL: GLDAS VIC Land Surface Model L4 monthly 1.0 x 1.0 degree V2.1, Greenbelt, Maryland, USA, Goddard Earth Sciences Data and Information Services Center (GES DISC)., https://doi.org/10.5067/VWTH7S6218SG, 2020.

Beck, H. E., Zimmermann, N. E., McVicar, T. R., Vergopolan, N., Berg, A., and Wood, E. F.: Present and future Köppen-Geiger climate classification maps at 1-km resolution, Scientific Data, 5, 180 214, https://doi.org/10.1038/sdata.2018.214, publisher: Nature Publishing Group, 2018.

Chen, F., Mitchell, K., Schaake, J., Xue, Y., Pan, H.-L., Koren, V., Duan, Q. Y., Ek, M., and Betts, A.: Modeling of land surface evaporation by four schemes and comparison with FIFE observations, Journal of Geophysical Research: Atmospheres, 101, 7251–7268, 1996.

Cherkauer, K. A., Bowling, L. C., and Lettenmaier, D. P.: Variable infiltration capacity cold land process model updates, Global and Planetary Change, 38, 151–159, https://doi.org/10.1016/S0921-8181(03)00025-0, 2003.

Collatz, G. J., Ribas-Carbo, M., and Berry, J. A.: Coupled photosynthesis-stomatal conductance model for leaves of C4 plants, Functional Plant Biology, 19, 519–538, 1992.

Cosby, B. J., Hornberger, G. M., Clapp, R. B., and Ginn, T. R.: A Statistical Exploration of the Relationships of Soil Moisture Characteristics to the Physical Properties of Soils, Water Resources Research, 20, 682–690, https://doi.org/10.1029/WR020i006p00682, 1984.

De Pury, D. and FARQUHAR, G. D.: Simple scaling of photosynthesis from leaves to canopies without the errors of big-leaf models, Plant, Cell & Environment, 20, 537–557, 1997.

Deardorff, J. W.: Efficient prediction of ground surface temperature and moisture, with inclusion of a layer of vegetation, Journal of Geophysical Research: Oceans, 83, 1889–1903, 1978.

Derber, J. C., Parrish, D. F., and Lord, S. J.: The new global operational analysis system at the National Meteorological Center, Weather and forecasting, 6, 538–547, 1991.

Dorman, J. L. and Sellers, P. J.: A Global Climatology of Albedo, Roughness Length and Stomatal Resistance for Atmospheric General Circulation Models as Represented by the Simple Biosphere Model (SiB), Journal of Applied Meteorology and Climatology, 28, 833–855, https://doi.org/10.1175/1520-0450(1989)028<0833:AGCOAR>2.0.CO;2, 1989.

Ek, M., Mitchell, K., Lin, Y., Rogers, E., Grunmann, P., Koren, V., Gayno, G., and Tarpley, J.: Implementation of Noah land surface model advances in the National Centers for Environmental Prediction operational mesoscale Eta model, Journal of Geophysical Research: Atmospheres, 108, 2003.

Elnashar, A., Wang, L., Wu, B., Zhu, W., and Zeng, H.: Synthesis of global actual evapotranspiration from 1982 to 2019, Earth System Science Data, 13, 447–480, https://doi.org/10.5194/essd-13-447-2021, publisher: Copernicus GmbH, 2021.

Farquhar, G. D., von Caemmerer, S. v., and Berry, J. A.: A biochemical model of photosynthetic CO2 assimilation in leaves of C3 species, planta, 149, 78–90, 1980.

Franchini, M. and Pacciani, M.: Comparative analysis of several conceptual rainfall-runoff models, Journal of Hydrology, 122, 161–219, https://doi.org/10.1016/0022-1694(91)90178-K, 1991.

Gelaro, R., McCarty, W., Suárez, M. J., Todling, R., Molod, A., Takacs, L., Randles, C. A., Darmenov, A., Bosilovich, M. G., Reichle, R., Wargan, K., Coy, L., Cullather, R., Draper, C., Akella, S., Buchard, V., Conaty, A., Silva, A. M. d., Gu, W., Kim, G.-K., Koster, R., Lucchesi, R., Merkova, D., Nielsen, J. E., Partyka, G., Pawson, S., Putman, W., Rienecker, M., Schubert, S. D., Sienkiewicz, M., and Zhao, B.: The Modern-Era Retrospective Analysis for Research and Applications, Version 2 (MERRA-2), Journal of Climate, 30, 5419–5454, https://doi.org/10.1175/JCLI-D-16-0758.1, publisher: American Meteorological Society Section: Journal of Climate, 2017.

Helfand, H. M. and Schubert, S. D.: Climatology of the simulated Great Plains low-level jet and its contribution to the continental moisture budget of the United States, Journal of Climate, 8, 784–806, 1995.

Hersbach, H., Bell, B., Berrisford, P., Hirahara, S., Horányi, A., Muñoz-Sabater, J., Nicolas, J., Peubey, C., Radu, R., Schepers, D., Simmons, A., Soci, C., Abdalla, S., Abellan, X., Balsamo, G., Bechtold, P., Biavati, G., Bidlot, J., Bonavita, M., De Chiara, G., Dahlgren, P., Dee, D., Diamantakis, M., Dragani, R., Flemming, J., Forbes, R., Fuentes, M., Geer, A., Haimberger, L., Healy, S., Hogan, R. J., Hólm, E., Janisková, M., Keeley, S., Laloyaux, P., Lopez, P., Lupu, C., Radnoti, G., de Rosnay, P., Rozum, I., Vamborg, F., Villaume, S., and Thépaut, J.-N.: The ERA5 global reanalysis, Quarterly Journal of the Royal Meteorological Society, 146, 1999–2049, https://doi.org/10.1002/qj.3803, 2020.

Hijmans, R. J., Cameron, S. E., Parra, J. L., Jones, P. G., and Jarvis, A.: Very high resolution interpolated climate surfaces for global land areas, International Journal of Climatology: A Journal of the Royal Meteorological Society, 25, 1965–1978, 2005.

Hirai, M., Sakashita, T., Kitagawa, H., Tsuyuki, T., Hosaka, M., and OH’IZUMI, M.: Development and Validation of a New Land Surface Model for JMA’s Operational Global Model Using the CEOP Observation Dataset, Journal of the Meteorological Society of Japan. Ser. II, 85A, 1–24, https://doi.org/10.2151/jmsj.85A.1, 2007.

Hu, G. and Jia, L.: Monitoring of Evapotranspiration in a Semi-Arid Inland River Basin by Combining Microwave and Optical Remote Sensing Observations, Remote Sensing, 7, 3056–3087, https://doi.org/10.3390/rs70303056, 2015.

Huffman, G. J., Adler, R. F., Morrissey, M. M., Bolvin, D. T., Curtis, S., Joyce, R., McGavock, B., and Susskind, J.: Global precipitation at one-degree daily resolution from multisatellite observations, Journal of hydrometeorology, 2, 36–50, 2001.

Ishii, M., Shouji, A., Sugimoto, S., and Matsumoto, T.: Objective analyses of sea-surface temperature and marine meteorological variables for the 20th century using ICOADS and the Kobe collection, International Journal of Climatology: A Journal of the Royal Meteorological Society, 25, 865–879, 2005.

Iturbide, M., Gutiérrez, J. M., Alves, L. M., Bedia, J., Cerezo-Mota, R., Cimadevilla, E., Cofiño, A. S., Di Luca, A., Faria, S. H., Gorodetskaya, I. V., Hauser, M., Herrera, S., Hennessy, K., Hewitt, H. T., Jones, R. G., Krakovska, S., Manzanas, R., Martínez-Castro, D., Narisma, G. T., Nurhati, I. S., Pinto, I., Seneviratne, S. I., van den Hurk, B., and Vera, C. S.: An update of IPCC climate reference regions for subcontinental analysis of climate model data: definition and aggregated datasets, Earth System Science Data, 12, 2959–2970, https://doi.org/10.5194/essd-12-2959-2020, publisher: Copernicus GmbH, 2020.

Jarvis, P. G.: The interpretation of the variations in leaf water potential and stomatal conductance found in canopies in the field, Phil. Trans. R. Soc. Lond. B, 273, 593–610, https://doi.org/10.1098/rstb.1976.0035, 1976.

Jiang, C. and Ryu, Y.: Multi-scale evaluation of global gross primary productivity and evapotranspiration products derived from Breathing Earth System Simulator (BESS), Remote Sensing of Environment, 186, 528–547, https://doi.org/10.1016/j.rse.2016.08.030, 2016.

Jiang, C., Ryu, Y., Wang, H., and Keenan, T. F.: An optimality-based model explains seasonal variation in C3 plant photosynthetic capacity, Global Change Biology, 26, 6493–6510, 2020.

Kim, S., Anabalón, A., and Sharma, A.: An Assessment of Concurrency in Evapotranspiration Trends across Multiple Global Datasets, Journal of Hydrometeorology, 22, 231–244, https://doi.org/10.1175/JHM-D-20-0059.1, 2021.

Kobayashi, S., Ota, Y., Harada, Y., Ebita, A., Moriya, M., Onoda, H., Onogi, K., Kamahori, H., Kobayashi, C., Endo, H., Miyaoka, K., and Takahashi, K.: The JRA-55 Reanalysis: General Specifications and Basic Characteristics, Journal of the Meteorological Society of Japan. Ser. II, 93, 5–48, https://doi.org/10.2151/jmsj.2015-001, 2015.

Koppa, A., Akash Koppa, Rains, D., Petra Hulsman, and Miralles, D. G.: A deep learning-based hybrid model of global terrestrial evaporation, Nature Communications, 13, https://doi.org/10.1038/s41467-022-29543-7, mAG ID: 4225984022, 2021.

Koster, R. D. and Suarez, M. J.: A Comparative Analysis of Two Land Surface Heterogeneity Representations, Journal of Climate, 5, 1379–1390, https://doi.org/10.1175/1520-0442(1992)005<1379:ACAOTL>2.0.CO;2, 1992.

Koster, R. D., Suarez, M. J., Ducharne, A., Stieglitz, M., and Kumar, P.: A catchment-based approach to modeling land surface processes in a general circulation model: 1. Model structure, Journal of Geophysical Research: Atmospheres, 105, 24 809–24 822, https://doi.org/10.1029/2000JD900327, 2000.

Kowalczyk, E., Wang, Y., Law, R., Davies, H., McGregor, J., and Abramowitz, G.: The CSIRO Atmosphere Biosphere Land Exchange (CABLE) model for use in climate models and as an offline model, CSIRO Marine and Atmospheric Research Paper, 13, 42, 2006.

Kumar, S., Peterslidard, C., Tian, Y., Houser, P., Geiger, J., Olden, S., Lighty, L., Eastman, J., Doty, B., and Dirmeyer, P.: Land information system: An interoperable framework for high resolution land surface modeling, Environmental Modelling & Software, 21, 1402–1415, https://doi.org/10.1016/j.envsoft.2005.07.004, 2006.

Li, B., Beaudoing, H., Rodell, M., and NASA/GSFC/HSL: GLDAS Catchment Land Surface Model L4 monthly 1.0 x 1.0 degree V2.1, Greenbelt, Maryland, USA, Goddard Earth Sciences Data and Information Services Center (GES DISC)., https://doi.org/10.5067/FOUXNLXFAZNY, 2020.

Li, B., Ryu, Y., Jiang, C., Dechant, B., Liu, J., Yan, Y., and Li, X.: BESSv2.0: A satellite-based and coupled-process model for quantifying long-term global land–atmosphere fluxes, Remote Sensing of Environment, 295, 113 696, https://doi.org/10.1016/j.rse.2023.113696, 2023.

Li, C., Liu, Z., Yang, W., Tu, Z., Han, J., Li, S., and Yang, H.: CAMELE: Collocation-Analyzed Multi-source Ensembled Land Evapotranspiration Data, Earth System Science Data, 16, 1811–1846, https://doi.org/10.5194/essd-16-1811-2024, publisher: Copernicus GmbH, 2024.

Li, H., Wang, P., and Shen, C.: Towards end-to-end text spotting with convolutional recurrent neural networks, in: Proceedings of the IEEE international conference on computer vision, pp. 5238–5246, 2017.

Liang, X., Lettenmaier, D. P., Wood, E. F., and Burges, S. J.: A simple hydrologically based model of land surface water and energy fluxes for general circulation models, Journal of Geophysical Research: Atmospheres, 99, 14 415–14 428, https://doi.org/10.1029/94JD00483, 1994.

Liang, X., Wood, E. F., and Lettenmaier, D. P.: Surface soil moisture parameterization of the VIC-2L model: Evaluation and modification, Global and Planetary Change, 13, 195–206, https://doi.org/10.1016/0921-8181(95)00046-1, 1996.

Louis, J.-F.: A parametric model of vertical eddy fluxes in the atmosphere, Boundary-Layer Meteorology, 17, 187–202, 1979.

Mahrt, L. and Ek, M.: The influence of atmospheric stability on potential evaporation, Journal of Applied Meteorology and Climatology, 23, 222–234, https://journals.ametsoc.org/view/journals/apme/23/2/1520-0450_1984_023_0222_tioaso_2_0_co_2.xml, 1984.

Markonis, Y., Vargas Godoy, M. R., Pradhan, R. K., Pratap, S., Thomson, J. R., Hanel, M., Paschalis, A., Nikolopoulos, E., and Papalexiou, S. M.: Spatial partitioning of terrestrial precipitation reveals varying dataset agreement across different environments, Communications Earth & Environment, 5, 217, https://doi.org/10.1038/s43247-024-01377-9, number: 1, 2024.

McNally, A., Arsenault, K., Kumar, S., Shukla, S., Peterson, P., Wang, S., Funk, C., Peters-Lidard, C. D., and Verdin, J. P.: A land data assimilation system for sub-Saharan Africa food and water security applications, Scientific Data, 4, 170012, https://doi.org/10.1038/sdata.2017.12, number: 1 Publisher: Nature Publishing Group, 2017.

Miralles, D. G., Bonte, O., Koppa, A., Baez-Villanueva, O. M., Tronquo, E., Zhong, F., Beck, H. E., Hulsman, P., Dorigo, W., Verhoest, N. E. C., and Haghdoost, S.: GLEAM4: global land evaporation and soil moisture dataset at 0.1° resolution from 1980 to near present, Scientific Data, 12, 416, https://doi.org/10.1038/s41597-025-04610-y, publisher: Nature Publishing Group, 2025.

Monfreda, C., Ramankutty, N., and Foley, J. A.: Farming the planet: 2. Geographic distribution of crop areas, yields, physiological types, and net primary production in the year 2000, Global biogeochemical cycles, 22, 2008.

Mu, Q., Zhao, M., and Running, S. W.: Improvements to a MODIS global terrestrial evapotranspiration algorithm, Remote Sensing of Environment, 115, 1781–1800, https://doi.org/10.1016/j.rse.2011.02.019, 2011.

Muñoz-Sabater, J., Dutra, E., Agustí-Panareda, A., Albergel, C., Arduini, G., Balsamo, G., Boussetta, S., Choulga, M., Harrigan, S., Hersbach, H., Martens, B., Miralles, D. G., Piles, M., Rodríguez-Fernández, N. J., Zsoter, E., Buontempo, C., and Thépaut, J.-N.: ERA5-Land: a state-of-the-art global reanalysis dataset for land applications, Earth System Science Data, 13, 4349–4383, https://doi.org/10.5194/essd-13-4349-2021, publisher: Copernicus GmbH, 2021.

Niu, G.-Y., Yang, Z.-L., Mitchell, K. E., Chen, F., Ek, M. B., Barlage, M., Kumar, A., Manning, K., Niyogi, D., Rosero, E., Tewari, M., and Xia, Y.: The community Noah land surface model with multiparameterization options (Noah-MP): 1. Model description and evaluation with local-scale measurements, Journal of Geophysical Research: Atmospheres, 116, https://doi.org/10.1029/2010JD015139, _eprint: https://agupubs.onlinelibrary.wiley.com/doi/pdf/10.1029/2010JD015139, 2011.

Reichle, R. H., Draper, C. S., Liu, Q., Girotto, M., Mahanama, S. P. P., Koster, R. D., and Lannoy, G. J. M. D.: Assessment of MERRA-2 Land Surface Hydrology Estimates, Journal of Climate, 30, 2937–2960, https://doi.org/10.1175/JCLI-D-16-0720.1, 2017.

Reynolds, C., Jackson, T., and Rawls, W.: Estimating soil water-holding capacities by linking the Food and Agriculture Organization soil map of the world with global pedon databases and continuous pedotransfer functions, Water Resources Research, 36, 3653–3662, 2000.

Rodell, M., Houser, P. R., Jambor, U., Gottschalck, J., Mitchell, K., Meng, C.-J., Arsenault, K., Cosgrove, B., Radakovich, J., Bosilovich, M., Entin, J. K., Walker, J. P., Lohmann, D., and Toll, D.: The Global Land Data Assimilation System, Bulletin of the American Meteorological Society, 85, 381–394, https://doi.org/10.1175/BAMS-85-3-381, publisher: American Meteorological Society Section: Bulletin of the American Meteorological Society, 2004.

Ryu, Y., Baldocchi, D. D., Kobayashi, H., Van Ingen, C., Li, J., Black, T. A., Beringer, J., Van Gorsel, E., Knohl, A., Law, B. E., et al.: Integration of MODIS land and atmosphere products with a coupled-process model to estimate gross primary productivity and evapotranspiration from 1 km to global scales, Global Biogeochemical Cycles, 25, 2011.

Schaake, J. C., Koren, V. I., Duan, Q.-Y., Mitchell, K., and Chen, F.: Simple water balance model for estimating runoff at different spatial and temporal scales, Journal of Geophysical Research: Atmospheres, 101, 7461–7475, https://doi.org/https://doi.org/10.1029/95JD02892, 1996.

Sellers, P. J., Mintz, Y., Sud, Y. C., and Dalcher, A.: A Simple Biosphere Model (SIB) for Use within General Circulation Models, Journal of the Atmospheric Sciences, 43, 505–531, https://doi.org/10.1175/1520-0469(1986)043<0505:ASBMFU>2.0.CO;2, 1986.

Shuttleworth, W. J. and Wallace, J. S.: Evaporation from sparse crops-an energy combination theory, Quarterly Journal of the Royal Meteorological Society, 111, 839–855, https://doi.org/10.1002/qj.49711146910, 1985.

Simard, M., Pinto, N., Fisher, J. B., and Baccini, A.: Mapping forest canopy height globally with spaceborne lidar, Journal of Geophysical Research: Biogeosciences, 116, 2011.

Stieglitz, M., Ducharne, A., Koster, R., and Suarez, M.: The impact of detailed snow physics on the simulation of snow cover and subsurface thermodynamics at continental scales, Journal of Hydrometeorology, 2, 228–242, 2001.

Still, C. J., Berry, J. A., Collatz, G. J., and DeFries, R. S.: Global distribution of C3 and C4 vegetation: carbon cycle implications, Global biogeochemical cycles, 17, 6–1, 2003.

Tao, M., Chen, L., Wang, Z., Wang, J., Che, H., Xu, X., Wang, W., Tao, J., Zhu, H., and Hou, C.: Evaluation of MODIS Deep Blue aerosol algorithm in desert region of East Asia: Ground validation and intercomparison, Journal of Geophysical Research: Atmospheres, 122, 10–357, 2017.

Wang-Erlandsson, L., Bastiaanssen, W. G. M., Gao, H., Jägermeyr, J., Senay, G. B., van Dijk, A. I. J. M., Guerschman, J. P., Keys, P. W., Gordon, L. J., and Savenije, H. H. G.: Global root zone storage capacity from satellite-based evaporation, Hydrology and Earth System Sciences, 20, 1459–1481, https://doi.org/10.5194/hess-20-1459-2016, 2016.

Wei, S., Fang, H., Schaaf, C. B., He, L., and Chen, J. M.: Global 500m clumping index product derived from MODIS BRDF data (2001–2017), Remote Sensing of Environment, 232, 111 296, https://doi.org/10.1016/j.rse.2019.111296, 2019.

Willmott, C. J., Rowe, C. M., and Mintz, Y.: Climatology of the terrestrial seasonal water cycle, Journal of Climatology, 5, 589–606, 1985.

Zheng, C., Jia, L., and Hu, G.: Global land surface evapotranspiration monitoring by ETMonitor model driven by multi-source satellite earth observations, Journal of Hydrology, 613, 128 444, https://doi.org/10.1016/j.jhydrol.2022.128444, 2022.